Thermal Structure and Geodynamics of Subduction Zones

by

Ikuko Wada
B.Sc., University of Victoria, 2003

A Dissertation Submitted in Partial Fulfillment
of the Requirements for the Degree of

DOCTOR OF PHILOSOPHY

in the School of Earth and Ocean Sciences

Supervisory Committee

Thermal Structure and Geodynamics of Subduction Zones

by

Ikuko Wada
B.Sc., University of Victoria, 2003

Supervisory Committee

Dr. Kelin Wang (Pacific Geoscience Centre, Geological Survey of Canada and School of Earth and Ocean Sciences, University of Victoria)
Supervisor

Dr. George Spence (School of Earth and Ocean Sciences, University of Victoria)
Co-Supervisor

Dr. Roy D. Hyndman (Pacific Geoscience Centre, Geological Survey of Canada and School of Earth and Ocean Sciences, University of Victoria)
Departmental Member

Dr. John F. Cassidy (Pacific Geoscience Centre, Geological Survey of Canada and School of Earth and Ocean Sciences, University of Victoria)
Departmental Member

Dr. Henning Struchtrup (Department of Mechanical Engineering, University of Victoria)
Outside Member

Abstract

Supervisory Committee

Dr. Kelin Wang
Supervisor
Dr. George Spence
Co-Supervisor
Dr. Roy D. Hyndman
Departmental Member
Dr. John F. Cassidy
Departmental Member
Dr. Henning Struchtrup
Outside Member

The thermal structure of subduction zones depends on the age-controlled thermal state of the subducting slab and mantle wedge flow. Observations indicate that the shallow part of the forearc mantle wedge is stagnant and the slab-mantle interface is weakened. In this dissertation, the role of the interface strength in controlling mantle wedge flow, thermal structure, and a wide range of subduction zone processes is investigated through two-dimensional finite-element modelling and a global synthesis of geological and geophysical observations. The model reveals that the strong temperature-dependence of the mantle strength always results in full slab-mantle decoupling along the weakened part of the interface and hence complete stagnation of the overlying mantle. The interface immediately downdip of the zone of decoupling is fully coupled, and the overlying mantle is driven to flow at a rate compatible with the subduction rate. The sharpness of the transition from decoupling to coupling depends on the rheology assumed and increases with the nonlinearity of the flow system. This bimodal behaviour of the wedge flow gives rise to a strong thermal contrast between the cold stagnant and hot flowing

parts of the mantle wedge. The maximum depth of decoupling (MDD) thus dictates the thermal regime of the forearc. Observed surface heat flow patterns and petrologically and geochemically estimated mantle wedge temperatures beneath the volcanic arc require an MDD of 70-80 km in most, if not all, subduction zones regardless of their thermal regime of the slab. The common MDD of 70-80 km explains the observed systematic variations of the petrologic, seismological, and volcanic processes with the thermal state of the slab and thus explains the rich diversity of subduction zones in a unified fashion. Models for warm-slab subduction zones such as Cascadia and Nankai predict shallow dehydration of the slab beneath the cold stagnant part of the mantle wedge, which provides ample fluid for mantle wedge serpentinization in the forearc but little fluid for melt generation beneath the arc. In contrast, models for colder-slab subduction zones such as NE Japan and Kamchatka predict deeper dehydration, which provides greater fluid supply for melt generation beneath the arc and allows deeper occurrence of intraslab earthquakes but less fluid for forearc mantle wedge serpentinization. The common MDD also explains the intriguing uniform configuration of subduction zones, that is, the volcanic arc always tends to be situated where the slab is at about 100 km depth. The sudden onset of mantle wedge flow downdip of the common MDD overshadows the thermal effect of the slab, and the resultant thermal field and slab dehydration control the location of the volcanic arc. The recognition of the fundamental importance of the MDD has important implications to the study of geodynamics and earthquake hazard in subduction zones.

Table of Contents

List of Tables

List of Figures

Acknowledgements

Most of all, I would like to thank my supervisor, Kelin Wang, for his invaluable teaching and boundless inspiration and encouragement during the course of my doctoral research.

I would like to thank my committee members, George Spence, Roy Hyndman, John Cassidy, and Henning Struchtrup, and my external examiner, Peter van Keken, for their support and helpful comments.

I owe much gratitude to a number of scientists and staff members at the Pacific Geoscience Centre (PGC), Geological Survey of Canada, including John He for developing the numerical code for thermal modelling and for his help throughout my research, Tom James, Honn Kao, Stephane Mazzotti, Garry Rogers, Earl Davis, Trevor Lewis, and Michael Riedel for useful discussions and suggestions, Ralph Currie and Darlene Upton for their encouragement and hospitality, and Steve Taylor and Bruce Johnson for computer support.

I would also like to thank Claire Currie who is presently at University of Alberta for benchmarking the numerical code at PGC during her Ph.D. program and for her help during the early stage of my research.

I would also like to thank faculty and staff members in the School of Earth and Ocean Sciences, University of Victoria, who provided me with great help during my Ph.D. program.

Last but not least, I would like to thank my family, Shihoko and Shigeru Wada and Yuko and Yusuke Matsuda, for their patience and support, and my friends and fellow students for their understanding and help and for the countless fond memories.

Chapter 1

Introduction

1.1. Motivation and Objectives

The subduction of the relatively cold oceanic lithosphere into the hot asthenospheric mantle at a convergent margin leads to a complex system of mass and heat transfer, including the subduction of the oceanic plate itself, slab-driven mantle wedge flow, and perhaps small-scale buoyancy-driven mantle convection (**Figure 1.1**). The resultant thermal structure of the subduction zone controls many important geophysical processes (**Figure 1.2a**). The thermal structure controls metamorphic phase changes and associated dehydration reactions in the subducting slab, which in turn control volatile recycling in subduction zones and intraslab earthquakes [e.g. *Hacker et al.*, 2003a]. A relatively low

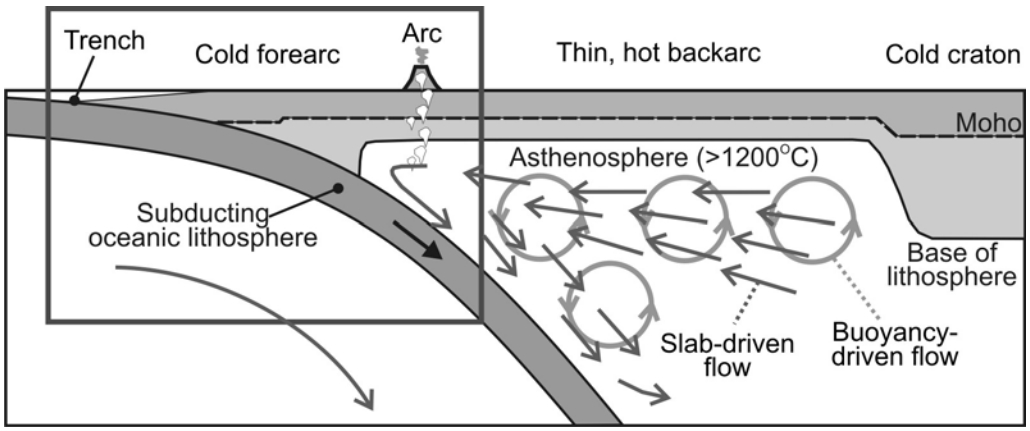

Figure 1.1. Schematic illustration of a conceptual model of mantle dynamics in subduction zones [modified from *Currie*, 2004a]. The box indicates the region of focus in this dissertation research.

temperature is required for the occurrence of earthquakes along the subduction interface and in both converging plates [e.g. *Kirby*, 1983; *Hyndman and Wang*, 1993] and for the serpentinization of the overriding mantle wedge [e.g. *Peacock and Hyndman*, 1999], but a high temperature is required for melt generation beneath the volcanic arc [e.g. *Tatsumi*

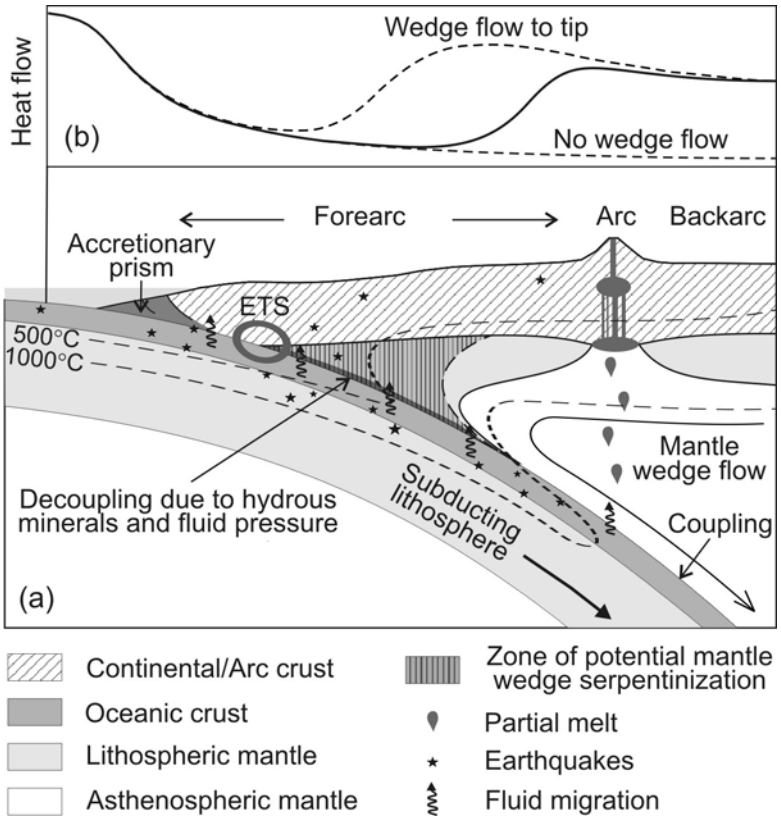

Figure 1.2. (a) Schematic illustration of the forearc-arc region of a typical subduction zone with a relatively young and warm subducting slab along a continental margin, showing the crustal and upper mantle components and processes that take place in them. ETS is episodic tremor and slip observed at Cascadia and Nankai. (b) Surface heat flow for a warm-slab subduction zone (solid curve). Heat flow patterns for cold-slab subduction zones are similar, except that values near the trench and further seaward are much lower. Models that allow the flow to occur near the tip of the wedge or do not include mantle wedge flow would incorrectly predict the heat flow pattern as indicated by dashed curves.

and Eggins, 1995]. The study of the thermal regime of subduction zones is therefore crucial to understanding subduction zone geodynamics.

The most direct observation that tells us about the thermal regime of subduction zones is surface heat flow. The surface heat flow is low in the forearc, indicating a cool thermal state of the underlying material, but high in the arc and backarc, indicating a hot thermal state (**Figure 1.2b**). One of the most important processes that control the forearc-arc thermal structure is solid-state mantle wedge flow (**Figure 1.2a**). This flow brings in hot mantle material from the backarc and greater depths to replace cold material that travels downdip with the slab, heating up the mantle wedge and its surroundings. In the forearc-arc region, the flow is driven primarily by viscous coupling between the subducting slab and the overriding mantle. This dissertation focuses particularly on the effect of slab-mantle coupling on mantle wedge flow.

Many processes in subduction zones depend on the availability of aqueous fluid at depth (**Figure 1.2a**). The primary source of the fluid in subduction zones is the dehydrating slab. Earthquakes in the subducting slab are thought to be facilitated by fluid released during the dehydration [*Kirby et al*., 1996a]. Fluid along the plate interface affects great thrust earthquakes [e.g. *Hyndman and Wang*, 1993] and is possibly responsible for episodic tremor and slip (ETS) that occur around the forearc mantle wedge tip in some warm-slab subduction zones such as Cascadia [*Kao et al.*, 2005] and Nankai [*Shelly et al.*, 2006]. The addition of fluid to the cold part of the overriding mantle causes serpentinization [*Hyndman and Peacock*, 2003], and the addition of the fluid to the hot part of the mantle wedge beneath the arc lowers the mantle solidus, triggering melting and hence arc magmatism [*Tatsumi and Eggins*, 1995]. The

subduction zone thermal structure is the primary control of the dehydration of the subducting slab. By modelling the thermal structure, I hope to provide a better understanding of the fluid supply at depth.

The above mentioned processes are known to vary systematically with the thermal state of the subducting slab [e.g. *Peacock and Wang*, 1999; *Hacker et al.*, 2003a]. It is their variations that give rise to the diversity of subduction zones. In contrast, the configuration of subduction zones is rather uniform in that the volcanic arc is typically situated where the slab is at around 100 km depth [*Tatsumi and Eggins*, 1995; *England et al.*, 2004]. What causes the diversity and uniformity of subduction zones has not been resolved and is an outstanding issue in the study of subduction zone geodynamics. It is also the aim of this dissertation research to explore mechanisms that reconcile the two contrasting characteristics.

1.2. Previous Studies of the Thermal Structure of the Forearc-Arc Region

The thermal structure of the forearc-arc region depends on the thermal state of the subducting slab and slab-driven mantle wedge flow [*McKenzie*, 1969]. The thermal state of the slab is controlled primarily by its age and is colder for older slabs [e.g. *Peacock*, 1993; *Peacock and Wang*, 1999]. In the study of subduction zone thermal structure, mantle wedge flow has been modelled as basally driven corner flow. Analytical solutions of *Batchelor* [1967] can efficiently calculate the corner flow in an isoviscous mantle wedge with a planar slab-mantle wedge interface. The thermal field in subduction zones has also been modelled using simple analytical solutions [e.g. *Davies*, 1999; *England and*

Wilkins, 2004]. In some numerical thermal models [e.g. *Peacock and Wang*, 1999], the flow field in the mantle wedge is calculated using the analytical corner flow solution of *Batchelor* [1967], but the heat transfer equation is solved numerically. Models of this type are computationally efficient but suffer from the assumptions of a planar slab-mantle interface and isoviscous mantle wedge. In models that solve both the flow and heat transfer equations numerically, a more realistic plate geometry and mantle wedge rheology can be used, and the mantle wedge flow is driven commonly by kinematically prescribed motion of the subducting slab [e.g. *Honda*, 1985; *Davies and Stevenson*, 1992; *Furukawa*, 1993; *Iwamori*, 1997; *Conder et al.*, 2002; *van Keken et al.,* 2002; *Kelemen et al.*, 2003; *Currie et al.*, 2004a]. In some large-scale dynamic models, the position of the slab is allowed to change [e.g. *Gurnis and Hager*, 1988; *King and Ita*, 1995; *Chen and King*, 1998; *Kincaid and Sacks*, 1997; *Billen and Hirth*, 2007].

The previous works show that the pattern of mantle wedge flow and thermal structure depend on the mantle wedge rheology. The models with a simple isoviscous mantle rheology feature rather evenly distributed flow and relatively low temperatures in the mantle wedge [e.g. *Davies and Stevenson*, 1992; *Peacock and Wang*, 1999], whereas models with a more realistic temperature- and stress-dependent rheology feature more focused corner flow which results in considerably high temperatures in the mantle wedge that are more consistent with petrological expectations [e.g. *van Keken et al.,* 2002; *Currie et al.*, 2004a].

In subduction zone thermal models, allowing flow of the entire mantle wedge results in forearc heat flow that is significantly higher than observed (**Figure 1.2b**). To satisfy the surface heat flow observations, a rigid mantle wedge corner was imposed in

some models to prevent hotter mantle material from entering the corner [e.g. *Peacock and Wang*, 1999; van *Keken et al.*, 2002; *Currie et al.*, 2004a]. The primary factor that controls the vigour of mantle wedge flow is the slab-mantle coupling [*Wada et al.*, 2008], and thus a lack of mantle wedge flow beneath the forearc indicates decoupling. A few studies [e.g. *Furukawa*, 1993; *Kneller et al.*, 2005] simulated slab-mantle decoupling in the forearc region by prescribing a free slip condition along the interface or assigning the mantle material just above the slab to flow at a very low velocity.

1.3. Outline of the Thesis

In this dissertation research, I use a two-dimensional steady-state thermal model to investigate the first-order effects of the slab-mantle decoupling on mantle wedge flow and subduction zone thermal structure. **Chapter 2** is designed to provide background knowledge for key parameters that control the thermal structure of subduction zones and important temperature-dependent subduction zone processes that are studied in this dissertation. Geological and geophysical observations compiled from seventeen subduction zones will illustrate how these processes vary with the thermal state of the subducting slab. **Chapter 3** provides a brief review of the rheological law for the mantle wedge, the governing equations for steady-state thermal models, and the numerical method employed in this work. I will also describe how the slab-mantle coupling is represented by a thin layer applied along the plate interface in the model. **Chapter 4** presents a new thermal model for northern Cascadia. Using the model, I examine in detail how mantle wedge flow and the subduction zone thermal structure are affected by

various degrees of slab-mantle decoupling. Several thermal models for northern Cascadia already exist, but the model developed for this dissertation directly simulates slab-mantle decoupling and thus aims to provide a better understanding of the mantle wedge flow dynamics. In **Chapter 5**, I present thermal and petrological models for all the seventeen subduction zones and illustrate that the common maximum depth of decoupling of 70-80 km can explain a wide range of observations and can reconcile the diversity and uniformity of subduction zones. **Chapter 6** provides main conclusions drawn from this dissertation research and recommendations for future research.

Chapter 2

Thermal Regime and Petrologic, Seismological and Volcanic Processes of Subduction Zones

In this chapter, I first briefly describe the two primary factors that control the thermal structure of subduction zones: the thermal state of the subducting slab and mantle wedge flow. I then summarize the present state of knowledge of three main temperature-dependent processes that are studied in this dissertation research: metamorphic processes, earthquakes, and arc volcanism. I compile geological and geophysical observations that characterize these processes and examine their trends. The observations were compiled from seventeen subduction zones (**Figure 2.1**) that were selected on the basis of the availability of geological and geophysical observations and structural and kinematic information. This relatively large number of subduction zones and the wide range of the thermal state of the slab spanned by them are ideal for examining the trends of observations. This chapter also serves to further explain scientific issues to be addressed in this study. Some of the materials in this chapter are presented in a paper by *Wada and Wang* [2009, in press].

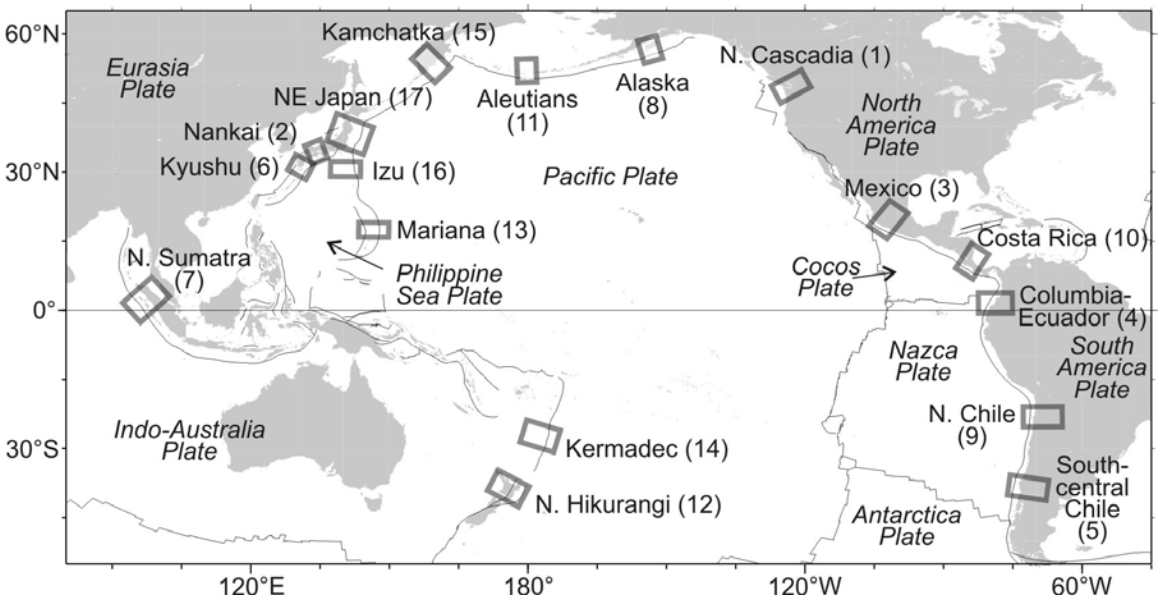

Figure 2.1. Map showing the locations of seventeen subduction zone corridors (rectangles) investigated in the present study. The number in parentheses indicates the index number of the subduction zone.

2.1. Thermal State of the Subducting Slab

The thermal state of the oceanic plate depends primarily on its age as indicated by surface heat flow that decreases with increasing plate age [*Stein and Stein*, 1992]. In subduction zones, isotherms are advected downward by the subducting oceanic plate (**Figure 1.2**), and the maximum depth of a given isotherm within the subducting lithosphere depends on its descent rate. Thus, the thermal state of the subducting slab is often described by the thermal parameter, ϕ, a product of the age and descent rate of the slab [*McKenzie*, 1969; *Molnar et al.*, 1979; *Kirby et al.*, 1996a]. Generally, the higher the ϕ value, the cooler is the slab at a given depth.

The ϕ values for the seventeen subduction zones shown in **Figure 2.1** are summarized in **Table 2.1**. For the calculation of ϕ, I use the age of the subducting slab

Table 2.1. Summary of subduction zone parameters

Index	Subduction zone	ϕ / 100 (km)	Slab age at trench (Ma) and references		Convergence rate (mm/yr)	Subduction direction[a] (°)	Subduction rate[b] (mm/yr)	Slab dip[c] (°)	Sub-arc slab depth H (km) and references	
1	N. Cascadia	2.2	8	*Wilson* [1988]	43	62	43	40	90	*McCrory et al.* [2004]
2	Nankai	3.9	15	*Okino et al.* [1994]	46	315	44	36	90	See **Section 2.5.3**[e]
3	Mexico	4.2	13	*Kostoglodov and Brandy* [1995]	55	35	55	36	110	*Currie et al.* [2002]
4	Colombia-Ecuador	4.5	16	*Hardy* [1991]	65	80	46	38	110	See **Section 2.5.3**[e]
5	SC Chile	8.6	25	*Tebbens et al.* [1997]	80	79	71	29	80	*Syracuse and Abers* [2006]
6	Kyushu	10.5	27	*Okino et al.* [1994]	50	315	47	56	105 ± 5	*England et al.* [2004]
7	N. Sumatra	11.2	50	*Cande and Kent* [1995]	55	12	40	34	115 ± 5	*England et al.* [2004]
8	Alaska	13.3	46	*Atwater* [1989]	55	341	47	38	85 ± 5	*England et al.* [2004]
9	N. Chile	13.4	48	*Müller et al.* [1997]	80	78	78	21	115 ± 5	*England et al.* [2004]
10	N. Costa Rica	17.1	24	*Barckhausen et al.* [2001]	85	23	80	63	95	*Syracuse and Abers* [2006], *Peacock et al.* [2005]
11	Aleutians	22.8	55	*Müller et al.* [1997]	72	319	54	50	80 ± 5 ~ 105 ± 6[d]	*England et al.* [2004]
12	N. Hikurangi	22.9	100	See **Section 2.1**.	41	266	29	52	85	*Reyners et al.* [2006, 2007]
13	Mariana	36.7	140	*Müller et al.* [1997]	39	310	30	61	115 ± 10	*England et al.* [2004]
14	Kermadec	47.3	100	See **Section 2.1**.	60	272	57	56	95 ± 5	*England et al.* [2004]
15	Kamchatka	47.8	100	*Müller et al.* [1997]	77	308	76	39	95 ± 5	*England et al.* [2004]
16	Izu	52.2	140	*Müller et al.* [1997]	55	286	51	47	130 ± 6	*England et al.* [2004]
17	NE Japan	52.3	130	*Müller et al.* [1997]	83	297	83	29	100 ± 5	*England et al.* [2004]

[a] Subduction direction is measured from north.

[b] The margin-normal component of the convergence rate is used.

[c] The average dip between 75 and 140 km depths is used.

[d] *England et al.* [2004] determined H for the western, central, and eastern segments of the Aleutian margin. The depth range shown is from the shallowest (eastern segment) to the deepest (western segment) of the three. An H value of 95 km is used in the thermal model for this margin as described in **Section 5.5.3**.

[e] The sub-arc slab depth was extrapolated from the existing slab geometry model for the shallow part of the slab and from limited intraslab earthquakes in the EHB catalog in the present study.

determined from magnetic isochrons on the oceanic plate as reported in the literature (**Table 2.1**), except for northern Hikurangi and Kermadec where the isochrons on the incoming plate are not identifiable at present. The old age (~100 Ma) of the adjacent oceanic crust and tectonic reconstruction suggest that the subducting plates at these two margins are no younger than 100 Ma [*Davy and Wood*, 1994; *Müller et al.*, 1997]. The thermal states of old oceanic plates (> ~80 Ma) are uniformly cold (surface heat flow of < 60 mW/m^2), and their differences are negligibly small. Thus, I assume a slab age of 100 Ma for these two margins.

The descent rate of the slab is the product of the margin-normal convergence rate and the sine of the dip of the slab. I calculate the convergence rates by using the global plate motion model NUVEL-1A [*DeMets et al.*, 1990, 1994] except for Nankai, Kyushu, Mexico, Costa Rica and Sumatra. I use a relative plate motion model determined by *Zang et al.* [2002] for Nankai and Kyushu and one by *DeMets* [2001] for Mexico and Costa Rica. These two models are constrained by newly obtained plate motion data in addition to those used to constrain NUVEL-1A and are more accurate than NUVEL-1A for the relative plate motions at these four margins. In Sumatra, the Australia plate subducts beneath the Sunda tectonic block, which is not differentiated from the adjacent Eurasia plate in NUVEL-1A, and therefore I use the relative plate motions constrained by GPS data for this margin [*Bock et al.*, 2003]. For the calculation of ϕ, I use the average dip between 75 and 140 km depths; for the purpose this study, the absolute depths are unimportant as long as the choice is made consistently between different subduction zones. The shape of the slab in northern Cascadia is described in **Chapter 4** and that in the other sixteen subduction zones is described in **Chapters 5**.

2.2. Mantle Wedge Flow

2.2.1. Seaward Extent of Mantle Wedge Flow

In the mantle wedge, the rock material undergoes solid-state flow. In the forearc-arc region, the flow is driven primarily by viscous coupling between the downgoing slab and the mantle. The positive buoyancy of deep, hot material in the backarc mantle may cause small-scale convection (buoyancy-driven flow), which may be responsible for the observed high surface heat flows in the backarc region (**Figure 1.1**). However, in the forearc region, buoyancy-driven flow is likely to be discouraged due to the narrow space and relatively small temperature difference between the top and the bottom of the mantle wedge [*Currie et al.*, 2004a; *Currie and Hyndman*, 2006]. Small-scale convection may also be driven by other mechanisms, such as foundering of the lower crust of the overriding plate [e.g. *Behn et al.*, 2007] and the development of pressure gradients caused by variations in slab geometry along the margin [*Hall et al.*, 2000; *Kneller and van Keken*, 2008]. However, their thermal effects on the forearc-arc region are likely to be small compared to that of slab-driven mantle flow.

The slab-driven mantle flow brings up hot material from greater depths and the backarc region and is responsible for high surface heat flow in the arc region and high mantle temperatures required for the generation of magma for arc volcanism. In contrast, geophysical and geological evidence indicates that most of the forearc mantle wedge does not participate in this flow. The most direct evidence is surface heat flow. Heat flow typically decreases arc-ward from the trench to values as low as 30 mW/m^2 before it increases to the arc and backarc values of ~80 mW/m^2 [*Currie and Hyndman*, 2006; see

also references for surface heat flow observations summarized in **Table 2.2**] (**Figure 1.2b**). The initial decrease is the direct cooling effect of the subducting slab, and the eventual landward increase is due to advective heat transport by mantle wedge flow. The increase is observed to be rather sharp in some subduction zones. The sharpness must be caused by local near-surface processes, such as magmatic and hydrothermal activities. Where the heat flow begins to increase indicates the seaward limit of mantle wedge flow. The pattern of observed heat flow indicates that thermally significant wedge flow does not begin until near the volcanic arc. In order to fit heat flow observations, a number of authors have concluded that a trench-ward part of the mantle wedge beneath the forearc must be stagnant [*Furukawa*, 1993; *Peacock and Wang*, 1999; *van Keken et al.*, 2002; *Currie et al.*, 2004a].

Another line of evidence for a cold forearc corner is mantle wedge serpentinization, which has been inferred from geological evidence such as serpentine mud volcanoes and from geophysical observations such as low seismic velocities, high Poisson's ratio, and positive gravity anomalies [*Hyndman and Peacock*, 2003, and references therein]. Inferences of mantle wedge serpentinization using geophysical observations will be described in greater detail in **Section 2.3.3**. The presence of serpentinites suggests conditions of relatively low temperatures and high contents of aqueous fluids [*Hyndman and Peacock*, 2003]. Such conditions cannot be sustained if there is vigorous mantle wedge flow to replenish continuously the forearc mantle wedge with dryer and hotter material brought up from greater depths.

A number of studies show seismic attenuation in the forearc mantle wedge to be low, which is in sharp contrast with high attenuation beneath the arc and is thought to

Table 2.2. Geological and geophysical observations

Index	Subduction zone	References for heat flow data in the forearc-arc region	Maximum downdip extent of a low-velocity layer (km) and references		Maximum depth of intraslab seismicity (km) and references		Volcanic output rate (km^3/Ma)	Eruption duration (Ma)	Measured volcano
1	N. Cascadia	*Currie et al.* [2004a], *Wang et al.* [1995]	45-75	*Bostock et al.* [2002], *Cassidy and Ellis* [1993]	70	*Cassidy and Waldhauser* [2003]	125[b]	1.29	Mt. Baker
2	Nankai	*Tanaka et al.* [2004]	60	*Hori et al.* [1985], *Hori* [1990], *Ohkura* [2000]	70	*Nakamura et al.* [1997], *Baba et al.* [2002]			
3	Mexico	*GHFD*[a]			90	*Engdahl et al.* [1998]	24[b]	1	Zitacuaro-Valle de Bravo
4	Colombia-Ecuador	*Marcaillou et al.* [2006]			90	*Engdahl et al.* [1998]	1500[b]	0.002	Tungurahua
5	SC Chile	*Grevemeyer et al.* [2003], *GHFD*[a]			115	*Haberland et al.* [2006], *Engdahl et al.* [1998]	800 ± 180[b]	0.65	Calabozos caldera
6	Kyushu	*Tanaka et al.* [2004]			200	*Zhao et al.* [2000], *Engdahl et al.* [1998]	1800 ± 500[c]	0.014	Sakurajima
7	N. Sumatra	*GHFD*[a]			180	*Engdahl et al.* [1998]			
8	Alaska	*GHFD*[a]	120	*Rondenay et al* [2008], *Abers et al.*[2006]	200	*Engdahl et al.* [1998]	700[b]	0.89	Regional average
9	N. Chile	*GHFD*[a]	120	*Yuan et al.* [2000], *Bock et al.* [2000]	240	*Engdahl et al.* [1998]	374[b]	10	per 100 km
10	N. Costa Rica	*Langseth and Silver* [1996], *Kimura et al.* [1997]			200	*Peacock et al.* [2005]	550[c]	4.73e-5	Arenal
11	Aleutians	*GHFD*[a]			200	*Engdahl et al.* [1998]	100[b]	3.5	per 100 km
12	N. Hikurangi	*GHFD*[a], *Townend* [1997]			> 300	*Engdahl et al.* [1998]	11000 ± 1000[c]	0.61	Taupo
13	Mariana	*GHFD*[a]			> 300	*Engdahl et al.* [1998]	1250[c]	5	per 100 km
14	Kermadec	*von Herzen et al.* [2001]			> 300	*Engdahl et al.* [1998]			
15	Kamchatka	*Tanaka et al.* [2004]			> 300	*Engdahl et al.* [1998]	6900[b]	0.01	Tolbachik
16	Izu				> 300	*Engdahl et al.* [1998]	1500[b]	0.025	Oshima
17	NE Japan	*Tanaka et al.* [2004]	100-150	*Matsuzawa et al.* [1986], *Kawakatsu and Watada* [2007]	> 300	*Engdahl et al.* [1998]	1200 ± 300[c]	0.3	Asama

[a] GHFD is an abbreviation for Global Heat Flow Data Base [*Pollack et al.*, 1993; *Global Heat Flow Database*, 2004].
[b] Values are from *White et al.* [2006].
[c] Values are from *Crisp* [1984].

indicate low temperatures in a stagnant forearc mantle wedge [e.g., *Wiens and Smith*, 2003; *Stachnik et al*., 2004]. Well-located earthquakes in the forearc mantle wedge [e.g., *Hasegawa et al.*, 1994; *Nakajima et al.*, 2001; *Miura et al.*, 2003], although rare, also indicate low temperatures that are required for seismic failure. All these observations point to a stagnant and cold forearc mantle, in sharp contrast with the flowing and hot mantle beneath the arc region.

2.2.2. Decoupling of the Slab and Mantle Wedge Beneath the Forearc

The necessary condition for the forearc mantle wedge to become stagnant and cold is that its basal drag force is very small relative to the strength of the overlying material, that is, the slab and the mantle wedge must be adequately decoupled [*Furukawa*, 1993]. This decoupling has been attributed largely to the addition of fluids from the dehydrating slab into the material at the base of the mantle wedge, where aqueous fluid is the most available.

Simple addition of fluids weakens the plate interface by elevating pore fluid pressure. Although still difficult to constrain with direct measurements, pore fluid pressure along the interface is expected to be high and probably decreases upward into the mantle wedge. It has been argued that upward migration of aqueous fluids from the dehydrating slab is possible only through permeability creation via hydrofracturing [*Peacock and Hyndman*, 1999]. Hydrofracturing requires pore fluid pressure to exceed the minimum principal stress, and the most likely place to reach this state is the base of the mantle wedge which is nearest to the fluid source.

The addition of fluids to the base of the mantle wedge also results in the formation of hydrous minerals, such as serpentine minerals, chlorite, talc, brucite, and amphibole, along the interface. **Section 2.3.3** will provide more information on the hydration of the mantle wedge. These hydrous minerals are generally weaker than anhydrous minerals that would be found in a dry mantle wedge [e.g., *Morrow et al.*, 2000; *Christensen*, 2004] and can substantially weaken the subduction interface [*Peacock and Hyndman,* 1999].

Along the most updip, coldest part of the slab-mantle wedge interface, coupling may take place as frictional sliding. Laboratory experiments at room temperature on frictional strengths of antigorite-rich gouge at wet conditions show that the coefficient of friction (μ) is ~0.5 [*Morrow et al.*, 2000]. The μ values of chlorite, brucite, and talc, are ~0.4, ~0.3, and ~0.2, respectively [*Morrow et al.*, 2000]. The sheeted structure of these phillosilicate minerals and loose bonding of H_2O to the mineral surface both lead to low frictional strength [*Morrow et al.*, 2000]. Thus, their presence decreases coupling between the slab and the mantle wedge.

Along the deeper, warmer part of the slab-mantle interface, deformation is likely to be dominated by ductile shear. At the pressure-temperature (PT) condition of the forearc mantle wedge, the viscosity of serpentinite (antigorite, which is to be further discussed in **Sections 2.3.2** and **2.3.3**) is one to two orders of magnitude smaller than that of mantle rock peridotite [*Hilairet et al.*, 2007; *Chernak and Hirth*, 2008] (**Figure 2.2**). Sufficient fluid supply and a stable PT condition along the interface can lead to a weak serpentine-rich band, in which shear strain localizes, effectively reducing the coupling between the slab and the overriding mantle. The incorporation of H_2O as lattice impurities in olivine, the primary constituent of peridotite, also lowers viscosity by 1-2 orders of magnitude

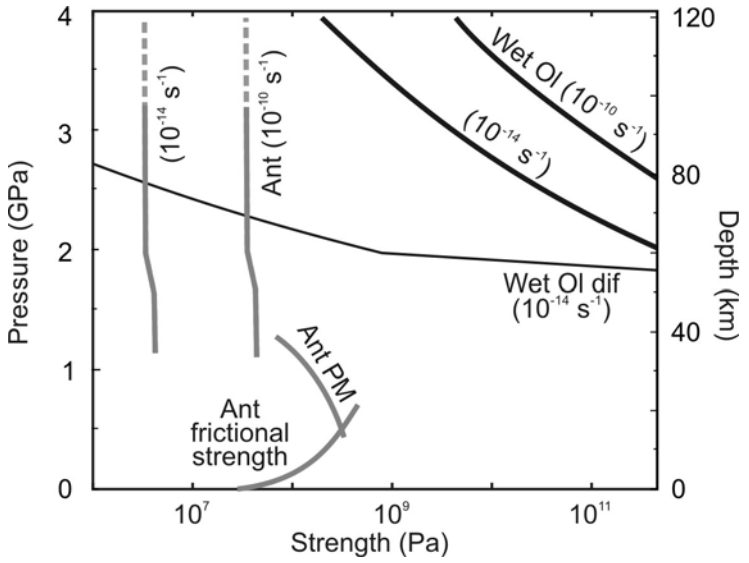

Figure 2.2. Strength of antigorite (Atg, grey thick lines) and olivine (Ol, black thick lines) calculated from deformation laws at a strain rate of 10^{-10} and 10^{-14} s^{-1} [*Hilairet et al.*, 2007]. The strength of the material was calculated for the PT path of the slab surface calculated by a thermal model of *Conder* [2005]. The thermal model consists of a 50-km-thick non-deforming overriding plate, an isoviscous mantle wedge, and a 50-Myr-old subducting slab with a dip of 45° and a subduction rate of 60 mm/yr. In the model, the mantle wedge corner is assumed to be rigid, and the base of this rigid corner is defined by a thermally controlled brittle-ductile transition.

[*Hirth and Kohlstedt*, 1996; *Mei and Kohlstedt*, 2000; *Hirth and Kohlstedt*, 2003].

It is important to recognize that decoupling or coupling depends also on the strength of the overlying mantle material. If the mantle wedge deforms as readily as does the interface, there will be no decoupling. The mantle material is highly sensitive to temperature, as will be discussed in more detail in **Section 3.1**. It is strong at shallow depths where the temperature is low and becomes very weak at greater depths where the temperature is high. Thus, the weakening of the mantle wedge with increasing depth diminishes the strength contrast between the interface and mantle wedge, eventually resulting in full coupling. Beneath the volcanic arc, the presence of melts further reduces

the viscous strength of the mantle material [e.g. *Hirth and Kohlstedt*, 2003].

2.3. Metamorphic Processes

2.3.1. The Subducting Igneous Oceanic Crust

The fresh oceanic crust that is created at the mid-ocean ridge, the mid-ocean-ridge basalt (MORB), contains little water and is depleted in incompatible elements (i.e. those that preferentially partition into the melt phase) such as potassium (K) and uranium (U), due to repeated episodes of partial melting of the magma source. However, the top-most portion of the oceanic crust is relatively porous and permeable due to lava drainage, fissuring, and fractures, promoting pervasive hydrothermal circulation and alteration [*Davis et al.*, 1997], resulting in enrichment of MORB with some of the incompatible elements [e.g. *Staudigel et al.*, 1996]. Hydrothermal alteration also results in the formation of hydrous minerals, such as chlorite, epidote/zoisite, amphibole (hornblende, actinolite, and tremolite), chloritoid, talc, and phengite [*Schmidt and Poli*, 1998]. The lower portion of the crust is likely to be hydrated locally along faults except under unusual conditions.

As temperature and pressure increase, the subducting oceanic crust undergoes a number of metamorphic phase changes and dehydration reactions, continuously releasing aqueous fluid (**Figure 2.3**) [*Hacker et al.*, 2003b]. The transformation from basalt to eclogite in particular releases a large amount of fluid, signalling the peak of slab dehydration reactions. The basalt-eclogite transformation results in an increase in density and seismic velocities. The subduction of marine sediments is an important mechanism of

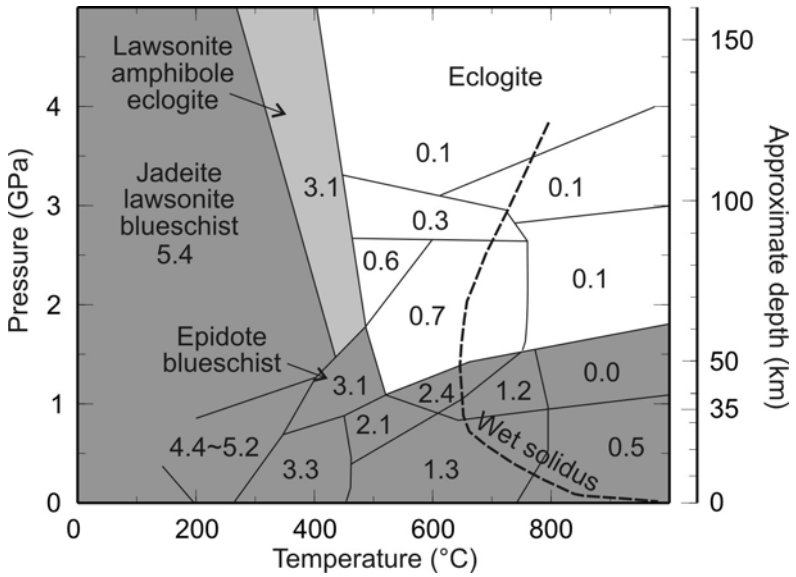

Figure 2.3. Phase diagram for H_2O-saturated mid-oceanic ridge basalt [*Hacker et al.*, 2003b]. Each facies is labeled with the maximum bound H_2O in wt%. White region consists of various eclogite facies. See *Hacker et al.* [2003b] for the composition of each facies. The peak dehydration (i.e. reactions that lead to a relatively dry crust) occurs at the boundary between the light/dark grey and white regions. In the anhydrous lower crust, the transformation may be kinetically delayed to deeper depths than in the hydrated upper crust [*Hacker et al*, 2003b]. The pressure-derived depth scale on the right is based on 35-km-thick crust (2750 kg/m^3) and underlying mantle (3300 kg/m^3). This depth scale is applicable to most continental margins, including Cascadia.

fluid transportation and chemical recycling in subduction zones, but the amount of the subducting sediments is usually negligibly small, and thus in this dissertation, the metamorphic and mechanical consequences of sediment subduction are not discussed at length.

Where resolution allows, seismological studies have revealed the presence of a narrow dipping layer of relatively low seismic-wave speed along the top of the subducting slab. It is commonly interpreted to be the basaltic oceanic crust that has not

transformed to eclogite [*Fukao et al.* 1983]. In Cascadia, analyses of receiver functions [*Cassidy and Ellis*, 1993] and scattered teleseismic body waves [*Bostock et al.*, 2002] indicate the presence of a low-velocity layer (LVL) down to 45-75 km depths. In Nankai, later P and S wave phases that traveled through the untransformed subducting crust indicate that an LVL extends to ~60 km [*Hori et al.*, 1985; *Hori*, 1990; *Ohkura*, 2000]. In northern Chile, receiver function analyses show an LVL extending to ~120 km depth [*Yuan et al.*, 2000; *Bock et al.*, 2000]. In Alaska, analyses of scattered teleseismic body waves [*Rondenay et al*., 2008] and receiver functions [*Abers et al.*, 2006] indicate an LVL extending to ~120 km depth. In northeast (NE) Japan, analyses of PS-P time data [*Matsuzawa et al.*, 1986] and receiver functions [*Kawakatsu and Watada*, 2007] show an LVL extending to 100-150 km depths. The downdip extent of this layer is clearly deeper in the older and colder slabs in northern Chile, Alaska, and NE Japan than in younger and warmer slabs in Cascadia and Nankai (**Figure 2.4**). This trend agrees with petrologic

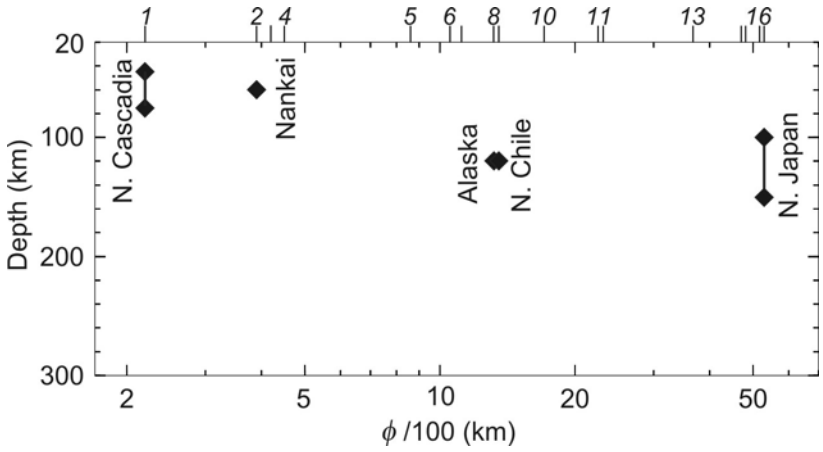

Figure 2.4. Variation in the observed maximum depth of a low-velocity layer in the subducting crust (diamond) with the thermal parameter ϕ (**Table 2.2**). The ϕ values of the seventeen subduction zones (**Figure 2.1**, **Table 2.1**) are shown at the top.

predictions based on thermal models [e.g. *Peacock and Wang*, 1999; *Hacker et al.*, 2003a].

Abers [2005] used body wave dispersion to determine the velocity contrast of an LVL with its surroundings for three depth ranges (0-100, 100-150, and > 200 km) in Nicaragua (near the focus region of northern Costa Rica of the present study), Aleutians, Alaska, Mariana, Kamchatka, and NE Japan. The results can be interpreted to indicate the presence of an LVL to at least 150 km depth at the six margins, although the exact maximum depth is undetermined because of the large depth bins used in the study. The slabs in all the six subduction zones are relatively cold, and the inferred, relatively deep downdip extent of the LVL is consistent with those reported for other cold-slab subduction zones (**Figure 2.4**). Furthermore, in Nicaragua and Alaska where the slabs are warmest among the six subduction zones, the velocity contrast of the LVL with its surroundings practically disappears for the > 150 km depth bin, indicating that the downdip limit of the layer is within the 100-150 km range, also consistent with the general trend illustrated in **Figure 2.4**.

2.3.2. The Subducting Oceanic Mantle

Oceanic mantle lithosphere is peridotitic in composition (mostly olivine and pyroxene), and its upper portion consists of the residual (harzburgite) of mantle material after MORB formation whereas the lower portion consists of less depleted mantle material (lherzolite) [*Irifune*, 1993]. On the basis of geochemical and geophysical, especially seismic, observations, it is generally accepted that the typical oceanic upper

mantle contains only a small amount of H_2O in the form of lattice impurities in minerals and contains little hydrous phases except in its upper portion where the infiltration of seawater through deep cutting faults may hydrate the mantle locally. These deep cutting faults may form due to tectonic extension near the spreading centre or due to bending at the outer rise along convergent margins [*Peacock*, 2001; *Ranero et al.*, 2003; *Ulmer and Trommsdorf*, 1995]. Local hydration of the oceanic upper mantle has been inferred from seismic studies to reach > 15 km depth [e.g. *Ranero et al.*, 2003] and speculated to reach up to ~40 km depth [*Peacock*, 2001; *Seno et al.*, 2001].

The principal hydrous minerals in H_2O-saturated peridotite at the pressure and temperature conditions of the oceanic upper mantle include serpentine, talc, chlorite, and amphibole (**Figure 2.5**). Of these, the most abundant hydrous mineral is serpentine, $Mg_3Si_2O_5(OH)_4$, which forms by the hydration of olivine and pyroxene [e.g. *Bonatti*, 1976]. There are three serpentine mineral species: lizardite, antigorite, and chrysotile, in the order of abundance. Chrysotile and lizardite occur at temperatures of < 300°C, and antigorite is stable at higher temperatures (300-700°C) [*Ulmer and Trommsdorf*, 1995; *Evans*, 2004, and references therein].

Although the serpentinization of the subducting mantle prior to subduction is likely to occur locally along faults, serpentine contains 12.3 wt% H_2O and therefore is important to the fluid budget in subduction zones [*Pawley and Holloway*, 1993; *Ulmer and Trommsdorff*, 1995]. Antigorite that survives to ~200 km depth is replaced by another hydrous phase, phase A, which contains 11.8 wt% H_2O and is stable at higher temperature and pressure conditions than antigorite [*Schmidt and Poli*, 1998].

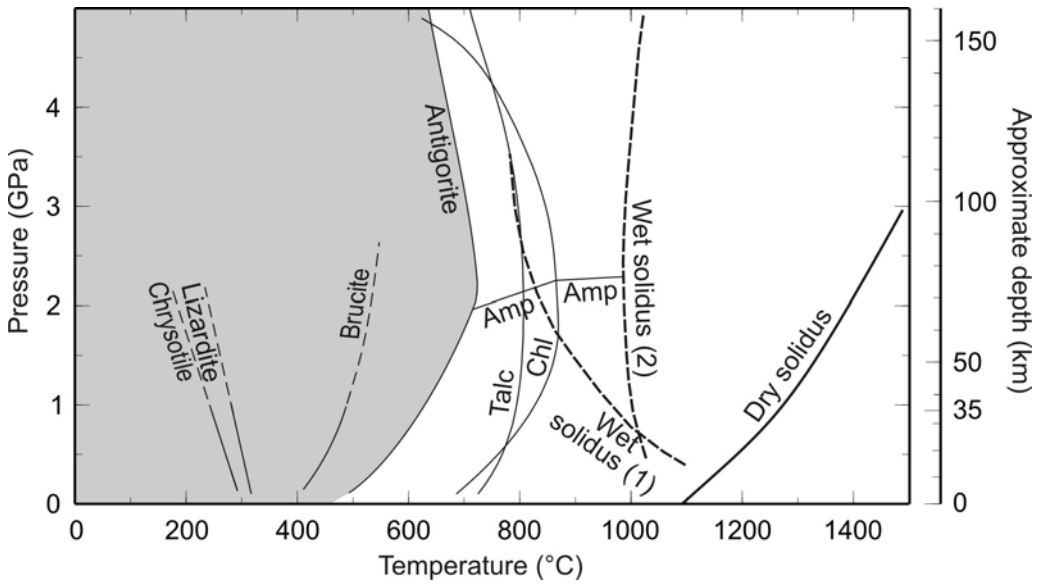

Figure 2.5. Phase diagram for H_2O-saturated mantle peridotite. Breakdown reactions of lizardite are from *Evans* [2004], chrysotile and brucite from *Evans* [1977], antigorite, chlorite (Chl) and amphibole (Amp) from *Schmidt and Poli* [1998], and talc from *Pawley and Wood* [1995]. One experimentally determined solidus (1) for H_2O-saturated mantle peridotite is from *Grove et al.* [2006], and (2) the other from *Schmidt and Poli* [1998]. The dry peridotite solidus was experimentally determined by *Takahashi and Kushiro* [1983]. See **Figure 2.3** for how the depth scale on the right is derived.

2.3.3. Serpentinization of the Mantle Wedge

In the forearc mantle wedge, hydrous minerals such as serpentine (antigorite, chrysotile, and lizardite), chlorite, talc, brucite, magnetite and amphibole can form, provided that the mantle wedge is cold and there is sufficient fluid supply from the dehydrating slab [*Hacker et al*, 2003a, b]. Of these hydrous minerals, serpentine mineral antigorite is expected to be the most abundant in a hydrated forearc mantle wedge at continental convergent margins [*Hyndman and Peacock*, 2003]. At ocean-ocean convergent margins, the mantle wedge overlies the subducting slab at very shallow

depths under a very thin (~7 km) oceanic crust. In its shallow part, the lower-temperature serpentine species chrysotile and lizardite are likely to be more abundant [*Evans*, 1977; *Evans*, 2004]. Fluid released from the subducting slab is likely to be silica-saturated, and the addition of silica-saturated fluid to silica-undersaturated mantle wedge material produces talc [*Peacock and Hyndman*, 1999]. Melting of the mantle due to the flux of aqueous fluid into the hot sub-arc mantle will be discussed in **Section 2.5.1**.

Given a stable thermal condition, the degree of serpentinization in the mantle wedge depends on the availability of aqueous fluid. Because the fluid source in the subduction zone is the dehydrating slab, the wettest part of the forearc mantle wedge should be its base where hydrous minerals are likely to be most abundant. The mechanism of fluid migration within the mantle wedge is a complex problem and will not be dealt with in this dissertation. However, some geological evidence [e.g. *Peacock*, 1987] supports that infiltration is likely to be controlled by fracture permeability, for which a number of mechanisms have been proposed, including hydrofracturing due to elevated pore fluid pressure [e.g. *Peacock and Hyndman*, 1999; *Seno*, 2005]. Serpentinization results in volume expansion [*Christensen*, 2004], which may induce stresses, promoting further fracturing and fluid migration [e.g. *Iyer et al.*, 2008] but may also seal fractures and reduce fracture permeability. The exothermic nature of serpentinization reactions, on the other hand, may cause a condition unfavourable for further serpentinization [*Peacock*, 1987]. These competing effects of serpentinization are yet to be investigated through laboratory experiments and numerical modelling.

Serpentinization results in a decrease in density and seismic velocities. The decrease in the velocity is more prominent for the S wave, resulting in an increase in the

ratio of P- to S-wave velocities (Vp/Vs) and hence a higher Poisson's ratio [*Christensen*, 2004, and references therein]. Serpentinization also results in increased magnetic susceptibility due to the formation of magnetite as a by-product of serpentinization [*Hyndman and Peacock*, 2003, and references therein]. High electrical conductivities are also expected in a hydrated mantle wedge because of the presence of magnetite and fluid [*Hyndman and Peacock*, 2003, and references therein]. Furthermore, volume expansion and density reduction due to serpentinization give rise to negative gravity anomalies.

Low Vp and Vs values observed in the Cascadia forearc mantle are interpreted as to indicate serpentinization (20-60%) [*Bostock et al.*, 2002; *Brocher et al.*, 2003; *Ramachandran et al.*, 2005]. This interpretation is supported by high-amplitude, long-wavelength positive magnetic anomalies and negative gravity anomalies in the Cascadia forearc [*Blakely et al.,* 2005]. Serpentinization of the forearc mantle wedge has also been inferred from seismic observations in Nankai (50-70%) [*Kamiya and Kobayashi*, 2000; *Seno et al.*, 2001], Kyushu (20-30%) [*Xia et al.*, 2008], northern Chile (0-12 %) [*Graeber and Asch*, 1999; *Carlson and Miller*, 2003], and Costa Rica (15-25%) [*Carlson and Miller*, 2003; *DeShon and Schwartz*, 2004], from magnetic and gravity anomalies in Alaska [*Saltus et al*., 1999], and from the presence of serpentine mud volcanoes in the forearc region of the Izu and Mariana margins [*Fryer*, 1996]. Note that the estimated degree of serpentinization represents an average value, and complete serpentinization may occur locally, especially along fractures and at the tip of the mantle wedge. The presence of a serpentinized forearc mantle wedge is proposed to explain the lack of velocity contrast between the continental crust and the underlying mantle in south-central (SC) Chile [*Groβ et al.*, 2008]. In contrast, a relatively dry mantle wedge corner and thus

a minor degree of serpentinization are reported for northern Hikurangi [*Eberhart-Phillips et al.*, 2008] and in most parts of NE Japan [e.g. *Miura et al.*, 2005]. There has been no investigation on mantle wedge serpentinization for the study regions of the other six of the seventeen subduction zones. Although further observations are required for the global distribution of mantle wedge serpentinization, it appears at present that evidence for serpentinization is more readily observed in subduction zones with warm slabs, possibly indicating a greater fluid supply beneath the forearc mantle wedge.

2.4. Seismic Activity in Subduction Zones

2.4.1. Distribution of Intraslab Earthquakes and Proposed Mechanism

In subduction zones, earthquakes occur along the plate interface (interplate earthquakes), in the overriding plate (mostly in the crust and thus often referred to as crustal earthquakes), and in the subducting slab (intraslab earthquakes). This dissertation focuses primarily on the thermal and petrologic conditions of intraslab earthquakes. Intraslab earthquakes occur over a wide depth range, extending to as deep as the base (660 km depth) of the mantle transition zone in some subduction zones [*Frohlich*, 1989, and references therein]. Intermediate-depth (< 300 km depth) and deep intraslab earthquakes are believed to be due to different mechanisms. In this study, I focus on the intermediate-depth intraslab earthquakes. See *Green and Burnley* [1989], *Kirby et al.* [1991], and *Kirby et al.* [1996b] for the studies of the deep earthquakes.

Stresses cause failure of geologic material, but they alone do not determine whether the failure occurs seismically or aseismically. Laboratory experiments indicate that the

high confining pressure at the depths of intermediate-depth intraslab earthquakes tends to inhibit seismic rupture of geologic materials. Transformational faulting is a proposed mechanism for deep earthquakes. Transformational faulting can occur due to a phase transformation of minerals propagating at seismic speeds [*Kirby*, 1987] or due to preferential alignment of minerals that facilitates seismic rupture [*Green and Burnley*, 1989]. However, while this mechanism can be at work in the deep slab through the phase transformation of olivine to spinel, the phase transformation of minerals found in the shallower part of the slab (< 300 km depth) does not cause transformational faulting [*Hacker et al.*, 2003a]. Shear instability involving rapid temperature increase and even melting is another possible mechanism that promotes earthquake rupture, but this mechanism is yet to be tested through laboratory experiments [*Ogawa*, 1987; *Kanamori et al.*, 1998]. Currently, the most widely accepted hypothesis is that fluid released during the dehydration of hydrous minerals in the subducting slab elevates pore fluid pressure, reducing the effective pressure and facilitating seismic rupture [e.g. *Kirby et al.*, 1996a]. This process is referred to as "dehydration embrittlement", a term originally used to describe a laboratory observation that fluid release causes an immediate change from ductile to brittle deformation. According to this hypothesis, the presence of fluid causes rock failure to occur seismically, controlling the distribution of intraslab earthquakes.

Intraslab earthquakes at relatively shallow depths occur in two sub-parallel bands (double seismic zone) in many subduction zones. They are thought to represent seismicity in the subducting crust and upper mantle separated by an aseismic core [e.g. *Hacker et al.*, 2003a]. The separation between the two bands tends to be greater for older and colder slabs, and the lower band is located several tens of kilometres away from the

slab surface in very old slabs (e.g. NE Japan) [e.g. *Hasegawa et al.*, 1994; *Brudzinski et al.*, 2007]. Dehydration embrittlement of the subducting crust and mantle is proposed to cause earthquakes in the upper and lower bands, respectively, although how the initially anhydrous oceanic mantle (**Section 2.3.2**) becomes hydrated to the depths of several tens of kilometres prior to subduction is not well understood [*Peacock*, 2001; *Yamasaki and Seno*, 2003].

The depth range of intraslab earthquakes varies greatly among subduction zones (**Figure 2.6**). For most of the seventeen subduction zones (**Figure 2.1**), the maximum depth of intraslab seismicity shown in **Figure 2.6** are obtained directly from the global earthquake catalog of *Engdahl et al.* [1998] (hereafter referred to as the EHB catalog), in which earthquake hypocentres are located using teleseismic networks. In northern Cascadia, Nankai, Kyushu, SC Chile, and Costa Rica, the number of intraslab

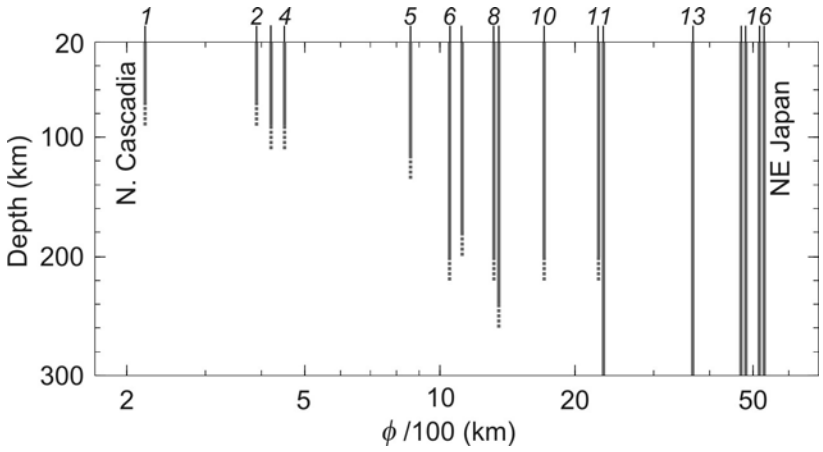

Figure 2.6. Variation in the observed depth range of intraslab seismicity (vertical lines) with the thermal parameter ϕ (**Table 2.2**). Dashed lines indicate uncertainties in the maximum depth. The ϕ values of the seventeen subduction zones (**Figure 2.1, Table 2.1**) are shown at the top.

earthquakes in the EHB catalog is small due mostly to the paucity of events that are large enough to be located by teleseismic networks. For these subduction zones, I infer the depth range from hypocentre locations of intraslab events determined by local networks (see **Table 2.2** for references). The maximum depth may be slightly underestimated because the earthquake catalogs used exclude events that do not meet all the criteria for hypocenter determination. Uncertainties in the maximum depth are expressed with dashed lines in **Figure 2.6**. The maximum depth increases with ϕ from 70 km to greater than 300 km. Dehydration reactions are expected to extend to greater depths in high-ϕ (colder) slabs than in low-ϕ (warmer) slabs [*Kirby et al.*, 1996a], and thus the increase in the depth of intraslab seismicity with ϕ (**Figure 2.6**) supports the hypothesis of dehydration embrittlement. Seismicity at > 300 km depths is hypothesized to be due to other mechanisms such as transformational faulting discussed above.

Dehydration embrittlement causes fault failure to be at seismic speeds in the subducting slab, but it is tectonic stresses that cause the faults to fail. The study of intraslab stresses is also a critical component of earthquake hazard analysis and subduction zone geodynamics [*Wada et al.*, 2009, submitted to *Journal of Geophysical Research*], although it is not included in this dissertation.

2.4.2. Episodic Tremor and Slip

In northern Cascadia, non-volcanic low-frequency seismic tremor occurs episodically in the forearc region [*Rogers and Dragert*, 2003]. The reported vertical distribution of tremor activity varies depending on the method applied to locate tremor

events [e.g. *Kao et al.*, 2005; *McCausland et al.*; 2005; *La Rocca et al.*, 2009], but in map view, they are around the tip of the mantle wedge corner (**Figure 1.2**). Similar tremor activity is also detected near the mantle wedge tip in Nankai [*Obara*, 2002] and is reported to be located along the plate interface [*Shelly et al.*, 2006].

In both Cascadia and Nankai, slow slip events occur along the plate interface downdip of the locked seismogenic portion of the subduction interface concurrently with the tremor [*Dragert et al.*, 2001; *Ozawa*, 2002; *Hirose and Obara*, 2005, 2006; *Wang et al.*, 2008]. The tremor and slow slip are together referred to as episodic tremor and slip (ETS). The ETS events occur roughly every 14 months in northern Cascadia and 6 months in Nankai and are not associated with regular high-frequency earthquakes [*Rogers and Dragert*, 2003; *Obara et al.*, 2004; *Shelly et al.*, 2006].

ETS-like events are also reported to occur in Mexico [*Larson et al.*, 2007; *Payero et al.*, 2008], Alaska [*Ohta et al*, 2006; *Peterson et al.*, 2007], and Costa Rica [*Larson et al.*, 2007]. However, these events exhibit characteristics that are different from ETS in Cascadia and Nankai, such as the lack of a strong temporal and spatial correlation between the tremor activity and slow slip. Silent slip events are abundantly observed in other subduction zones, including Hikurangi [*Douglas et al.*, 2005] and at the southern end of the NE Japan margin (Boso Peninsula) [*Sagiya*, 2004], but so far no tremor activity has been reported for NE Japan and Hikurangi where researchers have actively searched for tremor signals [*Ito*, personal communication, 2009; *Delahaye et al.*, 2009].

The mechanism of ETS remains unclear. Detailed studies of the waveforms of tremor in Cascadia [*Wech et al.*, 2007] and Nankai [*Shelly et al.*, 2006, 2007] indicate shear slip, but it is not known whether both tremor and slow slip are caused by interface

slip only. In both Cascadia and Nankai, seismic tomography indicates the presence of fluid in the ETS region, and thus ETS may be associated with the addition of fluid released by the dehydrating slab [*Kao et al.*, 2005; *Shelly et al.*, 2006]. Rate- and state-dependent friction laws have also been applied to explain the initiation and propagation of slow slip [e.g. *Liu and Rice*, 2005, 2007].

2.4.3. Tectonic and Thermal Implications of Crustal and Interplate Earthquakes

For the purpose of this dissertation, we are interested in what we can learn about frictional heating along the interface from interplate and crustal earthquakes. The amount of frictional heat generated along the interface is the product of shear stress on the fault and the fault slip rate *v*. The shear stress (τ) on a fault at failure is

$$\tau = \mu(1-\lambda)\sigma_n = \mu'\sigma_n \tag{2.1}$$

where μ is the coefficient of friction of the fault, μ' is the effective coefficient of friction, σ_n is the normal stress, and λ is the fluid pressure ratio,

$$\lambda = \frac{P_f}{P_l} \tag{2.2}$$

where P_f is the fluid pressure, and P_l is lithostatic pressure. A low μ' value of the fault results in low frictional heating.

The state of stress in the forearc crust inferred from crustal earthquakes can be used to constrain the strength of the subduction fault. Mechanical models of forearc stresses constrained by focal mechanism of crustal earthquakes show low strength of subduction faults [*Wang and He*, 1999; *Wang and Suyehiro*, 1999; *Lamb*, 2006; *Seno*, 2009].

Seismological and field observations [e.g. *Magee and Zoback*, 1993] and frictional heating studies [e.g., *Wang et al.*, 1995; *von Herzen et al.*, 2001] also indicate that subduction faults are weak and that the temporally and spatially averaged effective coefficient of friction of subduction faults is usually no greater than 0.05, typically around 0.03. The low μ' value of weak subduction faults results in low frictional heating.

The updip and downdip extent of the frictionally coupled, seismogenic portion of the plate interface is controlled by changes in the sliding behaviour of the material along the interface. Possible mechanisms for the changes in the sliding behaviour have been discussed extensively in the literature [e.g. *Vrolijk*, 1990; *Moore and Saffer*, 2001; *Saffer and Marone*, 2003; *Hyndman and Wang*, 1993; *Hyndman et al.*, 1997]. What is relevant to the present study is the downdip width of the seismogenic zone, along which most of the frictional heating occurs. The downdip width of the seismogenic zone has been estimated for a number of subduction zones on the basis of the distribution of thrust events [e.g. *Tichelaar and Ruff*, 1993; *Pacheco et al.*, 1993], geodetic data [e.g. *Le Pichon et al.*, 1998; *Wang et al.*, 2003; *Wallace et al.*, 2004; *Simoes et al.*, 2004], and tsunami modeling [e.g. *Baba et al.*, 2002]. However, there are typically large uncertainties of several kilometres in these estimates.

As will be discussed in **Section 3.2.2**, in the thermal models developed in the present study, I apply frictional heating along the interface from the surface to near the depth of the estimated downdip extent of the seismogenic zone where available, assuming a μ' value of 0.03 to be consistent with the concluded low strength of subduction faults. Although there are large uncertainties in the downdip width of seismogenic zones, given the low strength of the subduction fault and the shallow depths

(< 50 km depth) of the seismogenic zone reported for most subduction zones, the effect of frictional heating on the deeper part of the subduction zone, which is the focus of this dissertation research, is expected to be relatively small.

2.5. Arc Volcanism

2.5.1. Generation of Magmas Beneath the Volcanic Arc

Arc magmas are geochemically distinct from magmas generated in other tectonic settings such as the mid-ocean ridge (See **Section 2.3.1**). Relatively to MORB, arc magmas are enriched in fluid-mobile elements such as boron (B) and incompatible elements such as K and U [e.g. *Gill*, 1981]. They contain up to 6 wt% H_2O [*Johnson et al.*, 1994], whereas fresh MORB contains almost no water [*Pawlley and Holloway*, 1993].

Arc magmas are generated largely by hydration melting, that is, melting triggered by the lowering of mantle solidus due to the addition of fluid into the hot region of the mantle wedge [*Pawley and Holloway,* 1993; *Leeman*, 1996; *Gaetani and Grove*, 1998; *Ulmer*, 2001], although there is some evidence for (adiabatic) decompression melting of the upwelling mantle in the volcanic arc of some subduction zones [e.g. *Kohut et al.*, 2006]. The mechanism of hydration melting is supported by the relatively high water content and enrichment of fluid-mobile elements in arc lavas [*Ishikawa and Nakamura*, 1994; *Leeman*, 1996]. The rate of magma production is thus expected to depend strongly on the amount of fluid fluxing from the subducting slab. Variation in the enrichment of B

in arc lavas examined at several margins indicates greater fluid flux from the subducting slab (and sediments) for subduction zones with older slabs [*Leeman*, 1996].

How fluids are transported from the forearc to the high-temperature arc region is an important question. *Davies and Stevenson* [1992] suggested that fluid transfer occurs horizontally following a saw-tooth path across the mantle wedge by a series of hydration-dehydration reactions of amphibole. However, the time required for the lateral fluid transfer to the sub-arc region and the resultant magma geochemistry are inconsistent with experimental and geochemical constraints [*Schmidt and Poli*, 1998, and references therein]. An alternative mechanism is that fluid is transported by the subducting slab or downdip flow of hydrated material in the overriding mantle wedge to the sub-arc region, and the released fluid migrates upward to the melt source region due to its positive buoyancy. The proposed mechanisms of the upward migration include hydrofracturing [e.g. *Iwamori*, 1998] and porous flow along grain boundaries [e.g. *Mibe et al.*, 1999]. The distribution of fracture, connectivity of grain boundaries, and pressure gradient affect the ascent of the fluid, and the migration path may not be strictly vertical.

The amount of reduction in the melting temperature of mantle rocks due to the addition of H_2O reported in the literature varies dramatically [*Grove et al.*, 2006]. Two experimentally determined solidi for H_2O-saturated peridotite are shown in **Figure 2.5**. The one obtained by *Schmidt and Poli* [1998] indicates ~1000°C at 100 km depth, similar to the solidus determined by several other earlier studies [e.g. *Kushiro et al.*, 1968; *Green*, 1973; *Millhollen et al.*, 1974]. In contrast, the one more recent obtained by *Grove et al.* [2006] is significantly lower (~800°C) at this depth. *Grove et al.* [2006] explained that the lower melting temperature results from a longer duration of their experiments,

which allows co-existing minerals to approach near equilibrium. Their result is similar to that of *Mysen and Boettcher* [1975]. The large discrepancy between the various solidi is yet to be fully understood. The melting in the mantle wedge, however, is expected to occur at much higher temperatures than the above experimentally determined solidi because the mantle source is typically not fully saturated with H_2O as evidenced by the composition of arc lavas [e.g. *Ulmer*, 2001].

The PT conditions at which the melt equilibrates with mantle peridotite have been estimated through phase equilibrium experiments on arc lavas. For the Cascade arc in California, the equilibrium temperature is 1300-1450°C for the depth range of 36-66 km [*Elkins Tanton et al.*, 2001]. Thermobarometric data from the tectonically exhumed arc sections in Pakistan and south-central Alaska indicate that crystallization occurred at 980-1025°C at ~1.0 GPa (30-35 km depth) [*Kelemen et al.*, 2003]. These studies assume a steady-state geotherm for the PT path of the melt and the mantle, and the estimated mantle temperatures may represent high temperatures that are associated with transient states of melt or magma chambers and be higher than actual [*Kelemen et al.*, 2003]. On the basis of these petrological estimates with their uncertainties taken into account and the experimental constraints discussed above, it is widely agreed that mantle wedge melting temperatures should be greater than 1200°C [*Kelemen et al.*, 2003].

In some subduction zones such as Cascadia, Nankai, and Ecuador, in addition to flux melting of the mantle, partial melting of the top part of the subducting crust is also inferred from a low yttrium (Y) and ytterbium (Yb) content and high strontium/yttrium (Sr/Y) ratio [e.g. *Defant and Drummond*, 1990, 1993; *Morris*, 1995; *Bourdon et al.*, 2002]. Rocks that form from this type of magma are referred to as adakites. Melting of

the subducting crust requires very high temperatures as indicated by the solidus of wet basalt in **Figure 2.3** and is thought to occur when the subducting slab is young (< 25 Ma) and warm and/or the rate of shear heating is high [*Peacock et al.*, 1994]. The elevated level of trace elements such as beryllium (Be) and thorium (Th) in some arc lavas also suggests partial melting of subducted sediments [*Johnson and Plank*, 1999, and references therein].

2.5.2. Intensity of Arc Volcanism

The intensity of arc volcanism is highly variable among subduction zones. On the basis of the hypothesis that arc crust is formed through magmatism, arc magma production rates have been estimated indirectly from the growth rates of arc crust that are inferred primarily from seismic and gravity studies [e.g. *Dimalanta et al.*, 2002; *Hochstein*, 1995; *Taira et al.*, 1998]. These estimates depend on the inferred thickness and width of the crust across the arc. In the present study, instead of using indirect inferences on arc magma production rates, I consider the long-term volumetric volcanic output rate of a volcano or a unit length (100 km) of the volcanic arc in subduction zones compiled by *Crisp* [1984] and more recently by *White et al.* [2006] (**Table 2.2**). This rate accounts mainly for the extrusive portion of the arc volcanism, but a higher volcanic output rate is a reasonable proxy for a higher magma production rate because the latter is generally accompanied with the former. Among the volcanic output rates that were determined for a few volcanoes or margin segments of a given subduction zone, I choose one with the longest well-constrained history of activity so that the rate is based on

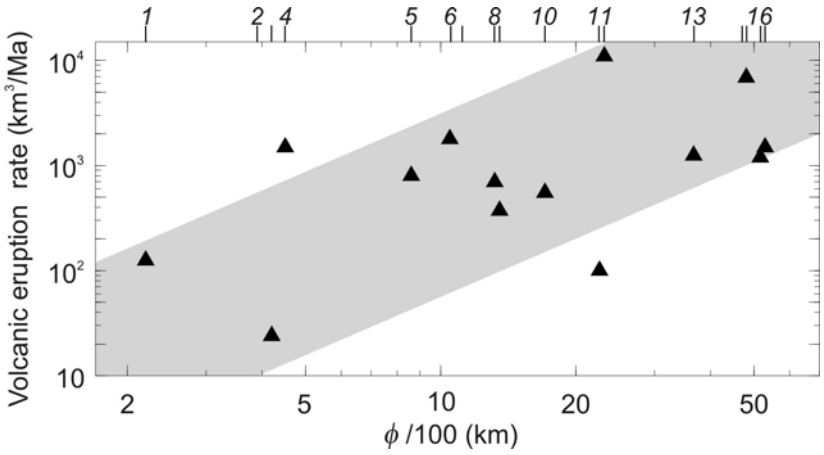

Figure 2.7. Variation in long-term volcanic output rates of volcanic arc (triangles) [*Crisp*, 1984; *White et al.*, 2006] with the thermal parameter ϕ (**Table 2.2**). The shaded area indicates the trend of increasing volcanic output rates with ϕ. The ϕ values of the seventeen subduction zones (**Figure 2.1, Table 2.1**) are shown at the top.

several eruption cycles and is closest to the long-term average. **Figure 2.7** shows that the rate of arc magma production has a strong tendency to increase with ϕ.

Because arc magmas are generated primarily by hydration melting, the rate of magma production is likely to be higher for subduction zones with a larger fluid flux from the subducting slab into the hot part of the overriding mantle. Therefore, the increase in arc magma production with ϕ is most likely due to the greater ability of colder slabs to carry fluids to the sub-arc depth. This is also supported by the observed variation in B (boron) enrichment of arc lavas as mentioned in **Section 2.5.1**. In some works, such as *Grove et al.* [2009], great emphasis is placed on the dehydration of mantle wedge material that was hydrated at a slightly shallower depth and then brought down to the sub-arc depth by wedge flow, but we think that fluid from the dehydrating slab directly beneath the arc is far more important. Region-specific processes such as intra-arc rifting and sediment

subduction to the sub-arc depth are likely to affect magma production and cause the large scatter of the magma production rates seen in **Figure 2.7**.

2.5.3. Configuration of Subduction Zones: Depth of the Slab Beneath the Arc

Arc volcanoes are distributed within a relatively narrow zone and are typically situated where the subducting slab is at ~100 km depth [e.g. *Tatsumi and Eggins*, 1995]. This relatively uniform slab depth beneath the arc led to the hypothesis that arc volcanism and thus magma generation is triggered by a depth-dependent dehydration reaction of amphibole in the subducting slab or mantle wedge at ~110 km depth [*Tatsumi*, 1986]. However, with this hypothesis it is difficult to explain why dehydration of other more abundant hydrous minerals in the subducting slab and mantle wedge would not trigger hydration melting at depths other than ~110 km. Other mechanisms are required to explain the uniformity of the sub-arc slab depth.

England et al. [2004] determined the depth to the top of intraslab seismicity beneath the arc for twenty-four margin segments using teleseismically determined intraslab earthquake hypocenter locations in the EHB catalog. I use this depth to approximate the sub-arc slab depth (H). The precise location of the intraslab earthquakes relative to the slab surface in the arc area is poorly known unless extensive seismic data (e.g. waves that are converted at or reflected from the slab surface or that are guided by the subducting crust) allow the detection of the slab surface, such as in NE Japan [e.g. *Zhao et al.*, 1997]. The inference of H from the intraslab seismicity thus results in a tendency to overestimate H, because the shallowest events beneath the arc may actually

be in the subducting mantle at some depth from the slab surface. A greater tendency of overestimating *H* is expected for older and colder slabs, in which intraslab seismicity can occur in a thicker band that extends deeper into the slab away from the slab surface (e.g. Mariana). A greater uncertainty in *H* is expected for a steeply dipping slab due to greater sensitivity of *H* to small changes in the position of the arc and horizontal location of intraslab earthquakes. Other source of uncertainties in *H* includes uncertainties in earthquake hypocenters.

The values of *H* determined by *England et al.* [2004] for the twenty-four margin segments range from 65 km to 130 km with the mean of ~100 km. About 54% of them fall in the range of 90-100 km, and 88% of them are in the 80-120 km range, confirming that *H* is relatively uniform. Similarly, 46% of individual volcanoes used to determine *H* in the twenty-four margin segments are situated where the slab is in the 90-100 km depth range, and 83% of them are situated where the slab is in the 80-120 km depth range. There results are shown in Figure 3c, confirming that the depths are commonly in the range of 90-110 km.

Syracuse and Abers [2006] determined *H* for fifty-one margin segments by delineating the slab surface based on the distribution of intraslab earthquakes in the EHB catalog. For the twenty-four margin segments investigated by *England et al.* [2004], the values of *H* determined by the two studies are similar (within 20 km) except for Java and Mariana. At these two margin segments, *H* determined by *Syracuse and Abers* [2006] is deeper than that determined by *England et al.* [2004]. The slab at these margins is relatively old and dips steeply, and the determination of *H* may be affected by the uncertainties discussed above. *Syracuse and Abers* [2006] also suggested that there might

be a need to adjust *H* to account for errors in hypocenter locations. The adjusted depths (*H'*) are systematically deeper than *H* (by up to ~40 km).

Besides the above two studies, *H* has also been determined independently using local seismic networks in some subduction zones. Where the local networks are dense and the slab geometry is relatively simple, the determination of *H* using the local networks is rather accurate and provides a "calibration" for the teleseismically determined *H*. At NE Japan, *H* determined using the very dense local network is ~100 km [e.g., *Nakajima et al.*, 2001]. The depths determined by both *England et al.* [2004] and *Syracuse and Abers* [2006] are also ~100 km while *H'* is 111 km. In northern Hikurangi, *H* determined using a similarly dense local network is ~85 km [*Reyners et al.*, 2007]. For the same location, the depths determined by *England et al.* [2004] and *Syracuse and Abers* [2006] are 110 km and 123 km, respectively, and *H'* is 147 km. The values of *H* determined by the two studies are in relatively good agreement with the "calibration" values. The adjustment made to produce *H'* does not appear to improve the deviation from the calibration values, and therefore we use *H* only in this study.

The *H* values determined by *England et al.* [2004] for most of the seventeen subduction zones investigated in this study are shown in **Figure 2.8**. Cascadia, Nankai, Mexico, Colombia-Ecuador, SC Chile, and Costa Rica were not included in their study due mostly to the paucity of intraslab seismicity directly beneath the arc. Of these margins, *Syracuse and Abers* [2006] determined *H* for SC Chile and Costa Rica, and we use their values for these two margins. For Cascadia and Mexico, I use *H* given by slab geometry models reported in the literature (**Table 2.1**). For the other two subduction zones, the slab geometry models reported in the literature is only for the shallow part of

the slab, most of which is based mainly on controlled-source seismic surveys. I extrapolate *H* from these models with the aid of limited intraslab earthquakes in the EHB catalog. Details of the slab geometry model for individual subduction zones will be provided in **Sections 4.2** and **5.3.2** as part of the description of mesh construction for thermal modelling. For northern Hikurangi, I use the value of *H* determined with the local network, but defining the precise location of the volcanic arc is somewhat problematic because of complications caused by on-going intra-arc and backarc rifting.

Figure 2.8 shows the tendency for the volcanic arc to form where the slab is around 100 km deep. The most striking characteristic of the arc location is its lack of a systematic dependence on ϕ, in contrast with other subduction zone processes discussed

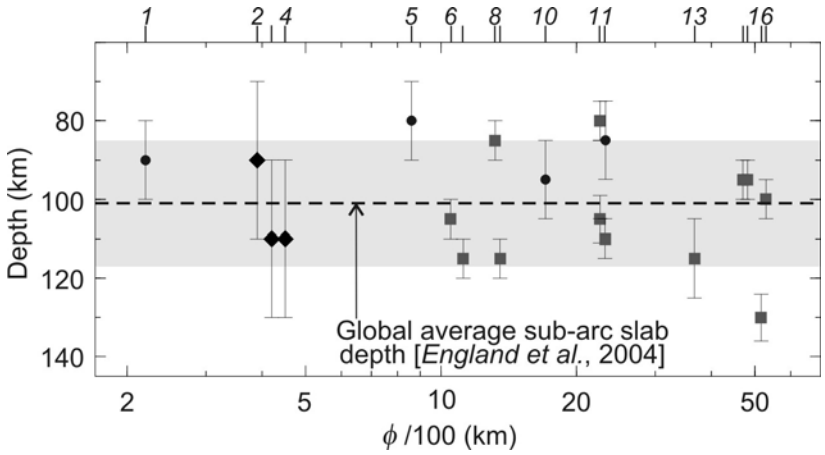

Figure 2.8. Variation in the sub-arc slab depths *H* with the thermal parameter ϕ (**Table 2.2**). The values indicated by squares and circles with error bars were determined by *England et al.* [2004] and other workers, respectively, and diamonds with error bars are estimated from the slab geometry model for the shallow part of subduction zones in the present study. The dashed line and the shaded area indicate the mean *H* of 101 km and the standard deviation of 16 km, respectively, obtained by *England et al.* [2004]. The ϕ values of the seventeen subduction zones (**Figure 2.1, Table 2.1**) are shown at the top.

above (**Figures 2.4**, **2.6**, and **2.7**). The independence of the arc location on ϕ is particularly intriguing considering the strong dependence of the intensity of arc volcanism on ϕ (**Figure 2.7**).

By comparing H with a range of subduction parameters, such as the age of the slab, subduction rate, and slab dip, both *England et al.* [2004] and *Syracuse and Abers* [2006] suggest that the kinematics of the subducting slab is at least partly responsible for the small variations in H. However, the first-order question of why the depth tends to be around 100 km and independent of the age of the slab is yet to be addressed.

Chapter 3

Method for Modelling the Effects of Weakened Subduction Interface on Mantle Wedge Flow and Thermal Structure

3.1. Mantle Wedge Rheology

At the temperature and pressure conditions in the upper mantle, the earth material deforms in a ductile manner primarily through diffusion and dislocation creep. Diffusion creep is a form of solid-state diffusive mass transfer, resulting from the movement of atoms within grains (Nabarro-Herring creep) or along grain boundaries (Coble creep) toward regions of lower pressure. Dislocation creep is a movement of line defects (dislocations) in crystalline lattice structure caused by applied stress and by thermodynamic forces due to heterogeneity of defect concentration [*Karato*, 2008].

The transition between diffusion and dislocation creep depends on various factors, such as shear stress, water content, and thermal gradient, but in general dislocation creep is thought to dominate in the shallow (< ~200 km depth) asthenospheric mantle [*Karato and Wu*, 1993]. This is supported by the seismic anisotropy observed in the upper mantle [*Savage*, 1999] which is thought to result from the reorientation of mineral grains, particularly olivine, during dislocation creep. The observations and interpretations of seismic anisotropy in the forearc mantle wedge will be discussed in **Section 5.8.2**.

The macroscopic relation between the deviatoric stress tensor (σ'_{ij}) and the strain rate tensor ($\dot{\varepsilon}_{ij}$) for diffusion-creep rheology is Newtonian:

$$\sigma'_{ij} = 2\eta\dot{\varepsilon}_{ij} \tag{3.1a}$$

where η is the viscosity of the fluid. The relation for the dislocation-creep rheology can be expressed in the same form as **Equation 3.1a** but using the effective viscosity η_e,

$$\sigma'_{ij} = 2\eta_e\dot{\varepsilon}_{ij}\,. \tag{3.1b}$$

The general flow law for both diffusion- and dislocation-creep under uniaxial loading is

$$\dot{\varepsilon}_a = A\left(\frac{\sigma_a}{\mu}\right)^n\left(\frac{b}{d}\right)^m \exp\left[-\frac{E+PV}{RT}\right] \tag{3.2}$$

where $\dot{\varepsilon}_a$ is axial strain rate and σ_a is axial stress, A is the pre-exponential factor, μ is shear modulus (80 GPa), b is the length of the Burgers vector (~0.5 nm), n is stress exponent, m is grain-size exponent, d is grain size, E is activation energy, V is activation volume, P is confining pressure, R is the universal gas constant (8.3145 J mol^{-1} K^{-1}), and T is absolute temperature [*Karato and Wu*, 1993]. In both diffusion and dislocation creep, the strain rate is highly sensitive to temperature. In diffusion creep, the strain rate increases linearly with stress, following the Newtonian flow law (n = 1) (**Equation 3.1a**), but decreases with grain size (m > 0). In dislocation creep, the strain rate increases nonlinearly with stress, following a power law (n > 1), but is independent of grain size (m = 0). The pressure term PV is very small relative to E and is neglected in this study.

For three-dimensional deformation, **Equation 3.2** is generalized to the form

$$\dot{\varepsilon}_{ij} = B\sigma'^{(n-1)}_{E}\sigma'_{ij} \tag{3.3}$$

where σ'_E is the effective deviatoric stress* and B is a parameter similar to A. To derive B from the experimentally determined rheological parameter values under uniaxial loading, let us first write **Equation 3.2** in a simpler form

$$\dot{\varepsilon}_a = A'\sigma_a^{\,n} \tag{3.4}$$

where $A' = \frac{A}{\mu^n}\left(\frac{b}{d}\right)^m \exp\left(-\frac{E}{RT}\right)$. Under uniaxial stress, the only non-zero components of σ'_{ij} are $\sigma'_{11} = \frac{2}{3}\sigma_a$ and $\sigma'_{22} = \sigma'_{33} = -\frac{1}{3}\sigma_a$, and those of $\dot{\varepsilon}_{ij}$ are $\dot{\varepsilon}_{11} = \dot{\varepsilon}_a$ and $\dot{\varepsilon}_{22} = \dot{\varepsilon}_{33} = -\frac{1}{2}\dot{\varepsilon}_a$. Using these expressions, σ'_E and the effective strain rate $\dot{\varepsilon}_E$† can be expressed in terms of $\dot{\varepsilon}_a$ and σ_a as $\sigma'_E = \frac{1}{3^{\frac{1}{2}}}\sigma_a$ and $\dot{\varepsilon}_E = \frac{3^{\frac{1}{2}}}{2}\dot{\varepsilon}_a$, respectively. By substituting these relations into **Equation 3.4**, we obtain

$$\dot{\varepsilon}_E = \frac{3^{\frac{n+1}{2}}}{2}A'\sigma'^{\,n}_{E}. \tag{3.5}$$

---

* The second invariant of σ'_{ij} is commonly used to define σ'_E, i.e., $\sigma'_E = \left(\frac{1}{2}\sigma'_{ij}\sigma'_{ij}\right)^{\frac{1}{2}}$.

† The second invariant $\dot{\varepsilon}'_{ij}$ is used to define $\dot{\varepsilon}'_E$, i.e., $\dot{\varepsilon}'_E = \left(\frac{1}{2}\dot{\varepsilon}_{ij}\dot{\varepsilon}_{ij}\right)^{\frac{1}{2}}$. For incompressible fluid, $\dot{\varepsilon}'_{ij} = \dot{\varepsilon}_{ij}$, and therefore $\dot{\varepsilon}'_E = \dot{\varepsilon}_E$.

Assuming that **Equation 3.5** holds also for three-dimensional deformation, we obtain

$$B = \frac{3^{\frac{n+1}{2}}}{2} A' . \tag{3.6}$$

Comparing **Equations 3.1b** and **3.3**, we have

$$\eta_e = \frac{1}{2B} \sigma'^{(1-n)}_E = 3^{\left(-\frac{n+1}{2n}\right)} 2^{\left(\frac{1-n}{n}\right)} \left(A'\right)^{-\frac{1}{n}} \dot{\varepsilon}_E^{\left(\frac{1-n}{n}\right)} . \tag{3.7}$$

For two-dimensional flow of an incompressible fluid ($\dot{\varepsilon}_{33} = 0$), σ_{33} is unknown, and σ'_E has to be calculated from the effective strain rate $\dot{\varepsilon}_E$ also assuming that **Equation 3.5** holds.

Other methods have also been used to cast **Equation 3.2** into a form suitable for two- and three-dimensional modelling:

$$\eta_e = \frac{1}{4}\left(\frac{4}{3A'}\right)^{\frac{1}{n}} \dot{\varepsilon}_E^{\left(\frac{1-n}{n}\right)} \qquad \text{[}\textit{Currie}\text{, 2004],}$$

$$\eta_e = \frac{1}{4}\left(\frac{4}{3A'}\right)^{\frac{1}{n}} \frac{1}{\sqrt{2}} \dot{\varepsilon}_E^{\left(\frac{1-n}{n}\right)} \qquad \text{[}\textit{Chen and Morgan}\text{, 1990], and}$$

$$\eta_e = \frac{\sigma}{\dot{\varepsilon}_E} = A'^{-\frac{1}{n}} \dot{\varepsilon}_E^{\left(\frac{1-n}{n}\right)} \qquad \text{[}\textit{van Keken et al.}\text{, 2002].}$$

For the wet olivine rheology, the above equations give effective viscosities that are 0.91, 1.2, and 3.3 times, respectively, that given by **Equation 3.7**. The differences between different methods are relatively small and are overshadowed by uncertainties in extrapolating laboratory results that were used to derive **Equation 3.2** to *in situ* conditions and in the effects of H_2O and melt contents on η_e.

A number of experimentally constrained rheological parameter values for olivine aggregates are available, including those that account for the effects of melts and aqueous fluids [e.g. *Hirth and Kohlstedt*, 2003]. However, for the purpose of this study, we are interested only in the overall nonlinear behaviour of the mantle wedge rheology, and the specific choice of parameter sets is unimportant. Therefore, I use the widely-cited parameter values reported by *Karato and Wu* [1993] for wet olivine assuming that sufficient amount of H_2O is supplied from the dehydrating slab to the mantle wedge (**Table 3.1**).

It has been observed experimentally that extremely high shear stress (> 200 Ma) causes the strain rate to increase exponentially during dislocation creep, and the stress-strain rate relation follows a Dorn law [e.g., *Tsenn and Carter*, 1987]. However, such high stress is rare in the mantle wedge, and thus the Dorn law is not used in this study.

Table 3.1. Rheological parameters for the upper mantle for uniaxial loading. Dry means water-free and wet means water-saturated conditions. Ref.: 1, *Karato and Wu*, 1993; 2, *Hilairet et al*, 2007.

Mineral/ Rock	Wet/ Dry	$\frac{A}{\mu^n}\left(\frac{b}{d}\right)^m$ ($Pa^{-n}\ s^{-1}$)	N	E (kJ/mol)	V (m^3/mol)	Ref.
Diffusion Creep						
Olivine	Dry	1.92×10^{-11}[a]	1	300	6.00×10^{-6}	1
Olivine	Wet	1.17×10^{-11}[a]	1	240	5.00×10^{-6}	1
Dislocation Creep						
Olivine	Dry	2.42×10^{-16}	3.5	540	2.00×10^{-5}	1
Olivine	Wet	3.91×10^{-15}	3	430	1.50×10^{-5}	1
Antigorite[b]	Wet	4.47×10^{-38}	3.8	89	3.20×10^{-6}	2

[a] A grain size of 1 mm is assumed.
[b] Parameters are best fit to the data at 1 GPa and 4 GPa.

3.2. Governing Equations: Viscous Flow and Heat Transfer

3.2.1. Viscous Flow Equations

In the model, flow velocities in the mantle wedge are computed by solving equations of mass and momentum conservation for an incompressible Boussinesq fluid. The equation for mass conservation is

$$\nabla \cdot \mathbf{v} = 0 \tag{3.8}$$

where $\mathbf{v}$ is the flow velocity, and the equation for the conservation of momentum is in a form of

$$\nabla \cdot \sigma' - \nabla P + \rho' g = 0 \tag{3.9}$$

where σ' is the deviatoric stress tensor, P is the dynamic pressure (i.e., the non-hydrostatic portion of pressure that is generated by flow), g is gravitational acceleration, and ρ' is the incremental density variation defined as

$$\rho' = -\rho_0 \alpha_v (T - T_0) \tag{3.10}$$

where ρ_0 is the reference density at a reference temperature T_0. The buoyancy (third) term on the left-hand side of **Equation 3.9** is omitted in this work as in the case of many other studies that model slab-driven mantle wedge flow. Changes in density due to metamorphic phase changes are relatively small and are also commonly neglected.

3.2.2. Heat Transfer Equation

Heat transfer through a material of thermal conductivity k, density ρ, and specific heat c_p should satisfy

$$\nabla \cdot \left(k \nabla T\right) - \rho \mathbf{c}_{\mathrm{p}} \left(\mathbf{v} \cdot \nabla T\right) + Q_H = \rho c_p \frac{\partial T}{\partial t} \tag{3.11}$$

where Q_H is the volumetric heat production [e.g. *Carslaw and Jaeger*, 1959]. The first term on the left-hand side represents conductive heat transfer, and the second term accounts for advective heat transfer. For steady-state heat transfer,

$$\nabla \cdot \left(k \nabla T\right) - \rho \mathbf{c}_{\mathrm{p}} \left(\mathbf{v} \cdot \nabla T\right) + Q_H = 0 . \tag{3.12}$$

In the models of the present work, Q_H includes radiogenic heat production (Q_{RH}), frictional heating (Q_{FH}) along the shallow brittle part of the subduction interface, and heat generation by viscous energy dissipation (Q_{VD}) along the deeper ductile part of the interface and in the mantle wedge. Endothermic dehydration reactions in the subducting slab and exothermic hydration reactions in the mantle wedge as heat sources or sinks depend on the distribution of hydrous phases in the subducting slab and the degree of hydration in the mantle wedge [*Peacock*, 1996]. On the basis of typical estimates for the H_2O content in the subducting slab and the mantle wedge, the thermal effect of these reactions is expected to be very small [*Peacock*, 1996, and references therein] and is neglected in the present study as is the case in most other subduction zone thermal modelling studies.

Heat generation along the plate interface is illustrated in **Figure 3.1**. Frictional heating is the product of fault slip rate v and shear stress τ (**Equation 2.1**),

$$Q_{FH} = \tau v = \mu' \sigma_n v . \tag{3.13}$$

Let us approximate σ_n by the weight of the overriding rock column and assume a value of 0.03 for μ', which is consistent with the concluded low strength of subduction faults as

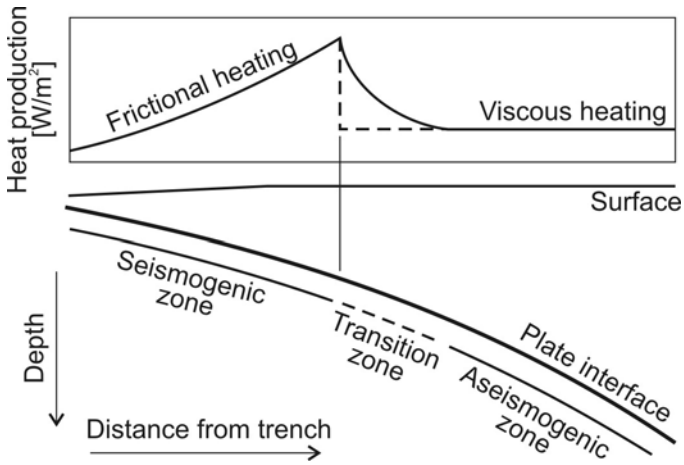

Figure 3.1. Schematic illustration of heat production along the plate interface in the model. The downdip end of frictional heating is assumed to correspond roughly to the downdip limit of the seismogenic zone in this study.

discussed in **Section 2.4.3**. Heat generated by viscous dissipation is the product of shear stress and shear strain rate (the second invariant of the stress and strain rate tensors),

$$Q_{VD} = \sigma'_E \dot{\varepsilon}_E . \tag{3.14}$$

In the model, the frictionally coupled part of the subduction interface where Q_{FH} is calculated is assumed to extend roughly to the estimated maximum depth of the seismogenic zone as mentioned in **Section 2.4.3**. Below this depth, shear stress and strain rate are calculated using the viscosity and strain rate of a thin layer of thickness h along the interface. I apply a dislocation-creep rheology to the interface layer over a short distance immediately downdip of the Q_{FH} segment and a uniform viscosity, which is to be investigated in **Chapter 4**, to the deeper part of the interface layer. Flow-law parameters for the layer dislocation-creep rheology are chosen to allow a smooth transition from the shallow Q_{FH} to the thin-layer Q_{VD} as shown in **Figure 3.1**. I use the parameter values determined for quartz diorite [*Hansen and Carter*, 1982; *Carter and*

Tsenn, 1987] except that I vary the value of the parameter *A* (**Equation 3.2**) to regulate the transition from Q_{FH} to Q_{VD} at a prescribed depth for a given model. The interface layer will be described in greater detail in **Section 3.5**.

Viscous energy dissipation occurs also in the mantle wedge and is included in models with a diffusion- or dislocation-creep rheology. However, increased temperature due to viscous energy dissipation decreases the (effective) viscosity of the mantle. This feedback between the two parameters renders viscous energy dissipation self-defeating. Thus, Q_{VD} is negligibly small as concluded by many other authors [e.g. *Currie*, 2004].

In some subduction zone thermal models, potential temperature, as opposed to real temperature, is used during the model calculation and then converted to real temperatures. In the studies by *Currie et al.* [2004a] and a number of other authors [e.g. *Peacock and Wang*, 1999], real temperature was used. *Currie* [2004] compared the difference between the mantle wedge temperatures calculated by using the "real temperature" and "potential temperature" approaches and found that the difference is small (<30-40°C at depths shallower than ~200 km depth). The difference is greater for the deeper part of the mantle wedge, and potential temperature needs to be used in large-scale thermal models [e.g. *Kincaid and Sacks*, 1997]. However, in regional-scale thermal models as developed in the present study, the "real temperature" approach is a reasonable approximation.

3.3. Numerical Method

I use the finite-element code PGCtherm. This code was developed by Dr. Jiangheng He at Pacific Geoscience Centre, Geological Survey of Canada and was previously benchmarked and used for subduction zone thermal modelling by *Currie* [2004] and *Currie et al.* [2004a]. The main advantages of this modelling code are its flexibility with model geometry and its efficiency in the numerical calculation.

In PGCtherm, the model domain is discretized into isoparametric quadrilateral elements. The lower and upper triangular decomposition method is used to solve the linear algebra equations after an optimal node-reordering. Dynamic pressure in the equation of motion (**Equation 3.9**) is underconstrained and introduces zeroes on the diagonal of the stiffness matrix. However, for the use of the lower and upper triangular decomposition method, the diagonal needs to be non-zero. To stabilize the pressure solutions, a conventional penalty function is introduced. The application of a penalty function requires that the interpolation function for pressure is at least one order lower than that of the velocity interpolation function. Thus, the code calculates the temperature and the velocity fields using nine-node elements while it calculates the pressure field using four-node elements (four corner nodes of the nine-node element). The quadratic nine-node elements allow much higher model resolution compared to linear elements of similar sizes. Except in the case of isoviscous mantle, a multi-corrector fixed-point iteration algorithm is used to solve the heat transfer and flow equations [*He*, 2008, personal communication]. Iteration is considered to have converged when the prescribed criteria for the velocity and temperature residuals at all nodes are met. These residuals are differences between consecutive iterations normalized by the maximum temperature and

velocity values (the L_∞-norm). There is little improvement in the flow and thermal fields once residuals become less than 10^{-6}, and I use this value as the convergence criteria for both temperature and velocity fields.

Several other numerical codes with different numerical methods are available for subduction zone thermal modelling. A community benchmarking exercise for these codes, including PGCtherm, shows that they are in reasonable agreement [*van Keken et al.*, 2008].

3.4. Boundary Conditions

The model consists of a non-deforming overriding plate, a subducting slab with prescribed motion, and a viscous mantle wedge in which the flow field is to be calculated (**Figure 3.2**). Heat transfer is assumed to be purely conductive within the overriding and

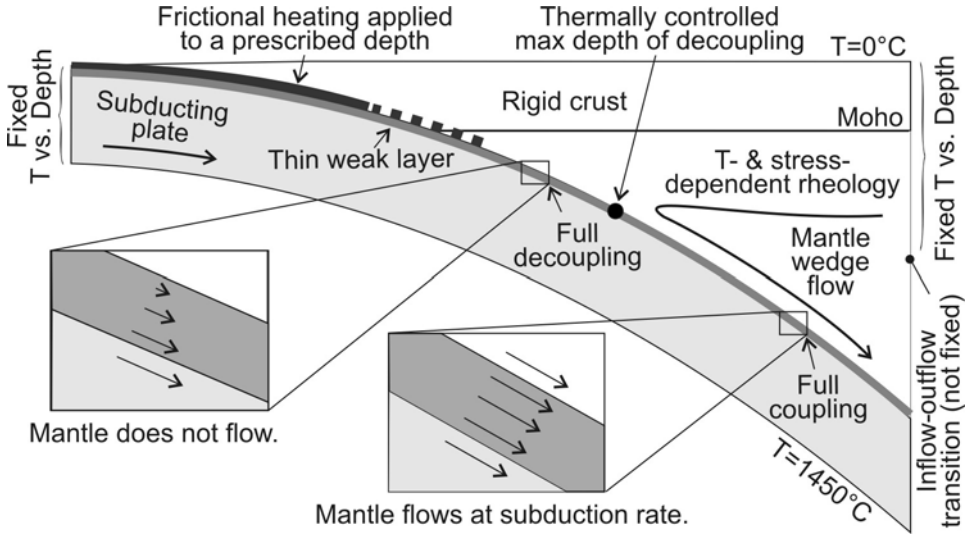

Figure 3.2. Schematic illustration of boundary and interface conditions for the thermal models. Insets show how the velocity varies across the thin layer along the plate interface in the cases of decoupling and coupling.

subducting plates, and only the subduction of the plate and mantle wedge flow cause advection of heat.

In the model, zero velocities are assigned to the crustal part of the overriding plate. However, in models with a realistic temperature- and stress-dependent mantle rheology, the actual base of the "rigid" upper plate is deeper, at a thermally controlled rheological transition determined as part of the solution.

Material in the mantle wedge is allowed to flow in across the shallow part of the backarc-side vertical boundary and out across its deeper part (**Figure 3.2**). The inflow-outflow transition depth is determined iteratively within the modelling code, and zero-velocity gradient in the flow direction is applied to this boundary. For the outflow part of the boundary, there is no conductive heat transfer in the flow direction ($\nabla T \cdot v = 0$). The velocity of the slab is assigned based on the plate convergence rate.

To the top and bottom boundaries of the model, I assign constant temperatures of 0°C and 1450°C, respectively, following *Peacock and Wang* [1999]. The age-controlled thermal structure of the incoming plate has a first-order influence on the thermal state of the subduction zone as discussed in **Section 2.1**. I calculate the geotherm for the incoming plate using the analytical plate cooling model of *Stein and Stein* [1992] (GDH1) for an appropriate plate age (**Figure 3.3**) unless otherwise specified. This model assumes a 95-km-thick lithosphere with a basal temperature of 1450 °C. Although I use a constant model grid thickness of 95 km for the subducting plate, the thermally relevant "slab thickness" is actually defined by the geotherm. In some subduction zones, the incoming plate is blanketed by a thick sediment cover. For these subduction zones, the

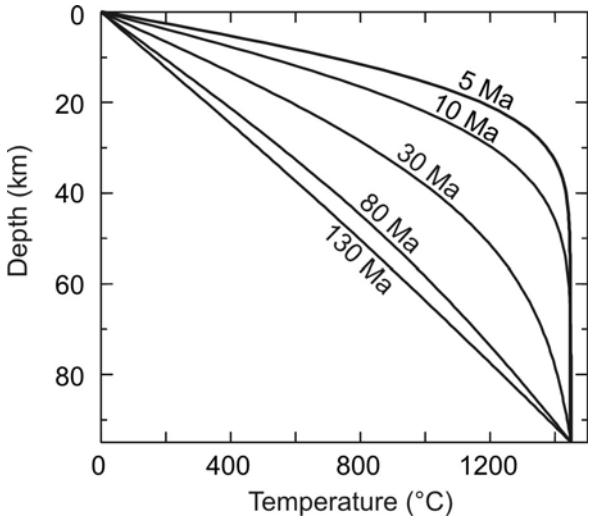

Figure 3.3. Geotherm for the trench-side vertical boundary calculated for oceanic lithosphere of various ages using the plate cooling model of *Stein and Stein* [1992] (GDH1). A half-spreading rate of 40 mm/yr is assumed.

effects of sedimentation on the thermal state of the incoming plate are included by using a different approach as will be described in **Section 5.3.3**.

For the shallow part of the backarc-side vertical boundary, I use a one-dimensional, steady-state, conductive heat equation to calculate the geotherm to give a regional average backarc surface heat flow value of a given subduction zone:

$$\frac{d}{dz}\left[k(z)\frac{dT}{dz}\right] + C(z) = 0 \tag{3.15}$$

where *T, z, C* and *k* are temperature, depth, radiogenic heat production, and thermal conductivity, respectively (**Figure 3.4**). For constant *k* and *C*, the integration of the above equation leads to

$$T(z) = T_0 + \frac{q_s}{k} z - \frac{C}{2k} z^2 \tag{3.16}$$

where T_o is surface temperature and q_s is surface heat flow. After a number of tests, however, we found that the assumed backarc surface heat flow has little effect on the forearc-arc mantle wedge thermal structure unless it is unreasonably low (<~50 mW/m^2). This is because the heat supply from the backarc to the forearc-arc region is controlled by the geotherm of the deeper flowing part of the backarc to be discussed in the following paragraph.

Following *Currie* [2004], I calculate the geotherm for the deeper part of the continental boundary above the inflow-outflow transition using a mantle potential temperature of 1295°C [*Ito and Katsura*, 1989] and an adiabatic temperature gradient of 0.3°C/km [*Turcotte and Schubert*, 2002]. In theory, the use of an adiabatic temperature gradient along this boundary is inconsistent with the assumption of the Boussinesq flow. I allow this inconsistency in order to curb the non-linearity of the problem and thus to simplify the model, as is commonly practiced in subduction zone thermal modeling. The effect of this simplification on the flow and thermal fields in the shallow part (< ~200-km depth) of the mantle wedge is very small [e.g. *Lee and King*, 2009]. The application of the adiabatic temperature gradient compensates for the missing effect of adiabatic heating in the model and therefore provides a good compromise. The adiabatic gradient is meant to represent vigorous mantle convection (buoyancy-driven flow) in the backarc region that supplies heat to the forearc-arc mantle wedge [*Currie et al.*, 2004a; *Currie and Hyndman*, 2006]. The intersection of the temperature profile calculated from **Equation 3.16** and the adiabatic mantle temperature profile is the transition depth from one profile to the other (**Figure 3.4**). This transition represents the transition from the rigid,

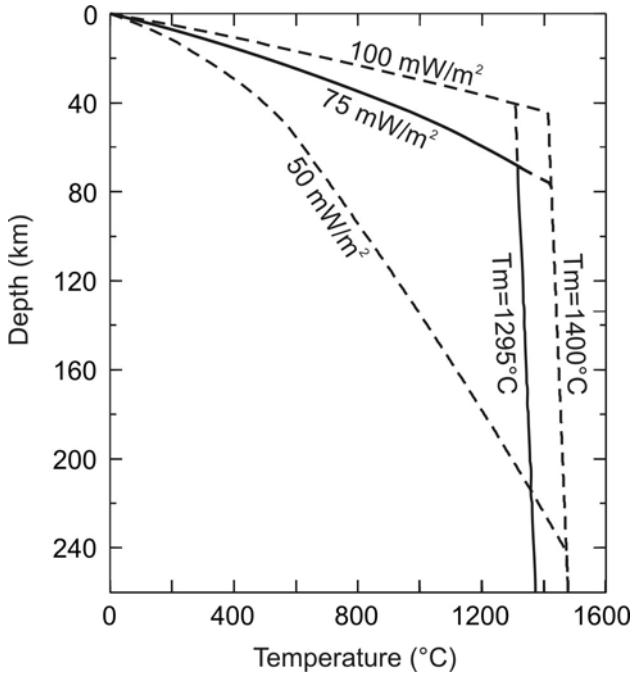

Figure 3.4. Geotherm for the backarc-side vertical boundary. The geotherm for the shallow part of the boundary is calculated by using **Equation 3.16** to give a surface heat flow of 75 mW/m^2 (solid line). Geotherms calculated to give 50 mW/m^2 and 100 mW/m^2 are shown by dashed lines. For the deeper portion of the boundary, the geotherm is calculated by assuming an adiabatic temperature gradient of 0.3 °C/km and a mantle potential temperature (Tm) of 1295 °C (solid line). A geotherm calculated by assuming the same adiabatic temperature gradient but Tm=1400°C (dashed line) is also shown for comparison.

conductive uppermost part of the mantle to a viscous, advecting deeper part of the mantle in the backarc region.

As *Currie et al.* [2004a] have shown, if the backarc-side boundary is placed far away from the arc, the model based on the temperature- and stress-dependent rheology predicts backarc heat flows that are significantly lower than observed. Vigorous small-scale buoyancy-driven flow is proposed as a mechanism for maintaining high heat flow in the backarc [*Currie et al.*, 2004a] as discussed in **Section 2.1.1**, and the transition from

the slab-driven flow regime in the forearc-arc region to the buoyancy-driven flow regime must take place somewhere in the arc and backarc region. Because this dissertation research focuses on the forearc-arc region, I assign the backarc-side vertical boundary at a short distance (100-150 km) landward of the arc and only simulate slab-driven flow.

Through a number of testing runs, I found that the assumed backarc surface heat flow has little effect on the forearc-arc mantle wedge thermal structure unless it is unusually low (<~50 mW/m^2) because the heat supply from the backarc to the forearc-arc region is controlled by the geotherm of the deeper flowing part of the backarc.

The mantle potential temperature reported in the literature ranges from 1280°C to 1400°C [*Kelemen et al*, 2003, and references therein]. The geotherm calculated with the upper bound mantle potential temperature of 1400°C is shown in **Figure 3.4** for comparison. I found that the use of a higher or lower mantle potential temperature within the reported range affects mantle temperatures mostly near the backarc boundary of the model, and its thermal effect is small in the forearc-arc region where the thermal field depends largely on the pattern of mantle wedge flow and thus the slab-mantle coupling.

3.5. Interface Layer for Simulating Slab-Mantle Decoupling

As discussed in **Section 2.2.1**, geophysical observations indicate that mantle flow is absent in most of the forearc mantle wedge and thus the subducting slab and the overriding mantle are decoupled. Various methods have been used to simulate slab-mantle decoupling in previous model studies. In *Currie et al.* [2004a], and also in *Peacock and Wang* [1999] and *van Keken et al.* [2002], a no-flow condition was imposed

on the most seaward part of the mantle wedge (**Figure 3.5a**). This "rigid corner" prevented mantle wedge flow from entering this region, resulting in a surface heat flow pattern consistent with that observed. *Conder* [2005] used an improved version of this approach in which the size and shape of the rigid corner are defined by a thermally controlled brittle-ductile transition. *Kneller et al*. [2005, 2007] and *Abers et al*. [2006] used a kinematically prescribed velocity discontinuity across the interface (**Figure 3.5b**). Full coupling or complete decoupling is accomplished by allowing the mantle material just above the interface to move at the slab velocity or be fixed, respectively, and any intermediate differential velocity represents partial decoupling. *Furukawa* [1993] used a free slip (i.e. zero shear stress) condition to simulate decoupling, so that there is no need to prescribe a differential velocity across the interface.

In the present work, I use a thin layer of low viscosity along the interface, in effect simulating a stress condition (**Figure 3.2**). This thin layer does not need to represent a

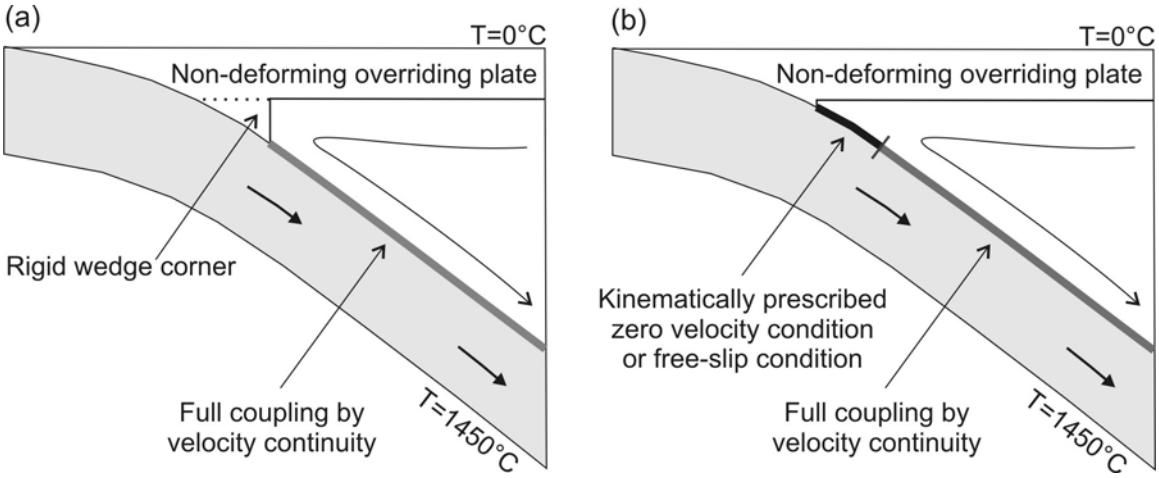

Figure 3.5. Schematic diagram showing (a) a rigid-corner model and (b) a model with a kinematically prescribed zero velocity condition or free-slip condition, to satisfy observed low surface heat flow in the most seaward part of the forearc region.

specific component of the subduction system, but it represents the collective effect of various mechanisms that weaken the interface. If the thin layer is less viscous than the overriding mantle, shear strain is localized within it, resulting in a sharp but continuous decrease in flow velocity across the layer. Complete decoupling, that is, the velocity decreases to zero across the layer, occurs when the layer is very weak. Full coupling occurs when the layer is as strong as or stronger than the overriding mantle. This is one step forward from the free-slip approach of *Furukawa* [1993] because it can accommodate a range of stress conditions from complete decoupling to full coupling.

Except for the purpose of illustrating how the layer rheology affects the flow pattern in the mantle wedge in **Section 4.4.4**, I use a uniform viscosity (η') for the interface layer to represent the strength of the subduction interface. This choice of layer rheology is arbitrary, but given the present state of knowledge of the actual processes along the interface, complex parameterizations do not necessarily provide more meaningful results. Furthermore, as will be shown in **Section 4.4.4**, the choice of layer rheology has little effect on the flow pattern in the mantle wedge with temperature- and stress-dependent mantle rheology. The geophysical meaning and implications of the layer viscosity will be discussed in **Section 4.4.5**.

A simplifying feature of an isoviscous layer is that its overall strength is the product of its viscosity and thickness. Because of this scaling relationship, the absolute value of the layer thickness or viscosity is unimportant. We choose to vary the degree of decoupling by using a fixed layer thickness and changing the layer viscosity.

In deciding the layer thickness to be used in the model, I ran a number of modelling tests. In applying the interface layer to a realistic curved slab shape, it is difficult to

maintain a constant layer thickness along the entire length of the slab due to the grid construction. If the layer is too thin (e.g. 10 m), a small fluctuation in layer thickness can result in oscillation in the flow field within the layer. If the interface layer is too thick (e.g. 1000 m), the flow velocity at the base of the mantle wedge over the fully coupled part of the interface is slightly slower than the imposed subduction rate. This is because the base of the mantle wedge is at large distance away from the bottom of the interface layer where the subduction rate is imposed and the top part of the layer behaves as if it is part of the mantle wedge. Thus, the use of a very thick interface layer leads to a poor approximation of the strength of the plate interface by the thin layer. Furthermore, to simulate a wide range of stress conditions in models with a temperature- and stress-dependent mantle rheology, a very thin or thick layer requires the layer viscosity to be unrealistically low or high, respectively, resulting in a strong contrast with the effective viscosity of the overriding mantle in some parts of the mantle wedge.

Through trial and error, I found that a layer thickness of 100 m is a good compromise. With a layer thickness of 100 m, the model is numerically stable over a wide range of layer viscosities (10^{16}-10^{23} Pa s), which is wide enough to simulate the full range of coupling conditions (i.e. from full coupling to decoupling) in models with a temperature-dependent mantle rheology. Also, the shape of the layer needs to be as smooth as possible, particularly for the purpose of examining the stress condition along the interface between the layer and the overriding mantle (**Chapter 4**).

Figure 3.6 schematically shows possible forms of downdip decoupling termination as controlled by the strength contrast between the interface layer and the mantle wedge. With a hypothetical isoviscous mantle wedge (**Figure 3.6a**), the strength contrast is

uniform, such that decoupling can be terminated only by limiting the downdip length of the interface layer. With a more realistic temperature-dependent mantle wedge rheology, the mantle strength decreases with increasing temperature and hence depth (**Figure 3.6b**), and decoupling is terminated where the strength contrast disappears. In this case, the downdip length of the interface layer has no effect as long as it extends beyond the temperature-controlled termination depth. The scenario in **Figure 3.6c** is a hybrid of those in **Figures 3.6a** and **3.6b**. A very weak layer can be used to simulate complete decoupling over the length of the layer extending to the prescribed maximum depth of decoupling. The free-slip decoupling model of *Furukawa* [1993] can be viewed as an end-member case of this model (zero layer viscosity). In the scenario shown in **Figure 3.6d**, the layer has the same rheology as the mantle wedge, but is much weaker. Similarly to that in **Figure 3.6a**, decoupling can be terminated only by truncating the interface layer

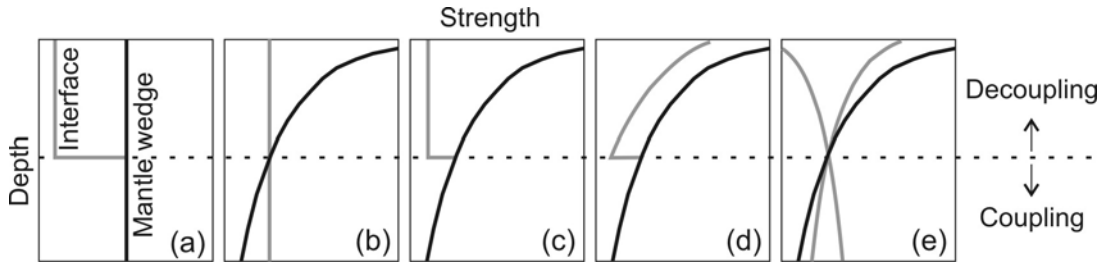

Figure 3.6. Different idealized forms of downdip decoupling termination. (a) Uniform interface strength and isoviscous mantle wedge. An increase in interface strength terminates decoupling. (b) Uniform interface strength but temperature-dependent mantle wedge rheology. The termination of decoupling is thermally controlled. (c) A hybrid of (a) and (b). (d) Similar to (c), but the interface has the same rheology as but is weaker than the mantle wedge. (e) Other combinations of interface and mantle strength profiles.

at some depth. **Figure 3.6e** shows other possible combinations of layer and mantle wedge rheology.

If there is a velocity discontinuity at the mantle wedge tip, it results in a singularity. By comparing the analytical corner flow solution of *Batchelor* [1967] and the numerical modelling results obtained by using PGCtherm, *Currie* [2004] showed that with the use of a high node density in the region, PGCtherm can model the pressure and velocity fields in the mantle wedge tip with high accuracy. The accuracy of different numerical codes in modeling the near-singularity behaviour in the mantle wedge tip was also investigated in a community benchmarking exercise [*van Keken et al.*, 2008].

In the present study, the near-singularity behaviour at the mantle wedge tip causes small oscillation in the flow within the interface layer regardless of the degree of slab-mantle decoupling. However, this oscillation dissipates quickly over a short downdip distance (a few elements) as long as a reasonably fine mesh is used in the mantle wedge tip, and the oscillation has little effect on the rest of the flow field. Similar near-singularity behaviour potentially occurs at the transition from decoupled to coupled interface, where the mantle starts to participate in the flow. In such cases, I use a fine mesh in the transitional area.

Some feedback effects of the hydration of the mantle wedge on slab-mantle coupling that are not included in the model are expected to occur in nature. A slight reduction in the interface strength due to, for example, high pore fluid pressure, causes mantle wedge flow to slow down, resulting in a cooler condition at the base of the mantle wedge and facilitating the formation of hydrous minerals. Although the amount of fluid released by the cold slabs at shallow depths may be too small to serpentinize the entire

mantle wedge, there is likely some fluid released to form serpentinites at the base of the mantle wedge. The increase in the amount of hydrous minerals then causes further weakening of the interface, and there is likely to be a positive feedback between these two factors. If there is sufficient fluid supply, the serpentinization of the overriding mantle wedge results in positive buoyancy due to the low density of serpentinite compared to the surrounding peridotite. The positive buoyancy works against the downward mantle flow in the forearc mantle wedge, discouraging mantle wedge flow and leading to a cooler and more favourable condition for further serpentinization.

Chapter 4

Model for Northern Cascadia: The Effects of Slab-Mantle Coupling

In this chapter, I apply the modelling approach described in **Chapter 3** to the northern Cascadia subduction zone (**Figure 4.1**) to investigate the effects of slab-mantle coupling on mantle wedge flow and the thermal structure. I will begin by providing a brief summary of the tectonic setting in northern Cascadia and describe the slab geometry, model parameters, and heat flow observations that are used to constrain the thermal model. I first present a model using a simple isoviscous mantle wedge and then a model using diffusion- or dislocation-creep rheology. I also test the effects of a cooler subducting slab on mantle wedge flow by using otherwise the same model set-up as for northern Cascadia. The results will show that a maximum depth of decoupling of 70-80 km depth best explains the surface heat flow observations in northern Cascadia. Part of the modelling results presented in this chapter formed the basis for the study by *Wada et al.* [2008], and the model developed in this chapter was also adopted by *James et al.* [2009] in investigating the viscosity of the upper mantle in relation to glacial isostatic rebound in northern Cascadia.

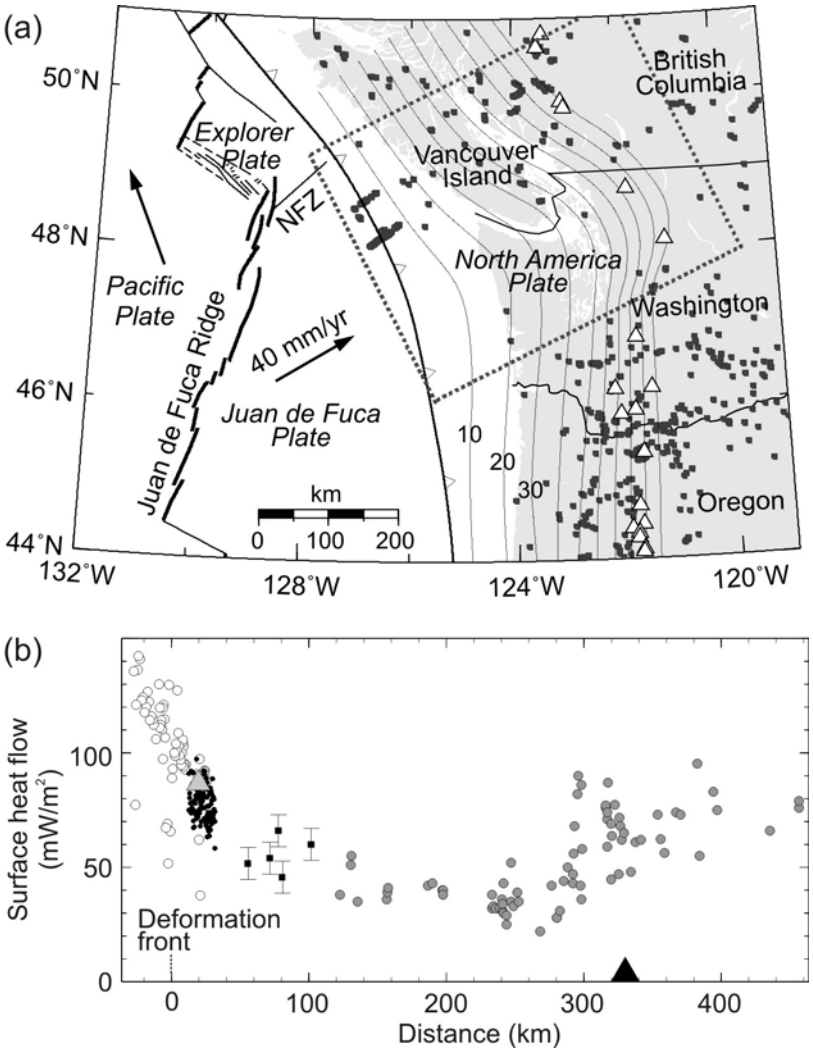

Figure 4.1. (a) Northern Cascadia subduction zone. Solid arrows indicate plate motions relative to North America [*DeMets et al.*, 1990, 1994; *Wilson*, 1993]. NFZ: Nootka fault zone. Thin lines are depth contours (km) of the surface of the subducting Juan de Fuca slab [*McCrory et al.*, 2004]. Open triangles represent arc volcanoes. Small grey squares are surface heat flow measurements. Dotted rectangle indicates the corridor for the northern Cascadia model. (b) Surface heat flow in the study area. Small black dots, white circles, squares, and the grey triangle are heat flow values obtained from bottom-simulating reflectors, marine probes, shelf wells, and an ODP borehole, respectively [*Davis et al.*, 1990; *Lewis et al.*, 1992; *Hyndman et al.*, 1993; *Wang et al.*, 1995]. Grey circles are heat flow observations complied by *Currie et al.* [2004a]. Solid triangle represents the regional average location of the volcanic arc in northern Cascadia.

4.1. Tectonic Setting of the Northern Cascadia Subduction Zone

The subduction of the Farallon plate beneath the North America plate started more than ~150 Ma along the Cascadia margin [*Riddihough*, 1984]. Currently, the Juan de Fuca plate, a northern remnant segment of the Farallon plate, subducts northeastward beneath North America at ~40 mm/yr [*DeMets et al.*, 1990, 1994] (**Figure 4.1**). In northern Cascadia, the minimum age of the Juan de Fuca plate along the margin is ~4 Ma off the central part of Vancouver Island, and the age increases southward to ~11 Ma off Oregon [*Wilson*, 1988, 1993]. The subduction of this young and warm plate makes Cascadia one of the warmest subduction zones in the world [e.g. *Hacker et al.*, 2003a]. Its warm thermal regime is also attributed to the relatively slow convergence rate [*Peacock*, 1996] and the thick (~3 km) blanket of sediments that insulates the underlying warm oceanic crust of the Juan de Fuca plate [*Davis and Hyndman*, 1989; *Hyndman and Wang*, 1993].

4.2. Model Geometry and Model Parameters for Northern Cascadia

For the shallow portion (< 50 km depth) of the subduction zone beneath southern Vancouver Island (**Figure 4.1**), several different models for the shape of the subducting Juan de Fuca plate have been proposed, depending on the interpretation of a thick zone of strong seismic reflectors referred to as the E reflectors, a deeper reflector referred to as the F reflector, and the depth of intraslab earthquakes relative to the slab surface [e.g. *Hyndman et al.*, 1990; *Flück et al.*, 1997; *Nedimovic et al.*, 2003; *Calvert*, 2004; *Nicholson et al.*, 2005; *Audet et al.*, 2009]. For the entire forearc-arc region of Cascadia,

McCrory et al. [2004] constructed a geometry model for the subducting slab by compiling published wide-angle seismic reflection and refraction data for the shallow part of the slab and intraslab earthquake hypocenters and teleseismic tomographic images of seismic velocity structures for the deeper part (**Figure 4.1**). Beneath Vancouver Island, the slab in their model is slightly shallower than but otherwise similar to those of *Hyndman et al.* [1990] and *Flück et al.* [1997], in which the slab surface is placed at the F reflector a few kilometres below the E reflectors. Their model is also compatible with the slab interface inferred from the Moho reflector of the subducting slab beneath northern Washington [*Preston et al.*, 2003].

In this study, I use the slab geometry model of *McCrory et al.* [2004], which is the most widely accepted, to obtain the regional average slab geometry for the region outlined by a box in **Figure 4.1**. Differences in the proposed geometry models for the shallow part of the subduction zone are yet to be reconciled, but the effects of the slab geometry at shallow depths on mantle wedge flow are minor and are not critical to the purpose of this research. Seismological studies of the region [e.g. *Ramachandran et al.*, 2004, 2005] indicate that the crust of the overriding plate is 30-35-km thick.

A typical finite-element mesh for the northern Cascadia model consists of about 7000-8000 elements of variable sizes (dimensions ranging from ~1 m to ~10 km) (**Figure 4.2**). The total number of temperature nodal points is about 30,000. Details of the mesh vary between different test cases to allow optimal distributions of element density.

Following *van Keken et al.* [2002] and *Currie* [2004], I assume specific heat of 1250 J/kg K and use typical values of rock densities for the model domain (**Table 4.1**). The upper crust in the forearc region of northern Cascadia consists of geologically

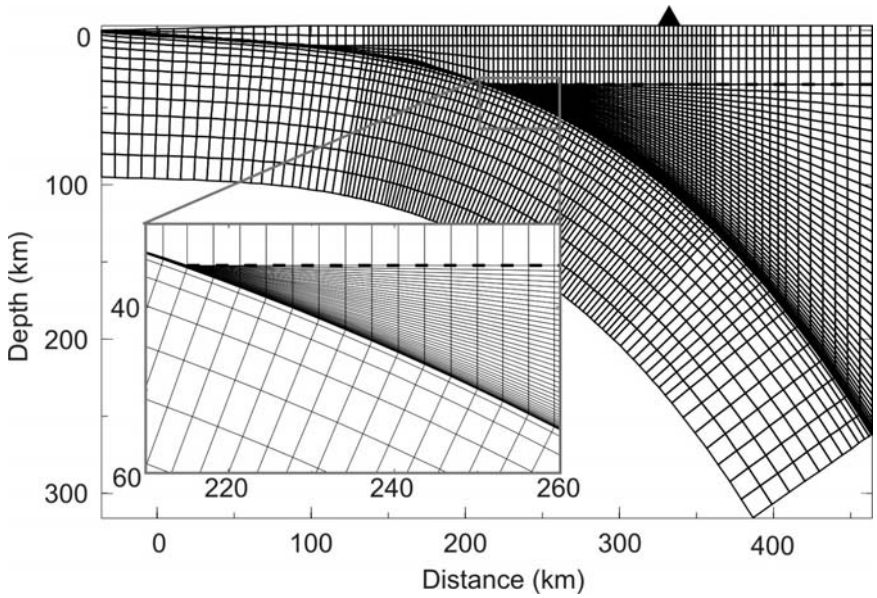

Figure 4.2. A typical finite element mesh used in this chapter for the northern Cascadia model. The triangle on top represents the average location of the volcanic arc. The mesh used for a model of fully-coupled interface is much finer in the mantle wedge corner than shown here.

distinct terranes, Cresent, Pacific Rim, and Wrangellia (**Figure 4.3**) [*Hyndman et al.*, 1990; *Monger and Price*, 2002, and references therein]. These terranes are composed primarily of mafic material and contain significantly lesser amounts of radiogenic elements than average continental material [*Lewis et al.*, 1988]. The estimated values of the thermal properties of these terranes have been summarized previously in accordance

Table 4.1. Density and thermal properties used in the models

Property	Material	Value
Density (kg/m^3)	Continental crust	2750
	Mantle and oceanic crust	3300
Thermal conductivity (W/m K)	Continental crust	2.5
	Mantle and oceanic crust	3.1
Radiogenic heat production (μW/m^3)	Continental upper crust	0-1.3*
	Continental lower crust	0.4
	Mantle and oceanic crust	0.02

* See **Table 4.2** for more detail.

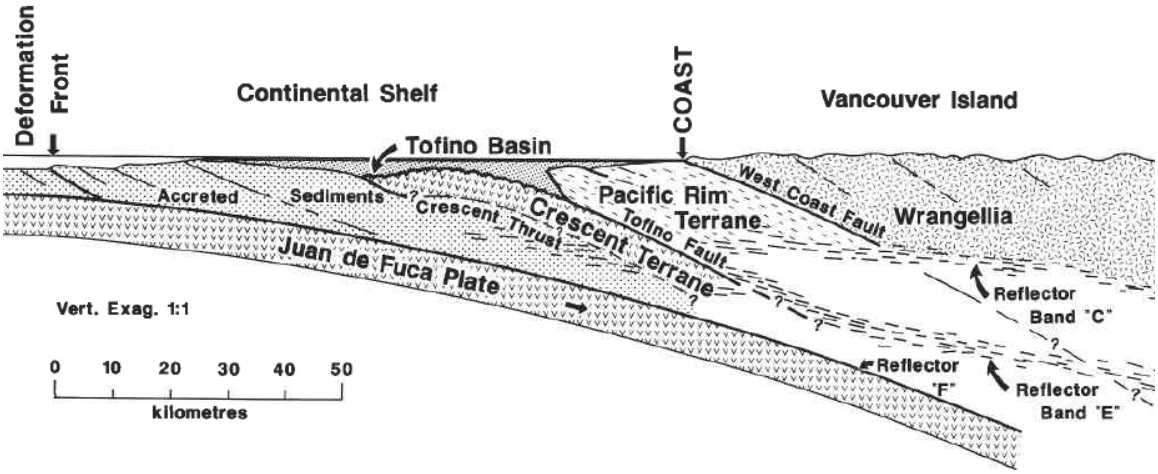

Figure 4.3. Geological cross section for the Vancouver Island margin [*Hyndman et al.*, 1990].

with the terranes (**Table 4.2**) and used to model the thermal structure [*Hyndman and Wang*, 1993, and references therein]. Following *Hyndman and Wang* [1993], I assign radiogenic heat production rates in the forearc crust as summarized in **Table 4.2** for models developed in this chapter. The exact locations of the transition between different rates depend on the grid construction. For the upper crust in the arc and backarc regions, I use a typical continental rate of 1.3 $\mu W/m^3$, which is consistent with the correction made

Table 4.2. Thermal properties of terranes in the forearc region of northern Cascadia from *Hyndman and Wang* [1993, and references therein] and radiogenic heat production rates used in the models in this chapter.

	Hyndman and Wang [1993]		This study	
Geologic unit	Thermal conductivity (W/m K)	Heat production ($\mu W/m^3$)	Distance from the deformation front (km)	Heat production ($\mu W/m^3$)
Sediment	1.0-2.0	0.6	-36-48	0.6
Cresent	2.0	0.0	48-99	0.4
Pacific Rim	2.5	0.0	99-287	0.2
Wrangellia	3.0	0.1-0.6	287-302	0.6
			302-362*	0.9
			362-464*	1.3

* The model of *Hyndman and Wang* [1993] did not extend to the volcanic arc.

to the heat flow observations by *Currie* [2004] as will be discussed in the next section. The thermal conductivity also varies among different terranes and generally increases landward to a typical continental crust value, but the effect of the variation on the results is relatively small, and thus I use a constant conductivity of 2.5 W/m K in this chapter.

As mentioned in **Section 4.1**, the incoming Juan de Fuca plate is blanketed by a 3-km-thick sediment cover [*Davis and Hyndman*, 1989]. The sediment cover insulates the plate, increasing the temperature of its top part. However, its effect on the slab at depth is expected to be negligibly small and will not affect the thermal field in the mantle wedge. Therefore, in this chapter, the oceanic-side geotherm is calculated by using the GHD1 model [*Stein and Stein*, 1992] for an 8-Ma oceanic lithosphere without the effect of sedimentation (**Section 3.4**). The 8 Ma is an average of the age of the incoming plate in the model corridor. Models in **Chapter 5** will include the effect of sedimentation. The geotherm applied to the backarc-side vertical boundary is calculated to give the northern Cascadia regional average backarc surface heat flow of 75 mW/m^2 (See **Section 3.4** for how the geotherm is calculated).

Different plate models [e.g. *Rddihough*, 1984; *DeMets et al*., 1990, 1994; *DeMets and Dixon*, 1999] give different convergence rates in northern Cascadia, and the estimates range from 39 to 45 mm/yr. Following *van Keken et al.* [2002] and *Currie et al.* [2004a], I use a rate of 45 mm/yr in the northern Cascadia model developed in this chapter. The frictionally coupled part of the subduction interface where Q_{FH} is calculated is assumed to extend from the trench to ~15 km depth (downdip extent of the seismogenic zone) except in the cold-slab case, in which it extends to 35 km depth (the continental Moho in northern Cascadia).

4.3. Observational Constraints: Surface Heat Flow

The primary observational constraint for the thermal model is surface heat flow as discussed in **Section 2.2.1**. In all subduction zones, surface heat flow is low in the forearc and high in the arc region, indicating a cold forearc mantle and a hot sub-arc mantle. The surface heat flow values in the model corridor are shown in **Figure 3.1b**.

The abruptness of the landward heat flow rise must be caused by local, near-surface processes such as magma emplacement associated with arc volcanism [*Lewis et al*., 1992; *Blackwell et al*., 1990a, b] and cannot be accounted for in the regional-scale models used in this study. Near-surface processes can greatly increase surface heat flow, but it is difficult to think of a mechanism for these processes to decrease surface heat flow systematically. Therefore, when using the heat flow values to constrain the model, we focus on explaining why the observed heat flows are low in most of the forearc region.

In northern Cascadia, there are relatively dense surface heat flow measurements (**Figure 4.1a**). *Currie* [2004] compiled 1675 published heat flow measurements for northern Cascadia. The measurements in southwestern Canada are from *Davis and Lewis* [1984], *Lewis et al.* [1988; 1992], and *Hyndman and Lewis* [1999], and those in the U.S. are from the Global Heat Flow Data Base (*GHFD*) [*Pollack et al.*, 1993; *Global Heat Flow Database*, 2004]. The variations in the radiogenic heat production of the upper crust of the overriding plate in the arc and backarc regions are large, ranging from 0.8 to 3.1 $\mu W/m^3$, resulting in large variations in surface heat flow values. These variations do not represent variations in the thermal state of the underlying mantle wedge [*Currie*, 2004]. Therefore, *Currie et al.* [2004a] corrected the measurements in the arc and backarc

regions to a uniform radiogenic heat production rate of 1.3 $\mu W/m^3$. The estimated uncertainties for these heat flow values are ±10-20% [*Currie*, 2004].

Since the focus of *Currie* [2004] and *Currie et al.* [2004a] was on the thermal state of the backarc region, offshore measurements were excluded from her compilation except for 6 measurements made in shelf wells offshore of Vancouver Island. In this research, I have included offshore surface heat flow, which consist of surface heat flow values determined from marine probe measurements [*Davis et al.*, 1990], petroleum exploration wells [*Lewis et al.*, 1988; 1991], and an ODP borehole [*Westbrook et al.*, 1994], and those derived from the depths of a bottom simulating reflector (BSR) in the accretionary prism [*Hyndman et al.*, 1993]. BSRs represent the base of the gas hydrate stability zone. Temperature at the BSR depth can be estimated from experimentally determined pressure and temperature conditions of gas hydrate stability and used to determine heat flow. In the compilation of *Wang et al.* [1995], the BSR-derived and borehole heat flow values on the accretionary prism were corrected for the effect of prism growth and fluid expulsion using the model of *Wang et al.* [1993]. The estimated uncertainties for these offshore surface heat flow values are 5-10% [*Davis et al.*, 1990; *Hyndman et al.*, 1993; *Wang et al.*, 1995].

Another fundamentally important observational constraint for the thermal model is the petrological constraint for the mantle temperature beneath the volcanic arc. As discussed in **Section 2.5.1**, geochemical data and thermobarometry measurements on arc lavas and xenoliths exhumed from the lower crust or upper mantle depths indicate that the sub-arc mantle temperature is > 1200°C. As will be shown below, the sub-arc mantle temperature depends largely on the seaward extent of mantle wedge flow and thus on the

maximum depth of decoupling (MDD). Therefore, the petrological constraint for the sub-arc mantle temperature is useful in validating the MDD.

4.4. Modelling Results

4.4.1. Isoviscous Mantle Wedge and Isoviscous Interface Layer

I first use a mantle wedge of uniform viscosity η (scenario in **Figure 3.6a**) to illustrate how the interface layer in the numerical model defines the degree of decoupling. The results of this simple model will provide guidance for interpreting models with a more realistic mantle wedge rheology which will be discussed in the following sections. For the isoviscous model, I let the interface layer extend to 70 km depth, the same as the depth of the bottom of the "rigid corner" of *Currie et al.* [2004a]. The strength contrast between the layer and the isoviscous mantle wedge is measured simply by the ratio of the layer and mantle viscosities η'/η.

If $\eta'/\eta \geq 1$, there is no strength contrast, and the interface is fully coupled (**Figure 4.4a**). In this fully coupled model, the mantle material immediately above the slab moves down with the slab at the convergence rate, and hotter mantle material moves from the backarc into the wedge corner to replace the downgoing material, resulting in relatively high mantle wedge temperatures. The stream lines of the mantle wedge flow are relatively evenly distributed, and the resultant flow pattern is similar to that of the analytical corner flow solution, except for the effects of slab curvature.

A viscosity contrast of $\eta'/\eta = 10^{-2}$ leads to partial coupling over the length of the interface layer (**Figure 4.4b**), resulting in a slight reduction in flow velocities over the

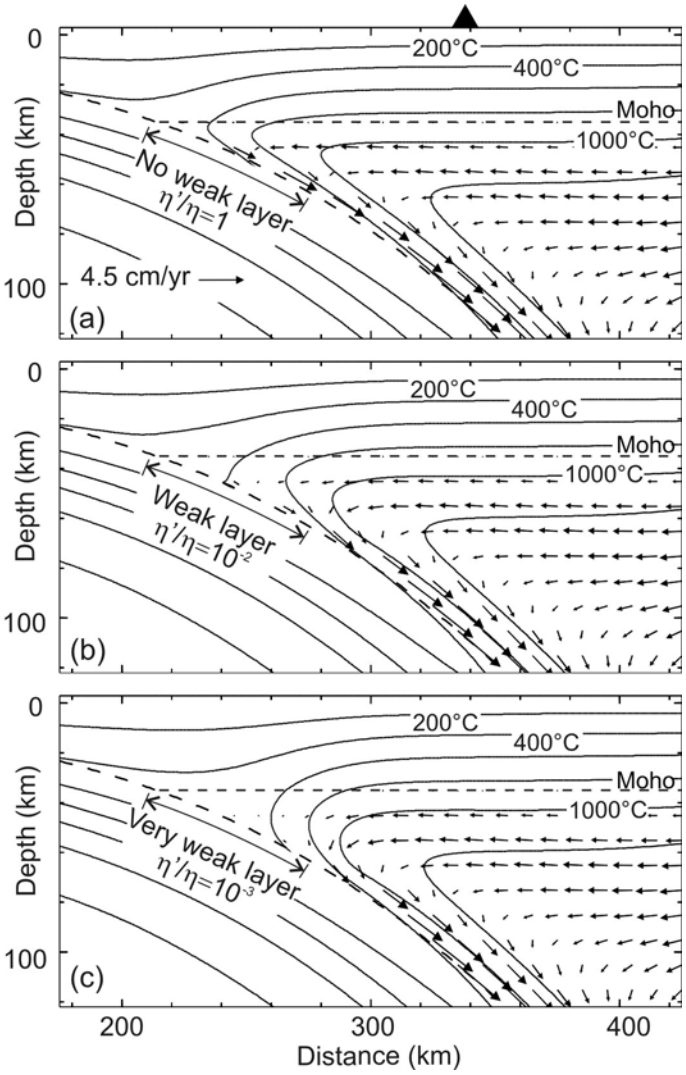

Figure 4.4. Temperature and flow velocities (arrows) in models with an isoviscous mantle wedge of viscosity η and an isoviscous interface layer of viscosity η' that extends to 70 km depth. (a) Full coupling, (b) partial decoupling, and (c) almost complete decoupling over the interface layer. Each model is labeled with the strength contrast η'/η used. The triangle at the top represents the average location of the volcanic arc at northern Cascadia.

layer and mantle wedge temperature. A viscosity contrast of $\eta'/\eta = 10^{-3}$ causes nearly complete decoupling, and the mantle wedge overlying the zone of decoupling is nearly stagnant (**Figure 4.4c**). Without hotter material moving in, the nearly stagnant wedge

corner is cold (**Figure 4.4c**) with temperatures comparable to those of a rigid corner imposed in models with an isoviscous wedge [e.g. *van Keken et al.*, 2002; *Currie et al.*, 2004a]. Further decrease in the value of η'/η causes little change to the modelling results except that the forearc mantle wedge becomes completely stagnant. The above results show that full decoupling occurs with $\eta'/\eta > 10^{-3}$ for a 100-m-thick interface layer.

The flow velocities at the base of the mantle wedge in the above three models illustrate the change in the flow velocity with the prescribed viscosity contrast (**Figure 4.5**). Even if the viscosity contrast is large ($\eta'/\eta > 10^{-4}$) and causes decoupling, the velocity near ~70-km depth is non-zero due to the influence of the mantle flow immediately downdip of the interface layer.

4.4.2. Diffusion-Creep Mantle Wedge and Isoviscous Interface layer

A diffusion-creep rheology is strongly temperature-dependent, and applying this rheology to the mantle wedge makes the model nonlinear due to the feedback between

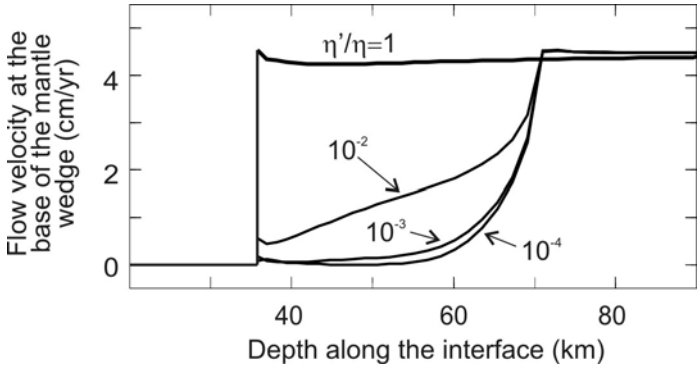

Figure 4.5. Flow velocity at the base of the isoviscous mantle wedge with an isoviscous interface layer extending to 70 km depth calculated by models shown in **Figure 4.4**. Each model is labeled with the strength contrast η'/η used.

the mantle strength and temperature. In this section, I present models with a diffusion-creep rheology to examine the effects of this temperature-dependence on slab-mantle decoupling and mantle wedge flow. I use the experimentally determined diffusion creep flow-law parameters for wet olivine (**Table 3.1**).

As discussed in **Section 3.1**, a dislocation-creep rheology is more appropriate for the mantle wedge at < 200 km depths. Models with a dislocation-creep rheology will be presented in the following two **Sections 4.4.3** and **4.4.4**. A dislocation-creep rheology depends not only on temperature but also on stress, increasing the nonlinearity of the model. The models with a diffusion creep rheology to be presented in this section will be useful for interpreting the effect of increased nonlinearity on slab-mantle decoupling in the models presented in the following two sections.

As discussed in **Section 3.5**, with a temperature-dependent mantle rheology, the downdip termination of decoupling can be thermally controlled, and therefore models presented in the rest of this chapter are of the type shown in **Figure 3.6b** with the interface layer extending along the entire length of the slab. With a diffusion-creep rheology, the viscosity of the mantle is non-uniform, and the viscosity contrast η'/η varies along the interface. I use the layer viscosity η' alone to represent the overall degree of coupling.

With a diffusion-creep mantle rheology, an interface layer viscosity $\eta' > 7\times10^{19}$ Pa s causes little viscosity contrast and decoupling except for a small segment at the wedge tip (**Figure 4.6a**). Compared to the isoviscous mantle wedge (**Figure 4.4a**), the wedge flow is focused in a narrow high-temperature, low-viscosity zone, consistent with the modelling results obtained with a diffusion-creep rheology in other studies [e.g. *Honda*,

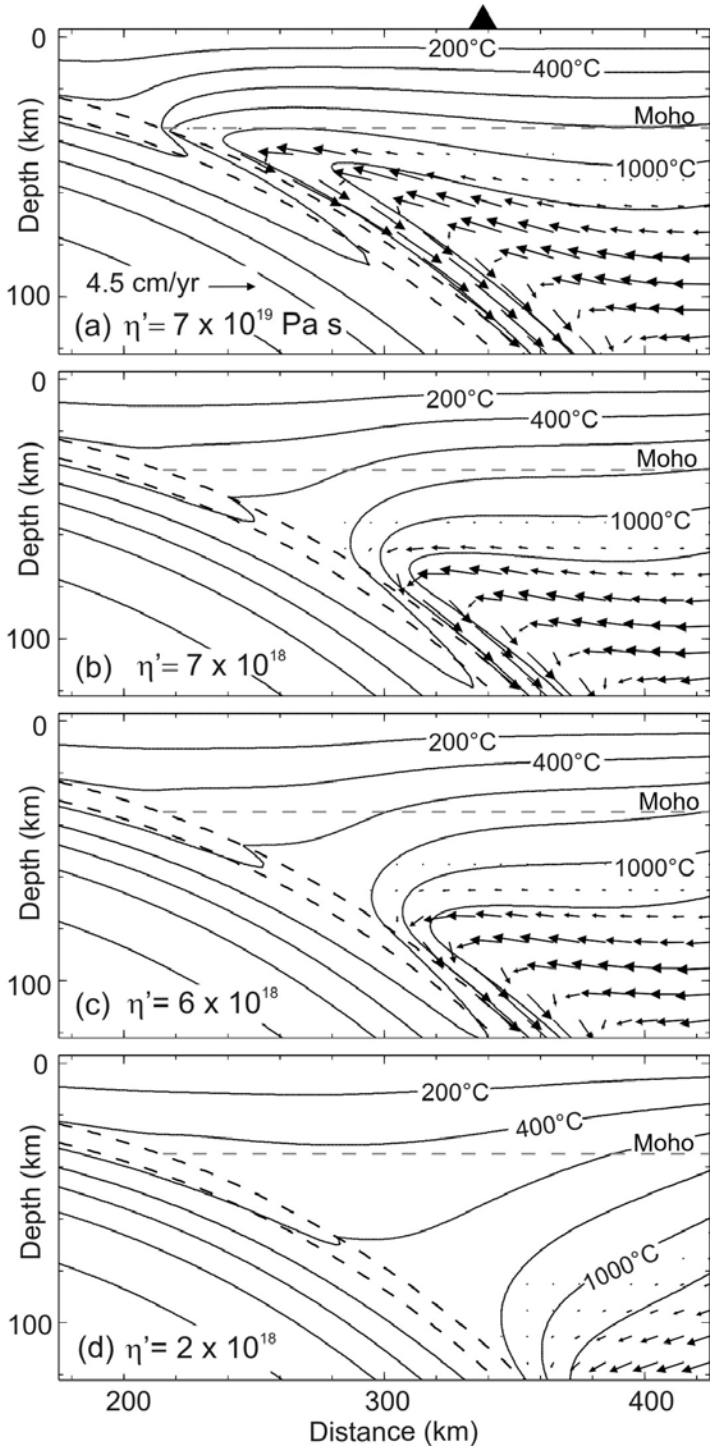

Figure 4.6. Temperature and flow velocities (arrows) in models with a diffusion-creep mantle wedge rheology and an isoviscous interface layer of viscosity η' that extends along the entire length of the slab. (a) Full coupling, (b) decoupling to ~70 km depth, (c) decoupling to ~80 km depth, and (d) decoupling to ~120 km depth. Each model is labeled

1985; *Furukawa,* 1993]. The focusing of flow results from the nonlinear feedback between temperature and η. The focused flow can bring in hotter material from greater depths towards the mantle wedge corner than does the more evenly distributed flow in the isoviscous mantle wedge, resulting in much higher mantle wedge temperatures.

A slight reduction in η' weakens the interface and causes flow velocities in the mantle wedge to decrease near the low-temperature mantle wedge corner where η is the highest and the viscosity contrast is the greatest. The reduction in flow velocities due to a weakened interface causes less heat to be advectively transported from greater depths and the backarc. The resultant decrease in temperature causes an increase in η, leading to greater viscosity contrast between the mantle wedge and the interface layer and thus further interface weakening. This nonlinear feedback between temperature and η causes nearly complete decoupling over the weakened part of the interface, resulting in a bimodal flow behaviour: the mantle either does not flow at all or flow at a full rate that is with slab velocity. With decreasing η', the MDD deepens and the stagnant part of the mantle wedge expands, but the bimodal flow behaviour is persistent (**Figure 4.6b**, **c** and **d**). The bimodal behaviour is more clearly illustrated in **Figure 4.7**, which shows flow velocity along the base of the mantle wedge. The velocity is virtually zero over the

---

(**Figure 4.6 caption continued**)
with the interface layer viscosity (Pa s) used. The frictional heat along the interface is terminated at ~15 km depth as discussed in **Section 4.2**, and heat production downdip of this depth is by viscous energy dissipation, which is greater for a stronger interface layer.

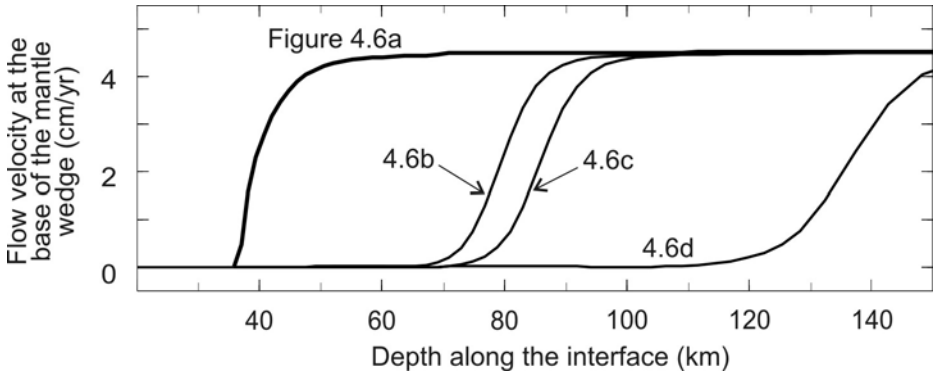

Figure 4.7. Flow velocity at the base of the mantle wedge with a diffusion-creep mantle rheology and an isoviscous interface layer calculated by models shown in **Figure 4.6**.

weakened part of the interface and is the plate convergence velocity over the coupled part. This flow behaviour is in contrast with an isoviscous mantle wedge that may flow at a reduced velocity above a weak interface (**Figure 4.5**) and also in contrast with models with a prescribed differential velocity (partial decoupling) in the forearc [e.g. *Kneller et al*, 2005]. The modeling results show that partial decoupling occurs in the transition from the decoupled to coupled interface but over a relatively broad depth range of about 20 km (**Figure 4.5**).

4.4.3. Dislocation-Creep Mantle Wedge and Isoviscous Interface Layer

In this section, I examine the flow pattern in the mantle wedge with the more realistic dislocation-creep rheology. I use rheological parameter values determined for dislocation creep of wet olivine (**Table 3.1**). This of the type shown in **Figure 3.6b** as in the previous section, and the depth of decoupling is thermally controlled. The main

difference of this model from that described in **Section 4.4.2** is that the mantle rheology depends not only on temperature but also on stress, making the problem more nonlinear.

An interface layer viscosity $\eta' \geq 3\times10^{19}$ Pa s leads to full coupling for practically the entire slab-mantle wedge interface (**Figure 4.8a**). The flow pattern is similar to that of the diffusion-creep rheology model in previous section except that the focusing of mantle flow is slightly more pronounced due to the additional nonlinear feedback between stress and the mantle rheology, resulting in slightly higher mantle wedge temperatures.

Decoupling occurs in models with $\eta' < 3\times10^{19}$ Pa s, and the MDD increases with decreasing η' (**Figures 4.8b, c,** and **d**). With a dislocation-creep mantle rheology, η' is smaller than that required to cause the same degree of decoupling with a diffusion-creep mantle rheology (**Figure 4.8c**). This is because the nonlinear feedback between temperature, stress, and η_e, makes the mantle wedge corner weaker than with diffusion creep.

For comparison, model results for an older (130 Ma) and colder slab are also shown in **Figure 4.8**. To ensure that the age of the incoming plate is the only difference in model set-up, I use the same model geometry. For a given MDD, the flow pattern in the mantle wedge is similar to that of a warm-slab model. The mantle material immediately above an old slab is colder than above a young slab, resulting in a slightly higher η_e in the mantle wedge. Because of the stronger mantle wedge, the layer viscosity that causes decoupling does not need to be as low as for the warm-slab models.

Similar to the diffusion-creep mantle wedge described in **Section 4.4.2**, the mantle over the weakened interface is almost completely stagnant, resulting in the bimodal flow behaviour. As discussed in **Section 4.4.2**, this is due to the nonlinear feedback between

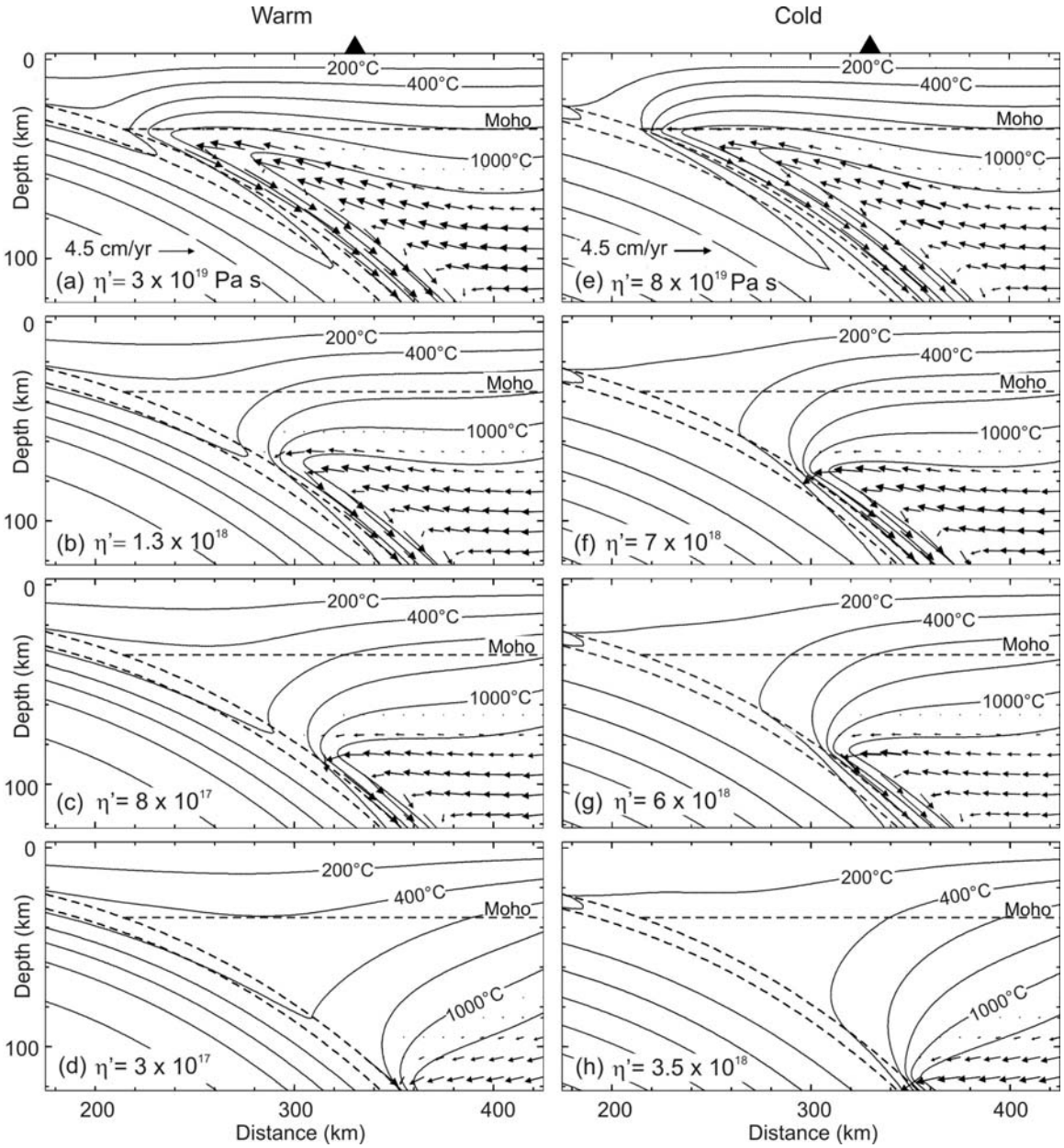

Figure 4.8. Temperature and flow velocities (arrows) in models with a dislocation-creep mantle wedge rheology and an isoviscous interface layer of viscosity η' that extends along the entire length of the slab. (a) Full coupling, (b) decoupling to ~70 km depth, (c) decoupling to ~80 km depth, and (d) decoupling to ~120 km depth in warm-slab (8 Ma) models. Models shown in **Figures 4.7b** and **c** are preferred for northern Cascadia (**Section 4.4.4**). (e) Full coupling, (f) decoupling to ~70 km depth, (g) decoupling to ~80 km depth, and (h) decoupling to ~120 km depth in cold-slab (130 Ma) models. Each model is labeled with the interface layer viscosity (Pa s) used.

temperature and the mantle strength. However, the bimodal flow behaviour is more pronounced in the dislocation-creep mantle wedge in that the transition from the decoupled to coupled part of the interface is sharper (**Figure 4.9a**) compared to that in the diffusion-creep mantle wedge (**Figure 4.7**). The more pronounced bimodal flow behaviour is caused by the greater nonlinearity due to the stress-dependence as well as temperature-dependence of the mantle rheology. A colder slab causes a larger temperature gradient between the stagnant and the flowing parts of the mantle wedge, resulting in a sharper decoupling-coupling transition and thus more pronounced bimodal flow behaviour (**Figure 4.5b**).

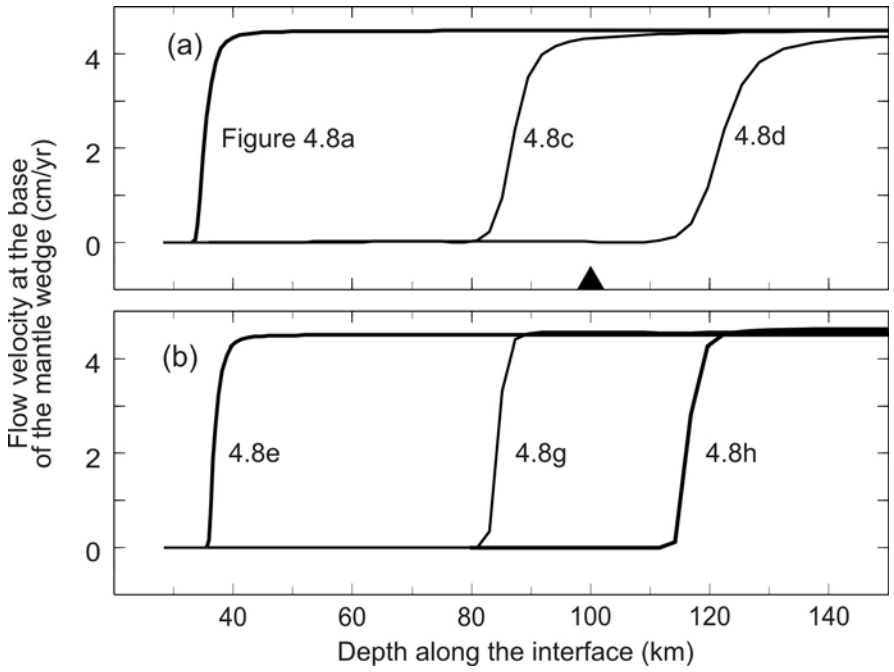

Figure 4.9. Flow velocity at the base of the mantle wedge with a dislocation-creep mantle rheology and an isoviscous interface layer. (a) Warm-slab models shown in **Figure 4.8 a**, **c**, and **d**. (b) Cold-slab models shown in **Figures 4.8 e**, **g**, and **h**.

The bimodal flow behaviour allows some simplifications to be used in modelling practice. For example, the free-slip decoupling zone with a prescribed termination depth used by *Furukawa* [1993] and the "rigid corner" used by *Peacock and Wang* [1999], *van Keken et al.* [2002], and *Currie et al.* [2004a] are reasonable approximations since they all impose a sharp transition from no wedge flow to full-speed flow. Also, since most of the wedge above the zone of decoupling is stagnant, within a broad range, the rheological parameters used for this part of the wedge have little influence. It is the strong sensitivity to temperature and stress that gives rise to the sharp transition between the stagnant and flowing parts of the mantle wedge; the exact parameter values are not critical. This is why even the rigid corner model can be a reasonable approximation.

4.4.4. Dislocation-Creep Mantle Wedge and Dislocation-Creep Interface Layer

To test how the choice of the interface layer rheology may affect slab-mantle decoupling and the mantle flow behaviour, I apply a dislocation-creep rheology to the interface layer in this section. Since antigorite is expected to be abundant at the base of a hydrated mantle wedge, I use the rheological parameter values determined for antigorite (**Table 3.1**). Recent laboratory results show that during dislocation creep, antigorite is significantly weaker than wet olivine at shallow depths, but the decrease in their strength with depth due to increasing temperature is more prominent for wet olivine than for antigorite, resulting in a decrease in the strength contrast between them as shown in **Figure 2.2** [*Hilairet et al.*, 2007]. The application of the dislocation-creep rheology of antigorite to the interface layer, thus, corresponds to the scenario in **Figure 3.6e**, and the

MDD is regulated by the eventual disappearance of the strength contrast between antigorite and wet olivine.

Because the strength of the interface layer is prescribed to be that of antigorite, I vary the degree of decoupling by varying the thickness of the interface layer instead. With an 8-Ma old slab, a 100-m and 500-m thick interface layer results in MDD of ~75 km and ~120 km depths, respectively (**Figure 4.10**). The resultant flow is also bimodal, but the bimodal behaviour is even more pronounced, and the transition from the decoupled to coupled part of the interface even sharper (**Figure 4.11**), than the models with a dislocation-creep mantle wedge and an isoviscous interface layer (**Figure 4.9**). The sharpness of transition is caused by the nonlinear behaviour of the layer strength in addition to that of the mantle wedge, making the model highly nonlinear.

The results presented in **Sections 4.4.1**, **4.4.2**, **4.4.3**, and this section illustrate how the nonlinearity of the flow system affects the slab-mantle decoupling and mantle wedge

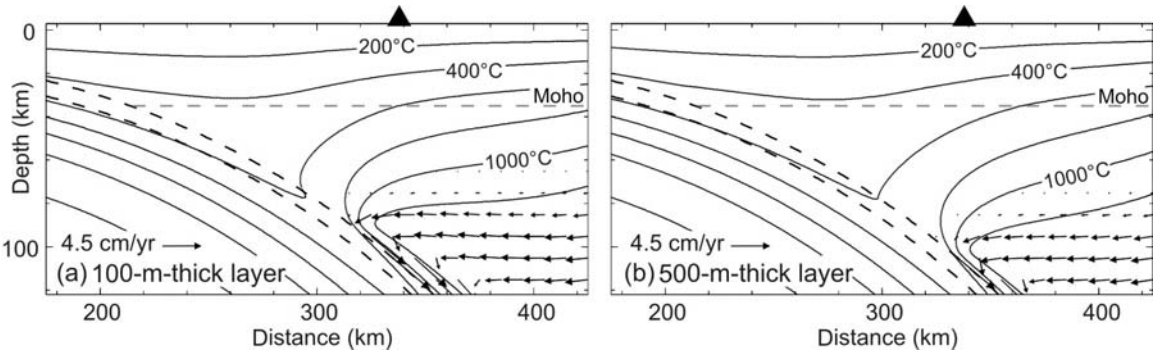

Figure 4.10. Temperature and flow velocities (arrows) in warm-slab (8 Ma) models with a dislocation-creep mantle wedge and a dislocation-creep interface layer that extends along the entire length of the slab. (a) 100-m-thick interface layer. (b) 500-m-thick interface layer. With a 130-Ma slab and a layer thickness of 100 m or greater, the interface is decoupled to a much greater depth (> 200 km depth) beyond the model dimension (results not shown).

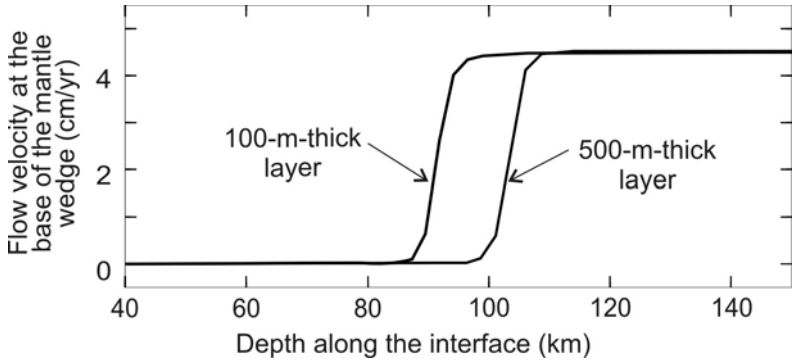

Figure 4.11. Flow velocity at the base of the mantle wedge in models with a dislocation-creep mantle wedge and a dislocation-creep interface layer.

flow pattern. The temperature-dependence of the mantle rheology causes the mantle wedge flow to be bimodal due to nonlinear feedback between temperature and the strength of the mantle (**Figures 4.6** and **4.7**), in strong contrast with the evenly distributed flow pattern in an isoviscous mantle wedge (**Figures 4.4** and **4.5**). The bimodal flow behaviour is more pronounced in a dislocation-creep mantle wedge due to the stress- as well as temperature-dependence of the mantle rheology, leading to a sharp decoupling-coupling transition (**Figures 4.8** and **4.9**). If the mantle wedge and interface layer both have a dislocation-creep rheology, the decoupling-coupling transition is even sharper because of the greater nonlinearity of the flow system (**Figures 4.10** and **4.11**). In nature, there are likely to be many other factors that may increase the nonlinearity of the system such as metamorphic phase changes and melting, and the bimodal flow behaviour and the sharp decoupling-coupling transition may be even more pronounced than portrayed by these modelling results.

4.4.5. Maximum Depth of Decoupling and Mantle Wedge Thermal Structure

The surface heat flow patterns predicted by the models with a dislocation-creep mantle rheology and isoviscous interface layer (**Figure 4.8a-d**) are compared with observations from northern Cascadia in **Figure 4.12**. The offshore heat flow data were obtained from the northern part of the model corridor where the subducting slab is younger (6 Ma) and the slab dips slightly more steeply in the forearc region than in the model which is intended to represent a northern Cascadia average. For all the four warm-slab models in **Figure 4.8**, the predicted surface heat flow seaward of the trench is slightly lower than the observed because of the older slab (8 Ma) in the model. The higher predicted values compared to the data from the trench to ~175 km landward are

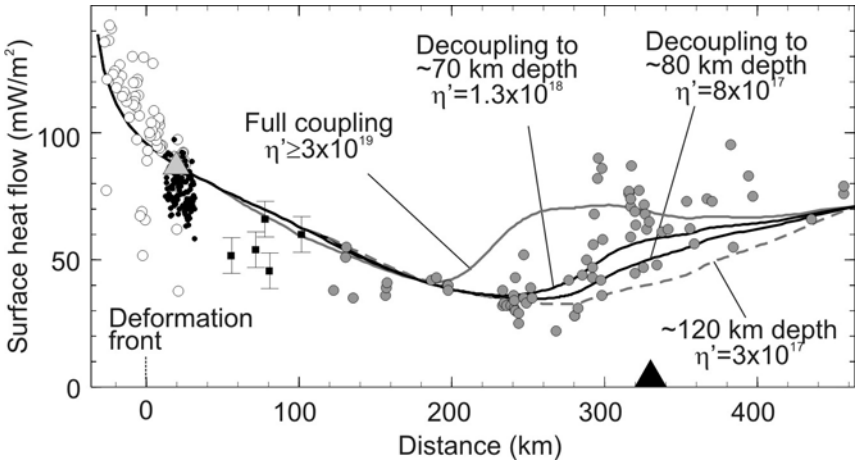

Figure 4.12. Surface heat flow for the warm slab models shown in **Figure 4.8** compared with observations at northern Cascadia. See the caption of **Figure 4.1b** for different symbols used for surface heat flow measurements. The scattered very high values near the volcanic arc are affected by local near-surface processes and do not represent background heat flow. Each model is labeled with the interface layer viscosity (Pa s) as in **Figure 4.8**.

caused by the shallower slab dip used in the model. These differences affect the shallow part of the subduction zone but have little effect on the mantle wedge thermal structure.

The sharp downdip transition from decoupling to coupling has a dramatic effect on the thermal regime of the mantle wedge. The decoupled stagnant part of the mantle wedge is cold because of conductive cooling caused by the descending slab, resulting in low surface heat flow. The deeper coupled part of the mantle wedge is hot because the wedge flow brings in heat from greater depths and the backarc, resulting in high surface heat flow. The thermal contrast between the cold and the hot part of the mantle wedge is sharp, and the transition from low to high surface heat flow values is governed by the maximum depth of decoupling (MDD) as discussed in **Section 4.3**.

The location of the initial heat flow rise predicted by the model with decoupling to ~70 or ~80 km (**Figure 4.8b** or **c**, respectively) is generally consistent with that of the observed pattern (**Figure 4.12**). Stronger coupling induces flow near the wedge tip, causes high temperature in the forearc mantle wedge, and therefore causes the heat flow rise to occur at a shorter distance from the trench (e.g., **Figure 4.8a**). The model with decoupling to ~120 km (**Figure 4.8d**) yields a heat flow pattern marginally consistent with observations, but the predicted temperature beneath the volcanic arc is too low (~500°C) for melt generation (See discussion in **Section 4.3**).

Because both models in **Figures 4.8b** and **c** give a reasonable fit to heat flow observations, the choice between the two has to be based on their predicted mantle wedge temperature below the volcanic arc. For example, if the temperature is required to be greater than 1250°C, one may argue that the model in **Figure 4.8b** is a better choice. However, given the present large uncertainties in the interpretation of geochemical data

to infer arc-mantle temperatures [*Kelemen et al.*, 2003], both models are equally acceptable. Thus, the model shown in either **Figure 4.8b** or **c** can be considered the preferred model for northern Cascadia.

Because the mantle wedge should be cold in the forearc and yet be sufficiently hot for melt generation beneath the volcanic arc, the models with decoupling to about 70-80 km depths, as shown in **Figure 4.8b, c, f,** and **g**, are considered representative of most subduction zones, an issue I will further explore in **Chapter 5**. Decoupling depths of 70-80 km have been used in thermal models of several different subduction zones constrained by heat flow and/or other geophysical observations [e.g., *Furukawa*, 1993; *Peacock and Wang*, 1999; *van Keken et al*., 2002; *Currie et al*., 2004a; *Kneller et al*., 2005; *Abers et al*., 2006].

4.4.6. Discussion About Stress Along the Interface

To understand the nature of the coupling and decoupling as portrayed in the models, it is necessary to examine the distribution of shear stress along the interface (**Figure 4.14**). For the examples shown in **Figure 4.13**, the linear increase in the shallowest part results from Coulomb friction used to calculate Q_{FH}, as explained in **Section 3.2.2**. What is the most relevant for this study is the stress along the slab-mantle wedge contact which is determined by the viscosity and shear strain rate of the thin layer along the interface.

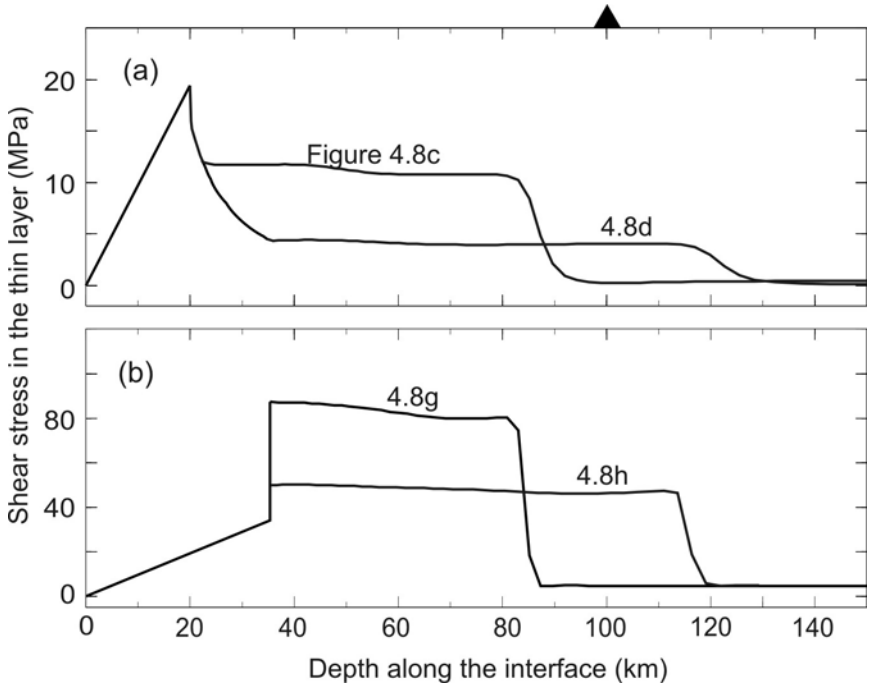

Figure 4.13. Shear stresses in the isoviscous interface layer. Approximate location of the volcanic arc is indicated using a solid triangle. (a) Warm-slab models shown in **Figure 4.8c** and **d**. (b) Cold-slab models shown in **Figure 4.8g** and **h**.

The stress distribution may appear counterintuitive in that the decoupled part of the interface has a higher stress than the fully coupled part further downdip. For example, in the preferred Cascadia model (**Figure 4.13a**), the stress along the decoupled part of the interface from 35 km to 80 km depths is about 12 MPa but sharply decreases to about 1 MPa along the coupled deeper part. This is the best demonstration that coupling and decoupling is controlled by the strength contrast between the interface and the mantle wedge, not by the absolute strength of the interface alone. Across the downdip transition from decoupling to coupling, the stress along the interface decreases by about one order of magnitude, but the viscous strength of the overlying mantle wedge decreases by several orders of magnitude because of the temperature- and stress-dependent rheology.

In the warmer (roughly > 800°C) part of the mantle wedge, the effective viscosity is so low that the shear stress is everywhere less than 1 MPa (results not shown), as is also shown in the models of *Kneller et al*. [2005]. Beneath the volcanic arc, the presence of melts is expected to further weaken the mantle wedge material.

Some limit on the level of shear stress along the slab-mantle wedge interface can be placed on the basis of the state of stress in the upper plate. In the Cascadia forearc, earthquake focal mechanisms and other stress indicators suggest a lack of a strong margin-normal compression [*Wang and He*, 1999] (Also see **Section 2.4.3**). If all the margin-normal compression is caused by frictional coupling along the shallowest part of the Cascadia megathrust (the seismogenic portion), an effective coefficient of fault friction μ' less than 0.08 can explain the observed degree of compression [*Wang and He*, 1999]. In NE Japan, where a cold slab is being subducted, there is strong margin-normal compression, but even this compression can be explained using a weak subduction fault that extends to 50 km depth, consistent with the observed depth extent of the seismogenic zone [*Wang and Suyehiro*, 1999]. In NE Japan, large shear stress further downdip is not required, although it cannot be excluded. The horizontal component of the shear stress along the base of the stagnant mantle wedge that exerts margin-normal compression on the upper plate is about 87% of what is shown in **Figure 4.1e**, given the dip of the interface. This, combined with the shear stress along the updip seismogenic portion, would give a margin-normal compression somewhat higher than required by forearc stress observations, especially for the Cascadia case.

It can be argued that the values shown in **Figure 4.1e** are upper limits, and the actual values in real subduction zones are very likely to be much lower. I have tried to

perturb the preferred models of **Figure 4.8b, c, f** and **g** by increasing or decreasing the strength (i.e., thin-layer viscosity) of the decoupled part of the interface while keeping the rest of the interface unchanged. If the decoupled interface is any stronger, that is, if the interface stress is higher than shown in **Figure 4.13**, decoupling will be terminated at a shallower depth. However, if the decoupled interface becomes a few times as weak, the depth of decoupling is not significantly affected. In a real subduction zone, the decoupled part of the interface is expected to have a tendency for further weakening because of continuing fluid supply from the slab and the increasing degree of hydration of the base of the stagnant mantle wedge. Therefore, the stress along the decoupled interface is also expected to be lower than shown in **Figure 4.13**.

It is worth mentioning the role of shear heating along the interface in limiting the stress. I have also tested models without including viscous shear heating (results not shown). In those models, the η_e values immediately above the slab are much higher due to lower temperatures along the interface. As a result, the viscosities of the interface layer required to produce flow and temperature patterns nearly identical to those shown in **Figure 4.8** are orders of magnitude higher, and the shear stresses along the interface are unacceptably high.

4.5. Summary

Using a two-dimensional steady state thermal model for northern Cascadia and the interface layer approach, I have numerically investigated the effect of interface decoupling on mantle wedge flow and subduction zone thermal regime. Models with an

isoviscous mantle wedge and a truncated isoviscous interface layer illustrate how the slab-mantle coupling is controlled by the strength contrast between the interface layer and the overriding mantle. The slab and the mantle are fully coupled if the layer viscosity is equal to or greater than the viscosity of the overriding mantle. A layer viscosity smaller than the mantle viscosity results in interface weakening, and flow velocity along the base of the mantle wedge over the weak interface layer decreases with decreasing layer viscosity.

In models with a more realistic diffusion- or dislocation-creep mantle rheology and an isoviscous interface layer that extends along the entire slab length, the strength of the mantle wedge decreases with increasing depth due to its strong sensitivity to temperature, and the strength contrast between the mantle and an isoviscous interface layer disappears at depth, resulting in coupling. Models of this type show a bimodal flow behaviour in the forearc mantle wedge: the base of the mantle wedge either almost does not flow at all or flows at the slab velocity. This is because of the nonlinear feedback between temperature and the mantle strength. However, in the dislocation-creep mantle wedge, its stress-dependence results in an additional feedback effect on the mantle strength, making the bimodal behaviour more pronounced than in the diffusion-creep mantle wedge. This highly nonlinear flow behaviour leads to a sharp transition from the decoupled to coupled interface. The decoupling-coupling transition is even sharper when a dislocation-creep rheology is used for both the mantle wedge and interface layer, and the sharpness of the transition increases with increasing nonlinearity of the flow system.

Because of the bimodal flow behaviour, the spatial transition between the thermal states of the seaward stagnant part and the landward, deeper flowing part of the mantle

wedge is rather abrupt. The cold stagnant part gives low heat flow at the surface; the hot flowing part gives high heat flow and maintains the high mantle temperature required for arc magmatism. Models with interface decoupling to a depth of about 70-80 km best explain the observed change in surface heat flow pattern from landward decrease to landward increase in the forearc of northern Cascadia while satisfying the petrological expectation for the thermal condition beneath the volcanic arc.

Decoupling is a reflection of the strength contrast between the interface and the mantle wedge. The downdip transition from decoupling to coupling may be accompanied with a stress increase along the interface. However, on the contrary, if the strength of the interface is assumed to be uniform, the stress along the coupled deeper part of the interface is an order of magnitude lower than the decoupled shallower part. This is because of the extreme sensitivity of the mantle strength to temperature. The level of stress along the decoupled interface in the preferred northern Cascadia models should be considered to represent an upper limit.

Chapter 5

Common Maximum Depth of Slab-Mantle Decoupling: Reconciling Diversity and Uniformity of Subduction Zones

5.1. Introduction

The review of available observations compiled from seventeen subduction zones (**Figure 2.1**) in **Chapter 2** illustrates two contrasting characteristics of subduction zones. On the one hand, the distribution and activity level of many geophysical processes in subduction zones vary systematically with the thermal state of the slab, giving rise to a rich diversity. On the other hand, the configuration of subduction zones is rather uniform in that the volcanic arc is typically situated where the slab is around 100 km deep. Some of the main observations presented in **Chapter 2** are summarized in **Figure 5.1**.

Great progress has been made in understanding the diversity of subduction zones. Major differences between subduction zones can be explained by differences in thermally controlled petrologic processes in the subducting slab [e.g. *Kirby et al.*, 1996a; *Peacock and Wang*, 1999; *Hacker et al*., 2003a] as discussed in **Chapter 2**. Slabs of different ages and hence thermal states go through different PT paths during subduction, and it is now widely accepted that the different dehydration depths and different abundance of fluids from the dehydrating slab give rise to the differences in such processes as intraslab earthquakes and arc volcanism.

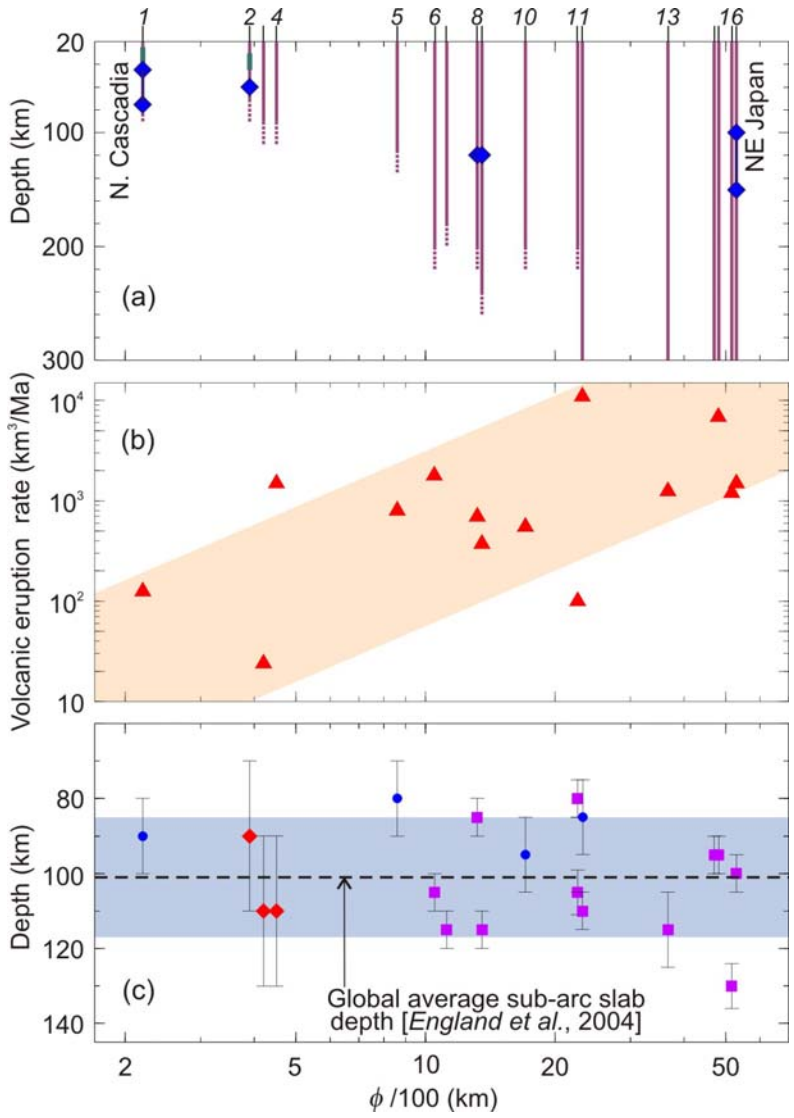

Figure 5.1. Summary diagram of variations of the observed characteristic parameters of geophysical processes in subduction zones with the thermal parameter ϕ as presented in **Chapter 2**. Index numbers for the seventeen subduction zones (**Figure 2.1**, **Table 2.1**) are shown at the top. (a) Observed maximum depth of a low-velocity layer in the subducting crust (blue diamond) and depth range of intraslab seismicity (purple lines). Dashed purple lines indicate uncertainties in the maximum depth. Green lines indicate the depth range of ETS events in northern Cascadia [*Kao et al.*, 2005] and Nankai [*Shelly et al.*, 2006]. (b) Long-term volcanic output rates of volcanic arc [*Crisp*, 1984; *White et al.*, 2006]. (c) Sub-arc slab depths *H* determined by *England et al.* [2004] (purple squares) and others (blue circles) and those estimated in the present study (red circles) with error bars. All the parameter values and their references except for the depth range of ETS are listed in **Table 2.2**.

Less progress has been made in understanding the uniformity of subduction zone configuration. Significant effort was previously made to explain the relatively uniform sub-arc slab depth *H*, primarily by flux melting triggered by pressure-dependent dehydration reactions in the subducting slab, but what causes the uniform *H* is still an unresolved outstanding issue as discussed in **Section 2.5.3**, and why the configuration of subduction zones are so uniform among subduction zones that are often vastly different in other aspects is yet to be addressed.

Building on the concepts discussed in **Chapter 4**, I develop thermal and petrological models for all the seventeen subduction zones (**Figure 2.1**) in order to explain the observed diversity and uniformity. The main challenge is to reconcile the diversity that is strongly dependent on the thermal state of the subducting slab and the uniformity that is independent of the thermal state of the slab. I will demonstrate that thermal models featuring a sharp contrast between a cold forearc and a hot volcanic arc such as those shown in **Figure 4.8b** and **c** have these seemingly self-contradicting characteristics. The key parameter that controls this sharp contrast is the maximum depth of decoupling (MDD) between the subducting slab and the overriding mantle wedge as discussed in **Section 4.4.5**. In most of the forearc where the slab and the mantle wedge are decoupled, the thermal regime is strongly controlled by the thermal state of the slab. Beneath the arc where the slab and mantle wedge are coupled, the thermal regime is controlled mainly by mantle wedge flow and is nearly independent of the thermal state of the slab. I will show that a common MDD of 70-80 km can reconcile the observed diversity and uniformity of subduction zones. The modelling results presented in this chapter have been summarized in a manuscript by *Wada and Wang* [2009, in press].

5.2. Hypothesis of a Common Maximum Depth of Slab-Mantle Decoupling

Let us first reemphasize the observationally inferred strong thermal contrast between the cold forearc and hot arc-backarc in subduction zones. Surface heat flow and other geophysical and geological observations indicate a cold forearc mantle (< 700°C) (**Section 2.2.1**) while petrological, geochemical and thermobarometric data indicate a hot sub-arc mantle (> 1200°C) (**Section 2.5.1**). The thermal contrast between the forearc mantle and sub-arc mantle is large, and the spatial transition between the two thermal regimes is sharp.

The two most important factors that govern the thermal regime of subduction zones are the thermal state of the subducting plate and the mantle wedge flow. As discussed in **Chapter 2**, the thermal state of the subducting slab obviously has a first-order impact on the thermal regime as evidenced by its strong influence on various processes (**Figure 5.1a** and **b**). However, the thermal effect of the slab cannot be dominant in the region of the volcanic arc as evidenced by its lack of influence on the location of the arc (**Figure 5.1c**). It can be reasoned that this is because the thermal effect of the slab is overshadowed by that of the mantle wedge flow in the arc region.

Modelling results presented in **Section 4.4.3** have illustrated that the sharp thermal contrast between the cold forearc and hot arc is due to the sudden onset of mantle wedge flow near the arc, that is, the downdip termination of slab-mantle decoupling. Over the decoupled interface in most of the forearc, there is no mantle wedge flow, and the thermal regime is controlled mainly by the relatively cold subducting slab. Farther downdip, an abrupt increase in the slab-mantle coupling causes a sudden onset of mantle wedge flow and hence the sharp transition from the cold forearc mantle to the hot sub-arc

mantle. Therefore, the key parameter to investigate is the maximum depth of slab-mantle decoupling (the MDD). To explain the uniform configuration of subduction zones, we hypothesize that most, if not all, subduction zones share a common MDD. In the following, this hypothesis will be tested using numerical thermal models.

5.3. Thermal Model Setup for Seventeen Subduction Zones

The numerical method and modelling approach used in this chapter are exactly the same as in **Section 4.4.3** except that the thin weak interface layer is terminated at a prescribed depth (**Figure 5.2**). As was shown in **Section 4.3.3**, the nonlinear feedback between temperature and the effective viscosity of the mantle always leads to nearly complete stagnation of the mantle wedge above a weakened interface and that the downdip transition from decoupling to coupling is always sharp. A slight reduction in flow velocity due to a weakened interface leads to lower temperatures, and the lower temperature in turn causes a higher effective viscosity, leading to an increase in the strength contrast between the mantle wedge and the interface and further decoupling. This nonlinear feedback between temperature and the mantle strength results in the sharp transition from the decoupled to coupled part of the interface as if the zone of decoupling is abruptly truncated. In this chapter, I truncate the weak interface layer at a prescribed MDD for numerical convenience. In this case, the exact value of the viscosity of the interface layer is unimportant as long as it is low enough to cause decoupling. I use the layer viscosity of 10^{17} Pa s in this study. The MDD itself will be the only variable parameter to be tested.

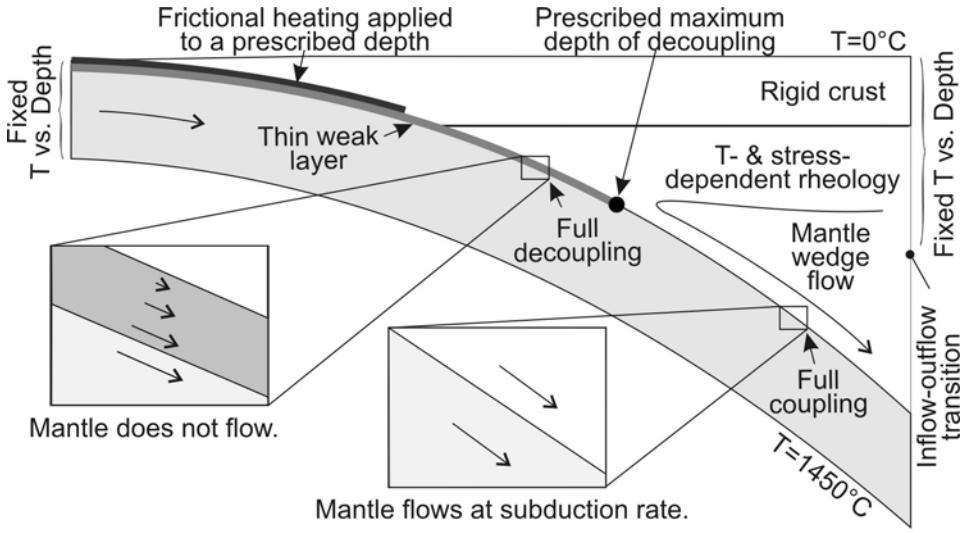

Figure 5.2. Schematic illustration of boundary and interface conditions for the thermal models developed in this chapter. The interface condition is simplified from that used in **Chapter 4** (**Figure 3.2**) by truncating the interface layer at a prescribed depth.

The northern Cascadia model presented in **Section 4.4.3** was developed using the interface layer extending along the entire length of the subducting slab. In this section, I develop a model for northern Cascadia with the simplified approach described above to be consistent with the models for the other sixteen subduction zones. The northern Cascadia model presented in this chapter also differs from that in **Section 4.4.3** in that the effect of sedimentation on the thermal state of the incoming plate is included as will be discussed in **Section 5.5.3**.

For each of the seventeen subduction zones shown in **Figure 2.1**, a model is developed along a representative corridor oriented roughly in the margin-normal direction. Details of how the slab geometry was obtained for individual subduction zones will be provided together with the modeling results in **Sections 5.5.4** and **5.5.5**. References for the slab geometry and model parameterization for all the seventeen

subduction zones are summarized in **Table 5.1**. The dimensions of elements in these models typically range from ~10 m to ~15 km.

In the thermal model, there is no practical need to differentiate between the subducting crust and mantle. However, in the determination of the metamorphic boundaries in the subducting slab from the thermal modelling results, the subducting crust and mantle need to be differentiated. I assume that the subducting crust has the global average oceanic crustal thickness of 7 km, except for northern Hikurangi where the 17-km thick oceanic Hikurangi Plateau is being subducted [*Davy and Wood*, 1994; *Mortimer and Parkinson*, 1996].

In the model, the thickness of the non-deforming overriding plate from the surface to the Moho depth has little effects on mantle wedge flow as explained in **Section 3.4**. However, the Moho depth at continental margins is relevant to converting depth to pressure when the thermal modelling results are used to determine the metamorphic state of the subducting slab and mantle wedge. Therefore, in the models for the thirteen continental margins studied here, I assign the thickness of the overriding crust in each model in accordance with the Moho depth reported in published seismological studies (**Table 5.1**). I use a conventional approach of using lithostatic pressure in the determination of the depth of phase transformation. Errors due to neglecting dynamic pressure associated with viscous flow in our petrological model are expected to be much smaller than uncertainties in the metamorphic phase boundaries. The Moho depth of the overriding plate at these margins is mostly in the range of 30-40 km except in northern Chile where it is reported to be in the range of 50-70 km in the forearc region [*Yuan et al.*, 2000; *Koulakov et al.*, 2006]. I thus assume a 60-km-thick crust for the northern Chile

Table 5.1. Summary of model parameterization

Index	Subduction zone	Intersection of model profile and trench		Profile direction[a]	References for slab geometry model[b]	Trench depth (km)	Sediment thickness (km) and references		Crustal thickness (km)	Downdip end of frictional heating (km)	Backarc heat flow (mW/m^3)
		Long (°)	Lat (°)	(°)							
1	N. Cascadia	-126.3	47.8	62	*McCrory et al.* [2004]	2	3	*Davis and Hyndman* [1989]	35	15	75[c]
2	Nankai	134.5	32.2	331	*Wang et al.* [2004], *Shiomi et al.* [2004]	4	2	*Clift and Vannucchi* [2004]	35	25	69[c]
3	Mexico	-103.3	17.55	30	*Currie et al.* [2002]	5			40	30	72[c]
4	Colombia-Ecuador	-79.8	2.4	125	*Marcaillou et al.* [2006, 2008], *Engdahl et al.* [1998]	3	4	*Marcaillou et al.* [2006, 2008]	40	30	80[d]
5	SC Chile	-74.7	-38.1	106	*Groß et al.* [2008], *Syracuse and Abers* [2006], *Engdahl et al.* [1998]	5	2	*Groß et al.* [2008]	40	40	80[d]
6	Kyushu	132.5	30.8	296	*Wang et al* [2004], *Baba et al.* [2002], *Goto et al.* [2001]	4	2	*Clift and Vannucchi* [2004]	30	30	69[c]
7	N. Sumatra	97.1	-0.5	54	*Engdahl et al.* [1998], *England et al.* [2004]	5	2.5	*Clift and Vannucchi* [2004]	30	30	120[e]
8	Alaska	-148.2	57.3	309	*Oleskevich et al.* [1999]	4	2.5	*Clift and Vannucchi* [2004]	40	40	80[d]
9	N. Chile	-71.3	-23.5	90	*Sallarès and Ranero* [2005], *Engdahl et al.* [1998], *England et al.* [2004]	8			60	35	85[c]
10	N. Costa Rica	-86.3	9.7	42	*Peacock et al.* [2005], *Syracuse and Abers* [2006]	5			30	30	80[d]
11	Aleutians	-179.7	50.2	0	*Engdahl et al.* [1998], *England et al.* [2004]	5	1.5	*Clift and Vannucchi* [2004]	10	20	75[c]
12	N. Hikurangi	179.2	-40.0	310	*Reyners et al.* [2006]	2.7			30	10	80[d]
13	Mariana	147.9	17.9	270	*Engdahl et al.* [1998], *England et al.* [2004]	8			10	20	80[d]
14	Kermadec	-176.2	-29.3	289	*Engdahl et al.* [1998], *England et al.* [2004]	7.5			10	20	80[d]
15	Kamchatka	161.3	51.7	300	*Engdahl et al.* [1998], *England et al.* [2004]	8			30	40	70[c]
16	Izu	142.3	31.4	263	*Engdahl et al.* [1998], *England et al.* [2004]	10			10	20	80[d]
17	NE Japan	143.3	36.8	293	*Hasegawa et al.* [1994], *Nakajima et al.* [2001], *Takahashi et al.* [2007], *Zhao et al.* [1994]	8			30	40	88[c]

[a] The profile direction is measured from north.
[b] Slab geometry at > 60 km depths in Nankai and at > 90 km depths in Colombia-Ecuador is extrapolated from the slab geometry model for the shallow part of the slab.
[c] The value is the regional average backarc surface heat flow value of the corresponding subduction zone [*Currie and Hyndman*, 2006].
[d] The value is the global average backarc surface heat flow [*Currie and Hyndman*, 2006].
[e] The value is the regional average backarc surface heat flow value obtained from *GHFD.*

model. For the calculation of pressure, I assume a uniform density of 2750 kg/m^3 for the overriding continental crust and 3300 kg/m^3 for the mantle wedge and the subducting slab (**Table 4.1**).

At ocean-ocean margins, the overriding crust consists nearly entirely of mafic material, and thus I assume the same density for the overriding crust as for the mantle wedge. I use the global average oceanic crust thickness of 7 km for the overriding crust for the margins. The thickness of the overriding oceanic crust in the arc-forearc region can vary along strike and in some places can be slightly thicker than 7 km, such as reported by seismic studies in the Izu-Bonin-Mariana margin [e.g. *Kodaira et al.*, 2007]. Therefore, the actual mantle wedge at some ocean-ocean margins may not always extend to depths as shallow as portrayed in some of the models for this type of margins.

For all seventeen subduction zones except northern Cascadia, I use typical values of thermal conductivity and radiogenic heat production rates for the continental crust, subducting crust, and mantle deduced from field measurements and laboratory data (**Table 4.1**). In northern Cascadia, detailed thermal measurements indicate relatively low thermal conductivity and radiogenic heat production rates in the overriding upper crustal material in the forearc region as discussed in **Chapter 4** (**Table 4.1).**

I apply frictional heating and viscous energy dissipation as described in **Section 3.2.2**. The transition from frictional heating to viscous energy dissipation along the interface is prescribed to occur near the depth of the downdip limit of the seismogenic zone as estimated by other studies (**Table 5.1**). The boundary conditions are as described in **Section 3.4**, but the geotherms applied to the vertical boundaries vary between subduction zones and are explained as follows.

To the trench-side vertical boundary, I prescribe a geotherm calculated by using the GDH1 plate cooling model [*Stein and Stein*, 1992] for an appropriate slab age (**Table 2.1**) in most of the models. However, at northern Cascadia, Nankai, Colombia-Ecuador, SC Chile, Kyushu, northern Sumatra, Alaska, and Aleutians, the incoming plate is blanketed by a thick (> 1 km) sediment cover, which increases the temperature of the top part of the plate. I include the thermal effects of sediment deposition and compaction when calculating the oceanic plate geotherm for these margins by using a time-dependent 1-D finite-element code of *Wang and Davis* [1992]. I assume conservative sedimentation rates of ~1 mm/yr and let the sediment accumulate to the present thickness (**Table 5.1**) at the trench. The thermal models do not feature sediment subduction because its thermal effect is negligibly small. The thermal effects of hydrothermal circulation in the top 1-2 km of the incoming oceanic crust are limited within ~20 km distance arc-ward of the trench [*Harris and Wang,* 2002]. Hydrothermal circulation in the crust may continue after subduction, but its cooling effect at depth is small (<50°C) unless vigorous hydrothermal circulation continues to a great depth (>15 km) [*Spinelli and Wang,* 2008]. Therefore, I neglect the effects of hydrothermal circulation in the subduction crust in the models.

At many subduction zones, isochrons on the incoming plate are sub-parallel to the trench, and the age of the plate at the trench is relatively constant with time as assumed in the steady-state models developed in this study. However, at subduction zones with nearly margin-normal isochrons, the incoming plate at the trench becomes older and thus cooler with time. The effect of neglecting this time-dependence of the thermal state of the incoming plate in the steady-state models is insignificant for old slabs. However, for young slabs such as in Nankai and Colombia-Ecuador where the isochrons are nearly

margin-normal, the models of constant slab age determined by using the isochron presently at the trench predict a thermal state slightly colder than actual.

For the shallow part of the backarc-side vertical boundary, I use a conductive heat equation (**Equation 3.16**) to obtain a geotherm consistent with the backarc surface heat flow values reported by *Currie and Hyndman* [2006] for northern Cascadia, Nankai, Kyushu, Mexico, Alaska, Aleutians, Kamchatka and NE Japan (**Table 5.1**). For northern Sumatra, a continental geotherm is used to fit the dense backarc heat flow data in *GHFD*, which indicate unusually high heat flow of ~120 mW/m^2. This high heat flow may indicate high crustal radiogenic heat production or hydrothermal processes in the region [*Hippchen and Hyndman*, 2008], but their effects are not included in the northern Sumatra model since the focus of the present study is on the forearc-arc region. For the other margins, where there is no direct observational constraint, I apply the global average backarc heat flow of 80 mW/m^2 as concluded by *Currie and Hyndman* [2006]. For the deeper part of the backarc-side boundary, I assign a geotherm calculated by using an adiabatic gradient of 0.3°C/km and a mantle potential temperature of 1295°C [*Ito and Katsura*, 1989] as explained in **Section 3.4**. The location of this boundary has a small effect on the temperatures of mantle material flowing into the model domain, and a horizontal shift by ~50 km causes up to ~20°C difference in the sub-arc mantle temperature. For consistency, I place the boundary at 150-km horizontal distance from the point of MDD in all models. For given heat supply from the backarc and mantle rheology, mantle temperature in the forearc-arc region depends primarily on the mantle wedge flow pattern, which is controlled by the MDD and the kinematics of the slab (subduction rate and slab dip) as will be shown in **Sections 5.4** and **5.5**.

5.4. End-member Warm-slab and Cold-slab Subduction Zones: Northern Cascadia and NE Japan

Let us compare models for two subduction zones that have extensive heat flow constraints, northern Cascadia and NE Japan (**Figures 5.3** and **5.4**, respectively). Northern Cascadia and NE Japan represent end-member warm- and cold-slab subduction zones (**Table 2.1**). They show dramatic contrasts in their metamorphic, volcanic, and seismological characteristics (**Figure 5.1a**, **b**), but they share a similar configuration in that the volcanic arc is located where the slab is at around 100 km depth (**Figure 5.1c**). Heat flow measurements near the trench at these two margins reflect the ages of the subducting plates, but in both places, values are low in the rest of the forearc until some 20-50 km sea-ward of the volcanic arc.

The Cascadia model shown in **Figure 5.3** is almost identical to that in **Chapter 4.** For the NE Japan model shown in **Figure 5.4**, I use the slab geometry model that has been constrained by numerous studies using intraslab seismicity, seismic reflection and refraction data, and tomographic images of seismic velocity structures [*Nakajima et al.*, 2001; *Takahashi et al.*, 2007; *Hasegawa et al*., 1994; *Zhao et al.*, 1994].

An MDD of ~75 km can explain the heat flow data at both northern Cascadia and NE Japan (**Figures 5.3** and **5.4**, respectively). The NE Japan results are consistent with the modelling results of previous studies [e.g. *Furukawa*, 1993]. Increasing or decreasing the MDD by 15 km will lead to a poorer fit between the model-predicted and observed surface heat flow patterns, and, in both cases, a deeper MDD (e.g. 90 km) results in a sub-arc mantle wedge temperature that is too low (< 1200°C) for melt generation (results not displayed).

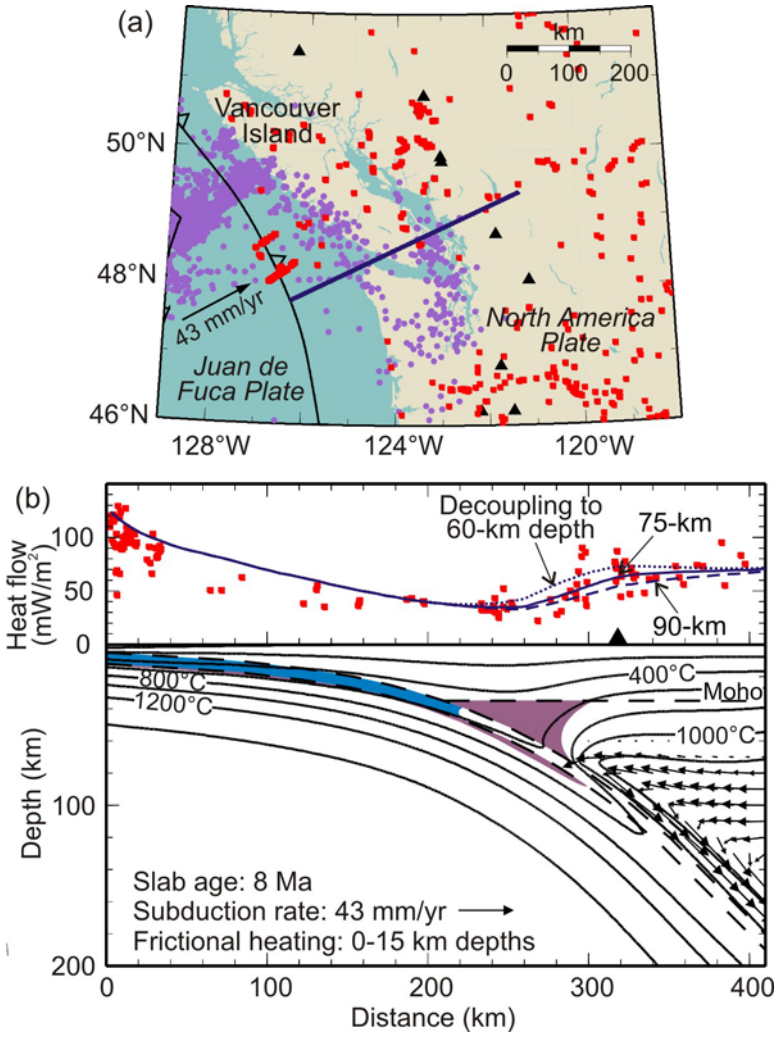

Figure 5.3. (a) Map of northern Cascadia (index number 1), showing the distributions of surface heat flow observations (red squares) and earthquakes in the Juan de Fuca plate (purple dots). The blue thick line indicates the profile line for the northern Cascadia thermal model. (b) Observed (red squares) and model-predicted (blue lines) surface heat flows and model-predicted flow and temperature fields with the 75-km MDD for northern Cascadia. Surface heat flow data [*Wang et al.*, 1995; *Currie et al.*, 2004a] within 100 km of the profile line are plotted in (b) (See **Section 4.3** for the compilation of heat flow data). The scatter of heat flow values near the volcanic arc is caused by local near-surface processes. Arrows in the mantle wedge indicate flow velocities. Blue and white in the subducting crust represent regions of high (0.7-5.4 wt%) and low (≤ 0.7 wt%) H_2O contents, respectively [*Hacker et al.*, 2003b] (**Figure 2.3**). The boundary between them roughly represents the basalt-eclogite transforma-

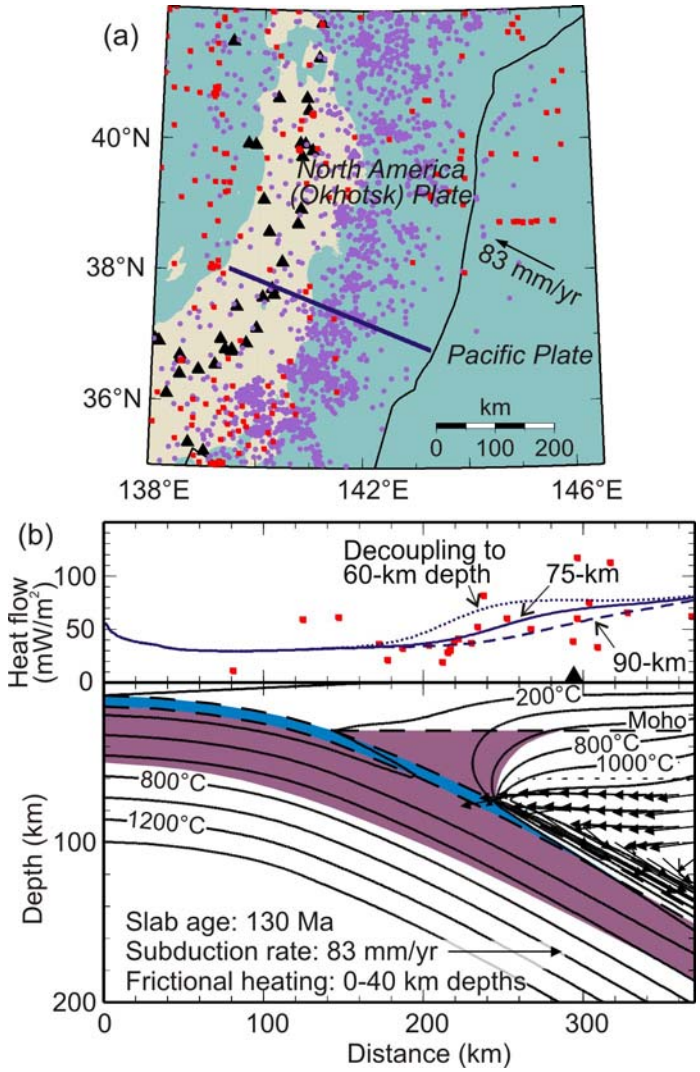

Figure 5.4. (a) Map and (b) modelling results with 75-km maximum depth of decoupling for NE Japan (index number 17) presented in the same way as **Figure 5.3**. Heat flow observations in and around Japan were compiled by *Tanaka et al.* [2004] and consist of 2450 values from *Yamano* [1995] and 734 new values. The heat flow measurements within 200 km of the profile line are plotted in (b).

(**Figure 5.3 caption continued**)

tion under thermodynamic equilibrium, which releases a large amount of H_2O. The transformation may be kinetically delayed in the lower subducting crust. Purple in the mantle wedge and slab mantle indicates zones of antigorite stability [*Schmidt and Poli*, 1998] (**Figure 2.5**).

Using the calculated thermal field and the pressure converted from depth, I outline in **Figures 5.3b** and **5.4b** the basalt-eclogite transformation in the subducting crust and the zones of antigorite stability in the mantle wedge and the subducting mantle. The depths of basalt-eclogite transformation are based on phase boundaries of H_2O-saturated basalt shown in **Figure 2.3**. The zones of antigorite stability in the mantle wedge and the subducting mantle are based on phase boundaries for wet peridotite shown in **Figure 2.5**. The illustrated zones of antigorite stability in the mantle wedge and subducting mantle only represent the maximum possible spatial extent of antigorite and do not mean that antigorite must be present everywhere in these zones. How much antigorite is actually present depends on how much fluid is available. For example, as discussed in **Section 2.3.3**, antigorite, as well as other hydrous minerals found in a hydrated mantle wedge, is expected to be most abundant along the base of the mantle wedge. Serpentinization of the subducting plate occurs prior to subduction and depends on how much and how far H_2O can penetrate into the oceanic mantle.

The model-predicted depths of basalt-eclogite transformation, that is, the peak crustal dehydration in the subducting crust, are 40-47 km in the young slab in Cascadia but 75-140 km in the old slab in NE Japan. The greater depth for NE Japan is due to the cooler thermal state of the slab, and the larger depth range is due to the steep Clapeyron slope (dP/dT) of the basalt-eclogite transformation over the temperature range of the subducting crust (**Figure 2.3**) [*Hacker et al.*, 2003b]. The predicted depths of the basalt-eclogite transformation are consistent with the downdip extent of an LVL at 45-75 km depths reported for northern Cascadia and 100-150 km depths for NE Japan (**Section 2.3.1; Figure 5.1a**). The slightly deeper extent of the observed LVL may indicate

kinetically delayed transformation of the anhydrous gabbroic lower crust [*Hacker et al.*, 2003a]. The model-predicted zone of antigorite stability in the subducting mantle extends to 90 km depth in Cascadia and ~290 km depth in NE Japan (**Table 5.2**). The large difference is consistent with the observed difference in the depth ranges of intermediate-depth intraslab seismicity between these two subduction zones (**Figure 5.1a**) and supports the hypothesis that the dehydration of antigorite triggers embrittlement and intraslab seismicity in the subducting mantle as proposed by other workers [e.g. *Seno and Yamanaka*, 1996; *Peacock*, 2001; *Brudzinski et al.*, 2007]. During this dissertation research, I developed a detailed thermal model for northern Washington to investigate the thermal environment of the M_w 6.8 Nisqually earthquake that occurred in Washington in 2001 [*Kao et al.*, 2008]. The modeling results also support the dehydration embrittlement hypothesis.

The degree of decoupling along the subduction interface controls not only the dehydration of the slab but also the hydration of the mantle wedge. For the similar MDD, the models for both subduction zones have a similar zone of antigorite stability in the mantle wedge despite the large differences in the petrology of the subducting slab. However, the shallow dehydration of the subducting slab in Cascadia should provide ample fluid beneath the cold stagnant part of the forearc mantle wedge to promote mantle wedge serpentinization but little fluid beneath the arc region for melt generation. The situation is the opposite in NE Japan, for which peak slab dehydration is predicted to occur at greater depths beneath the arc region, providing ample fluid for arc volcanism but less fluid for forearc mantle wedge serpentinization. These model predictions are

consistent with the inferred degree of serpentinization and the observed intensity of arc volcanism for the two subduction zones (**Chapter 2**, **Figure 5.1b**).

The models explain not only the differences between the two subduction zones but also their similar subduction zone configuration. In both the Cascadia and NE Japan models, high temperatures (> 1200°C) occur in the mantle wedge where the depth of the slab is about 100 km or greater, providing the necessary thermal condition for melt generation beneath the arc. Because of the slab-mantle decoupling, the forearc region is

Table 5.2. Summary of modelling results.

Index	Subduction zone	Maximum sub-arc mantle temperature (°)	Depths of peak crustal dehydration (top, bottom)[b] (km)	Maximum depth of antigorite stability in the subducting mantle (km)
1	N. Cascadia	1250	40, 46.5	90
2	Nankai	1260	55, 46	115
3	Mexico	1310	68, 75	130
4	Colombia-Ecuador	1305	63, 65	125
5	SC Chile	1220	72, 93	170
6	Kyushu	1290	71.5, 93	185
7	N. Sumatra	1305	72.5, 92	175
8	Alaska	1215	71.5, 93	195
9	N. Chile	1320	73, 103	210[c]
10	N. Costa Rica	1280	73.5, 121.5	215
11	Aleutians	1250	74, 126	240
12	N. Hikurangi	1120 and 1310[a]	73, 139	220
13	Mariana	1250	74, 117	240
14	Kermadec	1240	74, 141.5	275
15	Kamchatka	1290	74, 126	280[c]
16	Izu	1300	74.8, 132	270[c]
17	NE Japan	1310	75, 139.5	290[c]

[a] The two values are the model-predicted maximum mantle temperatures beneath the ocean-side and land-side ends, respectively, of the ~40-km-wide Taupo Volcanic Zone.

[b] "Crustal peak dehydration" occurs at the boundary between the light/dark grey and white regions of the phase diagram shown in **Figure 2.3**. The two values shown in the table are the depths of peak crustal dehydration at the top and bottom of the subducting crust, respectively. See **Section 5.3** for the thickness of the subducting crust.

[c] The downdip end of antigorite stability is extrapolated beyond the model domain from the modelling results.

too cold for melt generation. The thermal models for these two end-member warm- and cold-slab subduction zones indicate that their differences and the intriguing similarity in their subduction zone configuration can be reconciled if the slab-mantle wedge is decoupled to 70-80-km depths.

5.5. Models for the Other Fifteen Subduction Zones

Northern Cascadia and NE Japan have a similar MDD despite their large differences in subduction parameters, supporting the hypothesis that a common MDD can reconcile the uniformity and diversity of subduction zones. To further test this hypothesis more comprehensively, I developed thermal models for the other fifteen subduction zones (**Figure 2.1**; **Table 5.1**) assuming a common MDD of 75 km and using the same modelling strategy as in **Section 5.4**.

All surface heat flow data for the fifteen subduction zones are from *GHFD* unless otherwise stated in the figure caption. For all the fifteen subduction zones, surface heat flow measurements (**Table 2.2**) within 100 km of the profile line are plotted with the model-predicted surface heat flow values except for SC Chile and northern Chile and Kermadec. For SC Chile, I include surface heat flow values derived from the depths of bottom simulating reflectors (BSR) that were imaged at ~120 km south of my profile line [*Grevemeyer et al.*, 2003], and I also include one measurement made at ~110 km north of the profile line [*GHFD*]. For northern Chile and Kermadec, I include measurements within 200 km and 150 km, respectively, of the profile line [*GHFD*]. Limited heat flow observations from these subduction zones provide some model constraints.

5.5.1. Warm Continental Subduction Zones

The modelling results for three continental subduction zones with a warm slab (ϕ < 500 km) are presented in this subsection: Nankai, Colombia, and Mexico (**Table 2.1**). In the Nankai model (**Figure 5.5**), the slab geometry model reported by *Wang et al.* [2004] based primarily on the distribution of intraslab earthquakes is used. Their model, however, is only for the shallow part (< 60 km depth) of the slab due to lack of deeper intraslab earthquakes, and the deeper part of the slab in the thermal model had to be extrapolated from the model of *Wang et al.* [2004]. The observed surface heat flow near the trench is higher than predicted from the age of the plate and very sharply decreases landward. This has been explained to be the consequence of redistribution of heat by hydrothermal circulation in the relatively permeable subducting crust [*Spinelli and Wang*, 2008]. This effect is not important to the regional-scale thermal model shown here.

For the Mexico margin, I developed two models: one for the Michoacan region and

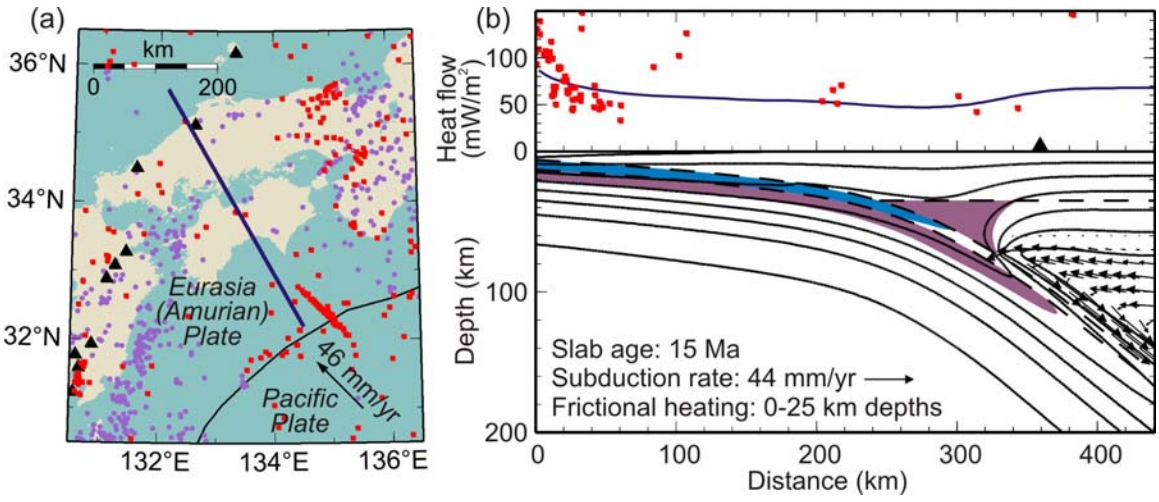

Figure 5.5. Nankai (index number 2). Heat flow data are from *Tanaka et al.* [2004]. See **Figure 5.3** for explanation of symbols and colors.

the other for the Guerrero region (**Figure 5.6a**). In the Michoacan model (**Figure 5.6b**), I use the slab geometry model of *Currie et al.* [2002], which was obtained using earthquake locations determined with the local seismic network. In the Guerrero model (**Figure 5.6c**), I use the slab geometry model of *Manea et al.* [2004, 2005], which was inferred from seismicity and gravity data [*Kostoglodov et al.*, 1996]. The slab is inferred

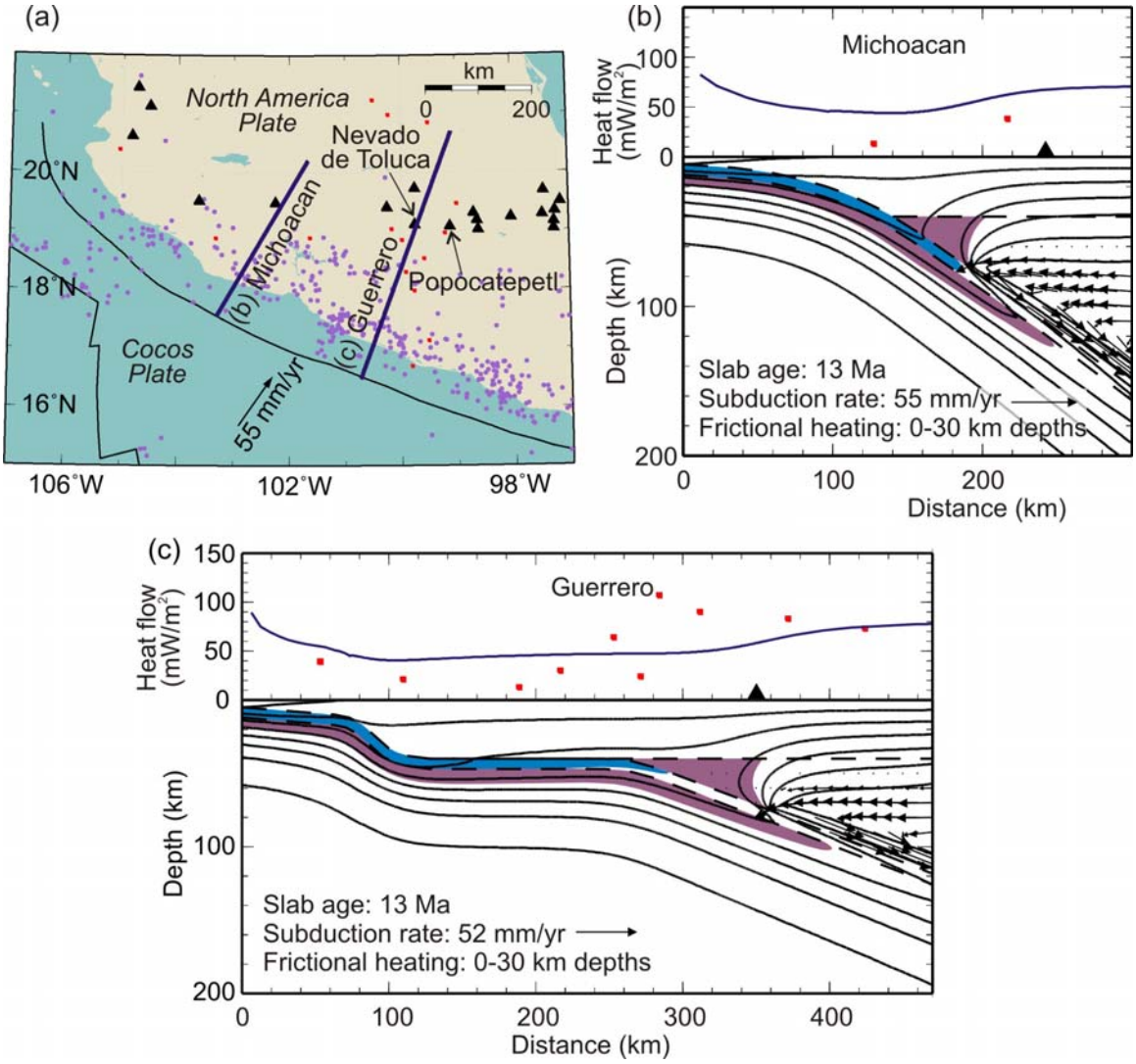

Figure 5.6. Mexico (index number 3). Modeling results for (b) the Michoacan region and (c) the Guerrero region. Heat flow data are from *GHFD*. See **Figure 5.3** for explanation of symbols and colors.

to be sub-horizontal at ~40 km depth over ~150 km distance and lies at unusually shallow depths (~70 km) beneath the arc volcanoes (the Nevado de Toluca and Popocatepetl volcanoes). These new models differ from those of *Currie et al.* [2002] and *Manea et al*. [2004] in that a temperature- and stress-dependent mantle rheology instead of an isoviscous mantle rheology is used.

In the Guerrero region, arc volcanoes are not parallel with the trench, shallow extensional seismicity occurs below the volcanic belt, and the geochemical data on some arc lava indicate the lack of contribution from the subducted material to magma genesis [*Verma*, 2002]. These signs all indicate that the volcanism may be related not to the subduction but to other processes such as rifting [e.g. *Márquez et al.*, 1999; *Verma*, 2002]. Intra-arc rifting and flat slab subduction reported for the Guerrero region are likely to involve complex dynamics of the subducting slab and the overriding mantle, which is not included in the model of the present study. Therefore, the later discussion only includes the modelling results for the Michoacan region. However, the modelling results for the Guerrero region will be useful for future research, particularly on the ETS-like events recently reported in this region [*Larson et al.*, 2007; *Payero et al.*, 2008].

For the shallow part of the subducting slab in the Colombia-Ecuador margin (**Figure 5.7**), I use the slab geometry reported by *Marcaillou et al.* [2006, 2008] based on seismic reflection data. For the deeper part, I inferred the slab geometry from the distribution of earthquake hypocenters in the EHB catalog. The red rectangle in the right panel indicates the range of BSR-derived heat flow values (not shown on the map) measured within a 50-km-distance from the profile line [*Marcaillou et al.,* 2006]. The Nazca plate is covered with a thick blanket (up to 4-km thick) of sediments that consist

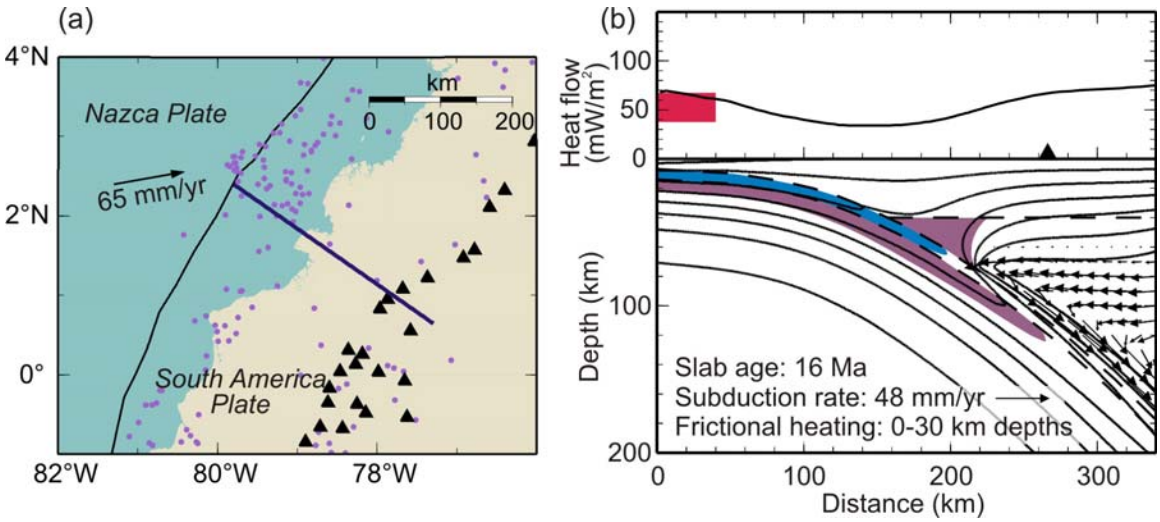

Figure 5.7. Colombia-Ecuador (index number 4). The red rectangle in the right panel indicates the range of BSR-derived heat flow values (not shown on the map) measured within a 50-km-distance from the profile line [*Marcaillou et al.,* 2006]. See **Figure 5.3** for explanation of symbols and colors.

mainly of turbidites at the trench [*Collot et al.*, 2005]. The relatively low heat flow near the trench is attributed to hydrothermal cooling of the oceanic crust prior to subduction [*Marcaillou et al.,* 2006], which is not included in the model presented here.

The above models for the three warm-slab subduction zones with a common MDD all predict sub-arc mantle temperatures of > 1250°C (**Table 5.2**), consistent with petrological constraints reviewed in **Section 2.5.1**. The model-predicted thermal and petrological states of the three subduction zones are in many aspects similar to those of northern Cascadia (**Figure 5.3**). They show that the peak crustal dehydration and the dehydration of antigorite in the subducting mantle occur at relatively shallow depths (See also **Table 5.2**), consistent with the seismologically inferred shallow depth of basalt-eclogite transformation and intraslab seismicity at these margins (**Figure 5.1a**). The shallow peak crustal dehydration provides ample fluid supply for mantle wedge

serpentinization but little fluid beneath the arc for melt generation. These model predictions are consistent with the inferred relatively high degree of mantle wedge serpentinization in Nankai (**Section 2.3.1**) and feeble arc volcanism in Nankai and Mexico (**Figure 5.1b**). Mantle wedge serpentinization is yet to be observationally investigated in Colombia-Ecuador and Mexico margins. The anomalously high rate of magma production rate at the Columbia-Ecuador margin (**Figure 5.1b**) may be explained by site-specific conditions. Although the downdip extent of the unusually thick layer of the subducting sediments mentioned earlier is unknown, it is a possible source of fluid for melt generation. Furthermore, the upper portion of the subducting mantle of the Colombia-Ecuador margin may be more hydrated than the other warm-slab subduction zones due to the vigorous hydrothermal circulation prior to subduction [*Marcaillou et al.*, 2006], and the dehydration of the hydrous minerals in the subducting mantle can provide more fluid at the sub-arc depth for melting than the other warm-slab subduction zones. As will be discussed in **Section 5.8.3**, the melting of the subducting crust may also contribute to the high level of arc volcanism.

5.5.2. Cold Continental Subduction Zones

The modelling results for eight continental subduction zones with a relatively or very cold slab (ϕ > 500 km) are presented in this subsection: SC Chile and northern Chile, Kyushu, northern Sumatra, Alaska, northern Costa Rica, northern Hikurangi, and Kamchatka. The results are shown in **Figures 5.8** through **5.15**.

In the SC Chile model (**Figure 5.8**), the slab geometry for the shallow part is based on that obtained by *Groβ et al.* [2008] using seismic reflection data. For the deeper part, I inferred the slab geometry from the hypocentre locations of intraslab earthquakes in the EHB catalog and *H* determined by *Syracuse and Abers* [2006].

In the Kyushu model (**Figure 5.9**), I adopt the slab geometry model reported by *Wang et al.* [2004] based primarily on intraslab earthquake distribution.

I infer the slab geometry in northern Sumatra (**Figure 5.10**) from the hypocentre locations of intraslab earthquake in the EHB catalog and *H* determined by *England et al.* [2004].

In the Alaska model (**Figure 5.11**), the slab geometry of *Oleskevich et al.* [1999] is used, which was obtained by using seismic reflection and refraction data and earthquake distribution.

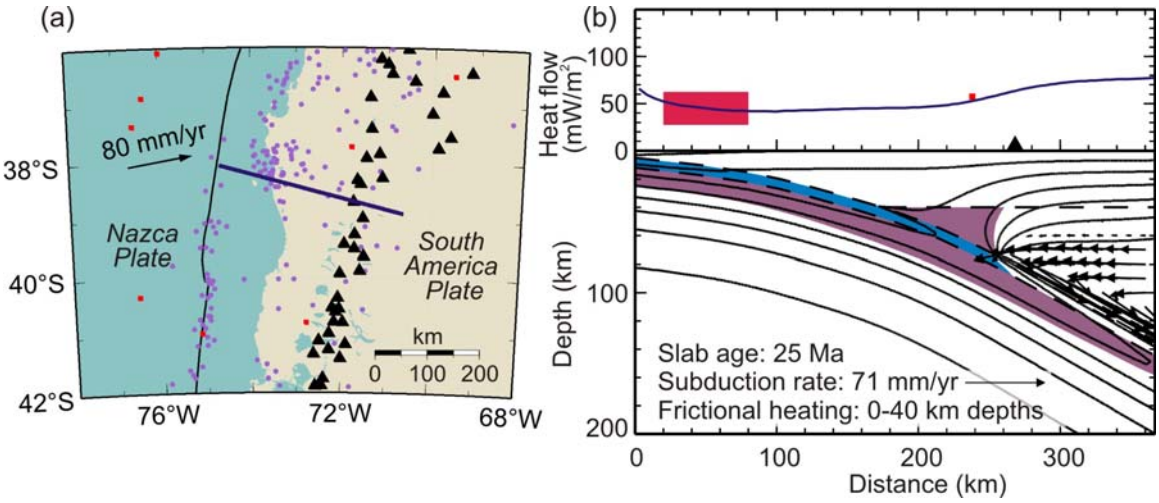

Figure 5.8. SC Chile (index number 5). The red rectangle in the right panel indicates the range of BSR-derived heat flow values (not shown on the map) measured at ~120-km south of the profile line [*Grevemeyer et al.*, 2003]. The rest of the heat flow data (red dots) are from *GHFD*. See **Figure 5.3** for explanation of symbols and colors.

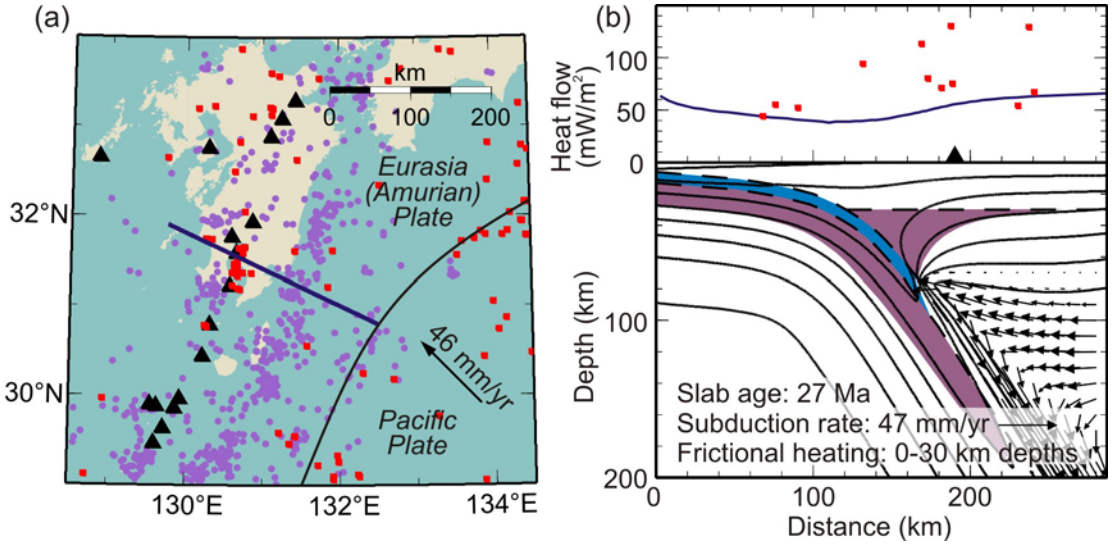

Figure 5.9. Kyushu (index number 6). Heat flow data are from *Tanaka et al.* [2004]. See **Figure 5.3** for explanation of symbols and colors.

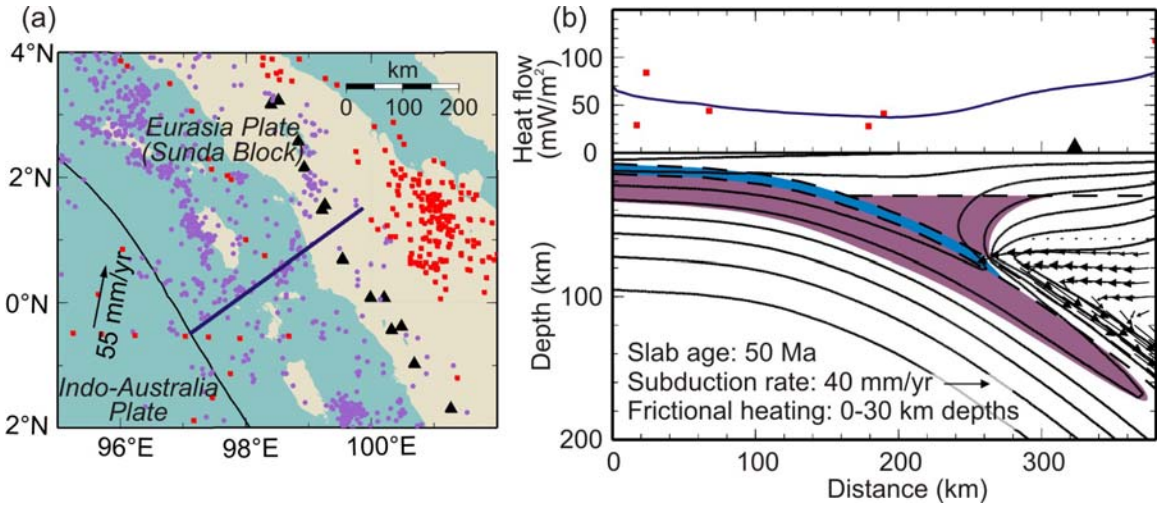

Figure 5.10. Northern Sumatra (index number 7). Heat flow data are from *GHFD*. See **Figure 5.3** for explanation of symbols and colors.

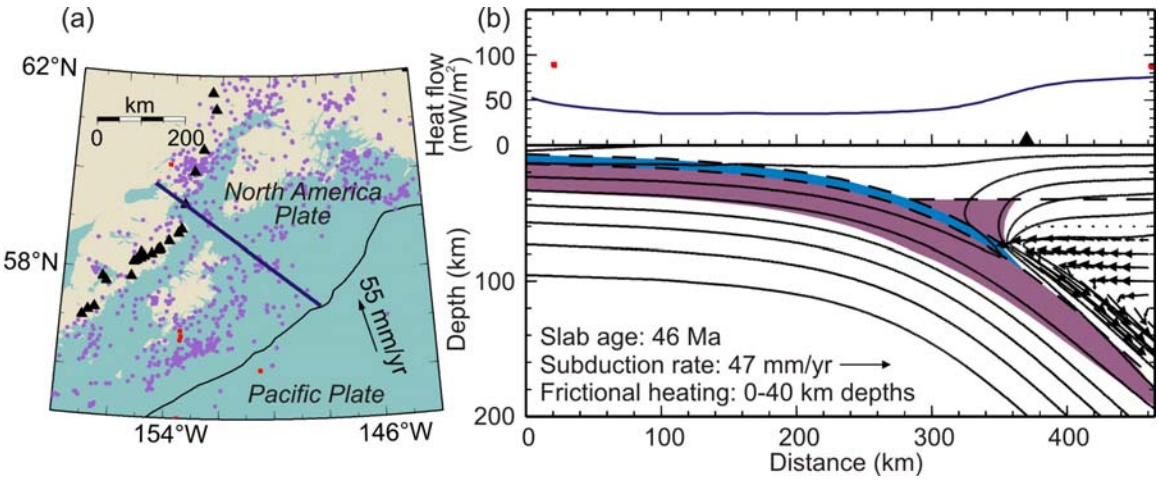

Figure 5.11. Alaska (index number 8). Heat flow data are from *GHFD*. See **Figure 5.3** for explanation of symbols and colors.

For the northern Chile model (**Figure 5.12**), I use the slab geometry reported by *Sallarès and Ranero* [2005] for the shallow part and infer the deeper part from the hypocentre locations of intraslab earthquakes in the EBH catalog. However, the composite model indicates a relatively sharp bending at shallow depth (< 30 km), which is mechanically less plausible for the relatively old slab. Therefore, I manually reduced the sharpness of the slab curvature slightly in the model construction.

I adopt the slab geometry of *Peacock et al.* [2005] in the northern Costa Rica model (**Figure 5.13**), which was inferred from earthquake hypocenters in the EHB catalog and those determined by *Protti et al.* [1995] and *Newman et al.* [2002] using local networks. The slab geometry model is consistent with *H* determined by *Syracuse and Abers* [2006]. Seismic images of the incoming Cocos plate near the model profile show bending-related faults penetrating to 18-20 km depth, well into the oceanic mantle [*Ranero et al.*, 2003]. Basement outcrops are also commonly observed on the incoming Cocos plate in the region. These outcrops and faults are likely to allow vigorous hydrothermal circulation

and efficient cooling of the basement [*Harris and Wang*, 2002; *Fisher et al.*, 2003]. The regional-scale model of the present study does not include this effect. This explains the low observed heat flow values near the trench compared to the predicted values.

In the northern Hikurangi model (**Figure 5.14**), I use the slab geometry model of *Reyners et al.* [2006], which was inferred from the distribution of intraslab earthquakes (purple dots) located by the local network. At this margin, continental rifting occurs within the TVZ, causing upwelling of mantle and decompressional melting over a relatively wide area and providing additional heat and melts. This causes the volcanic zone to appear wider than would be without the effect of rifing, such that the volcanic front indicated by the solid triangle does not represent a normal location of the volcanic arc. During this dissertation research, I developed conceptual tectonic models to explain the thermal effects of continental rifting within the TVZ and also the effects of collision-

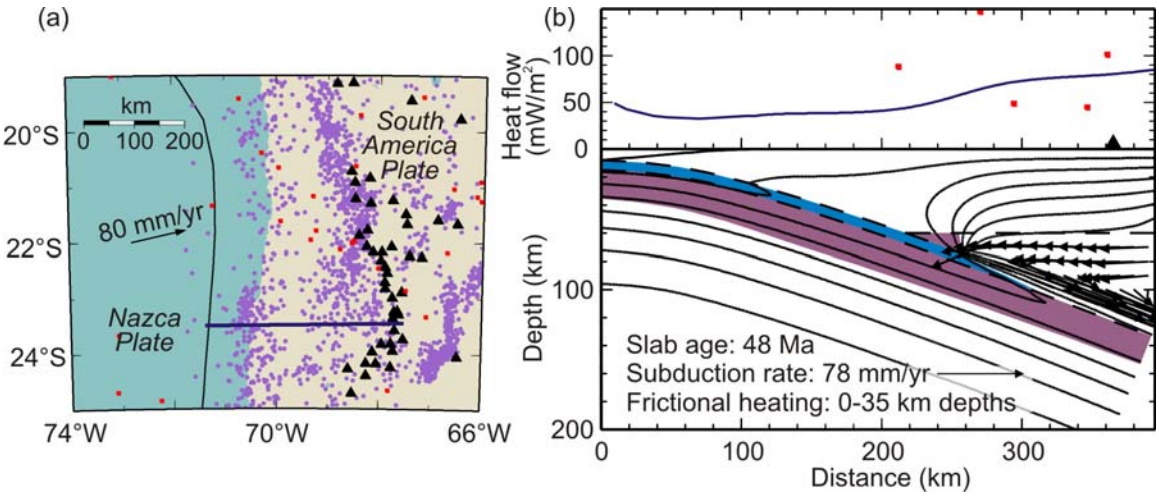

Figure 5.12. Northern Chile (index number 9). Heat flow data are from *GHFD*. See **Figure 5.3** for explanation of symbols and colors.

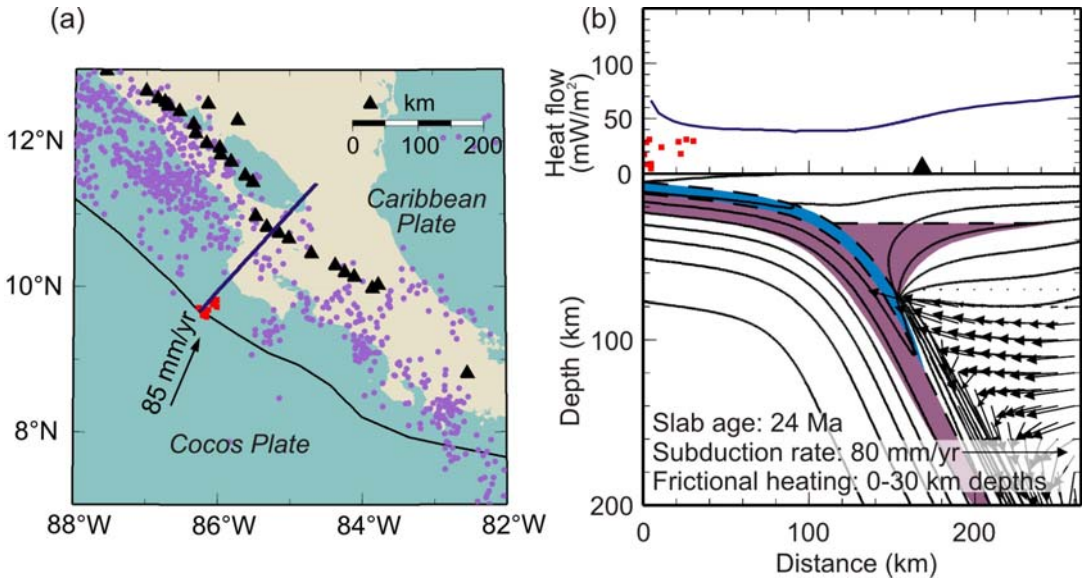

Figure 5.13. Northern Costa Rica (index number 10). Surface heat flow data are from *Langseth and Silver* [1996] and *Kimura et al.* [1997]. See **Figure 5.3** for explanation of symbols and colors.

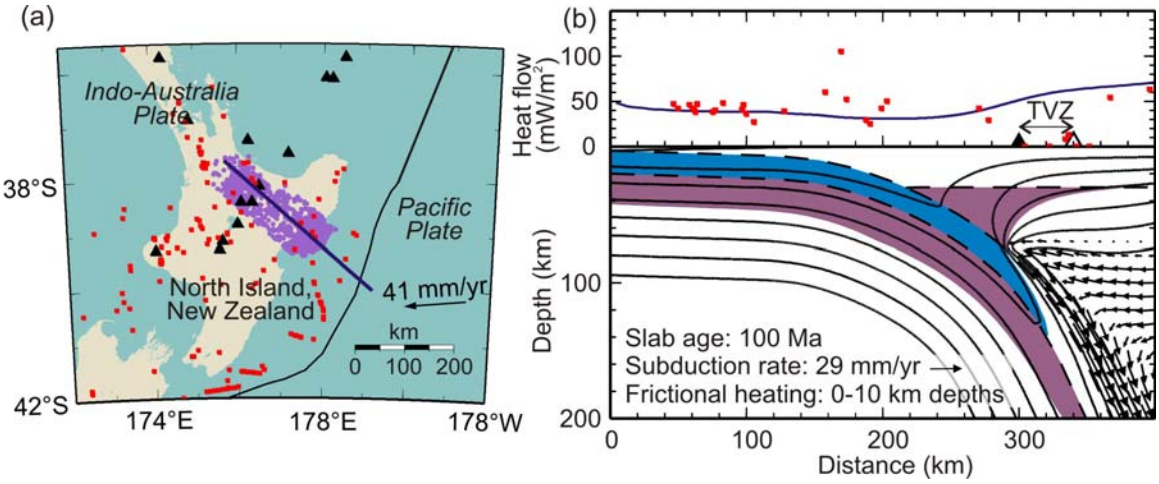

Figure 5.14. Northern Hikurangi (index number 12). Offshore heat flow data plotted in (b) are from *Townend* [1997] and the rest are from *GHFD*. The open triangle in (b) represents the landward end of the ~40-km-wide Taupo Volcanic zone (TVZ). See **Figure 5.3** for explanation of symbols and colors.

dominated convergence to the south on mantle wedge flow and thermal structure. The results are summarized in a poster, "Modelling the Thermal Regime of the Hikurangi Subduction Zone" by I. Wada, J. Townend, K. Wang, M. Reyners, and S. Ellis, which was presented by J. Townend at Geological Society of New Zealand and New Zealand Geophysical Society Joint Conference in December 2007. The magma production in northern Hikurangi is known to be unusually voluminous (**Figure 5.1b**). Along this margin, the thick (~17 km) oceanic Hikurangi Plateau is being subducted [*Davy and Wood*, 1994] as mentioned in **Section 5.3.2**. The large fluid supply from the thick subducting crust to the sub-arc mantle, in conjunction with rifting, accounts for the anomalously high magma production rate.

In the Kamchatka model (**Figure 5.15**), the slab geometry was obtained in this study using earthquake hypocenters in the EHB catalog and *H* determined by *England et*

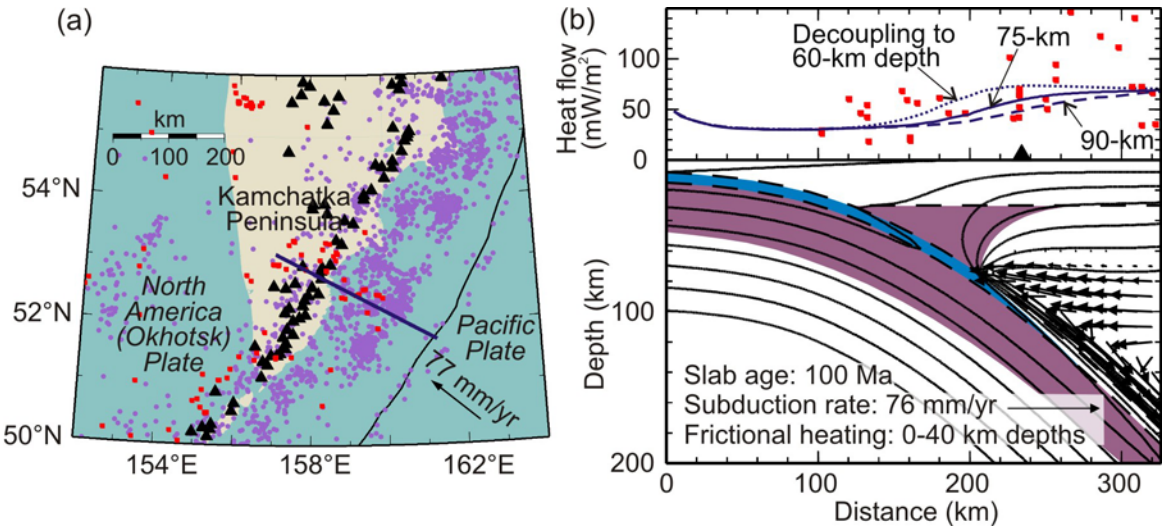

Figure 5.15. Kamchatka (index number 15). Surface heat flow data are from *Tanaka et al.* [2004]. See **Figure 5.3** for explanation of symbols and colors.

al. [2004]. There are relatively dense heat flow observations on this margin. I tested the surface heat flow patterns using MDD of 60, 75, and 90 km, a similar exercise performed for Cascadia and NE Japan in **Section 5.4**. The results also show that the MDD of around 75 km explains the observed surface heat flow while satisfying the high sub-arc mantle temperatures.

The sub-arc mantle temperatures predicted by the above models for the eight cold-slab subduction zones are consistent with petrological constraints (**Table 5.2**; **Section 2.5.1**). The model-predicted thermal and petrological states of the eight subduction zones are in strong contrast with those of the warm-slab subduction zones presented in the previous section. The peak crustal dehydration occurs mostly at depths greater than 75 km beneath the hot and flowing apart of the mantle wedge, and the zone of antigorite stability in the subducting mantle extends as deep as ~290 km depth (**Table 5.2**). These modelling results are consistent with the seismologically inferred greater depths of basalt-eclogite transformation and intermediate-depth intraslab seismicity (**Figure 5.1a** and **b**). Deeper dehydration provides ample fluid beneath the arc region but little fluid beneath the stagnant part of the mantle wedge, explaining the observed higher magma production (**Figure 5.1c**) and less evidence for mantle wedge serpentinization in cold-slab subduction zones than in warm-slab subduction zones (**Section 2.3.3**).

5.5.3. Cold Ocean-Ocean Subduction Zones

Four ocean-ocean margins are investigated in this study: Aleutians, Mariana, Kermadec, and Izu. In the Aleutian model (**Figure 5.16**), the slab geometry was obtained

using earthquake hypocenters in the EHB catalog. In the model, the depth of the slab beneath the arc is 95 km, intermediate of the two values of *H* obtained by *England et al.* [2004] for the regions east and west of my study region (**Table 2.1**). For the Mariana, Kermadec, and Izu models (**Figures 5.17** through **5.19**, respectively), the slab geometry is obtained using earthquake hypocenters in the EHB catalog and *H* determined by *England et al.* [2004].

The thermal and petrological characteristics predicted by the models for the four ocean-ocean margins are similar to those for the cold continental subduction zones presented in the previous section because of the similar thermal state of the subducting slab. However, some difference is in the thermal and petrological states of the forearc mantle wedge. At ocean-ocean margins, the mantle wedge overriding the subducting slab at shallow depths is cold and can host lower-temperature serpentine species chrysotile and lizardite as discussed in **Section 2.3.3** and shown in the modelling results (**Figures 5.16** through **5.19**). Although there is little supply of metamorphic fluid from the cold subducting slab at shallow depths, the collapse of pore space in the subducting sediments and fractured igneous crust provides fluid to serpentinize the shallow part of the mantle wedge. A high degree of mantle wedge serpentinization at the Izu-Bonin-Mariana margin is indeed evidenced by seismic observations [*Kamimura et al.*, 2002] and serpentinite deposits that were emplaced by serpentine mud volcanoes or by processes of large-scale faulting and rifting in the forearc [*Fryer*, 1996]. The nature of forearc mantle wedge serpentinization in cold-slab subduction zones thus depends on whether the overriding plate is oceanic or continental.

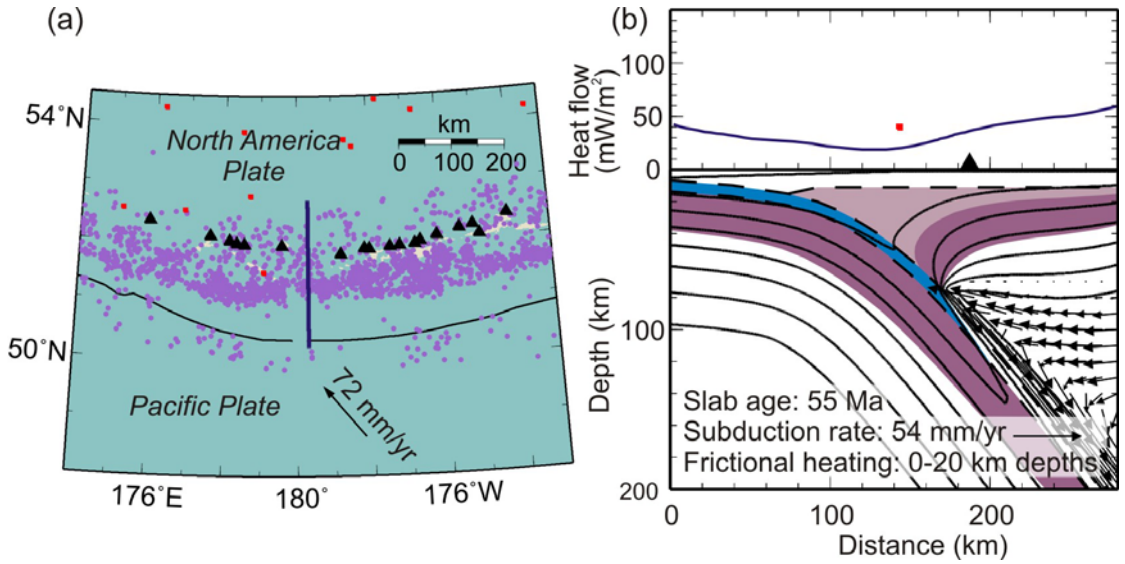

Figure 5.16. Aleutians (index number 11). Light purple in the mantle wedge indicates the zone of chrysotile/lizardite stability [*Evans*, 1977; 2004] (**Figure 2.5**). Heat flow data are from *GHFD*. See **Figure 5.3** for explanation of symbols and other colors.

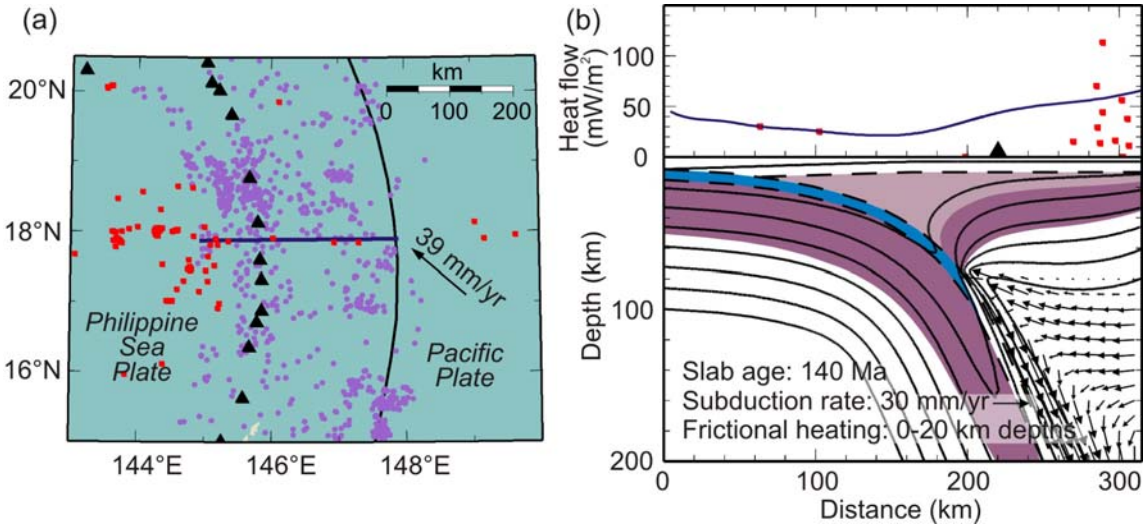

Figure 5.17. Mariana (index number 13). Heat flow data are from *GHFD*. See **Figures 5.3** and **5.16** for explanation of symbols and colors.

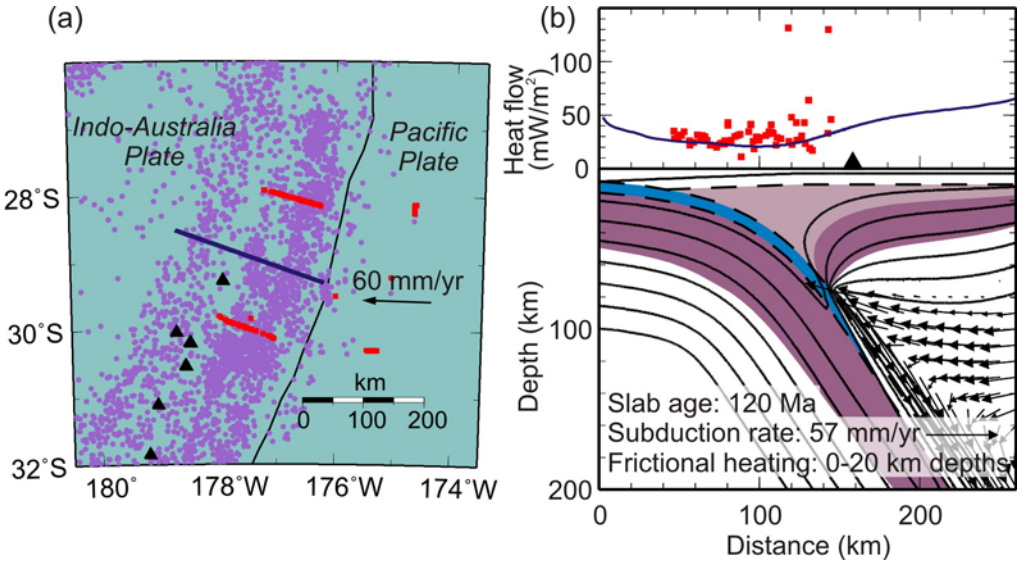

Figure 5.18. Kermadec (index number 14). Heat flow data are from *von Herzen et al.* [2001]. See **Figures 5.3** and **5.16** for explanation of symbols and colors.

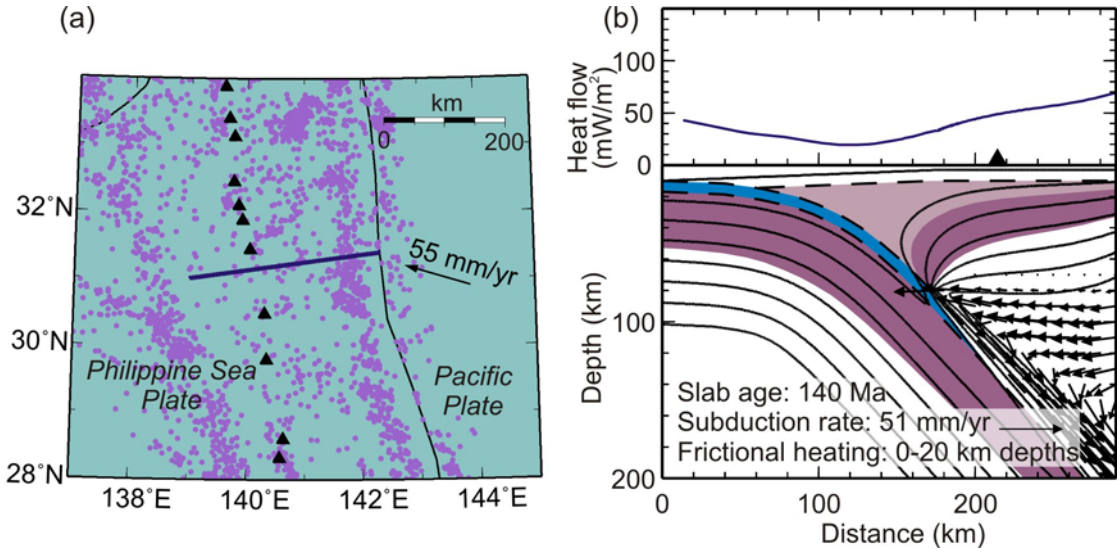

Figure 5.19. Izu (index number 16). Heat flow data are from *GHFD*. See **Figures 5.3** and **5.16** for explanation of symbols and colors.

5.6. Common Maximum Depth of Decoupling: Uniform Subduction Zone Configuration

In the models of all the seventeen subduction zones, the mantle beneath the arc is flowing and hot, with the temperature exceeding 1200°C, consistent with the thermal condition required for melt generation (**Figure 5.20**). Because the ascent of melt does not necessarily follow a strictly vertical path, the source region of melt may not be directly beneath the arc, and the model-predicted sub-arc mantle temperature may deviate slightly from the actual temperature of the melt source region. Furthermore, the exact thermal condition of mantle melting depends strongly on fluid content. A relatively wide range of sub-arc mantle temperature predicted by the models is consistent with laboratory predictions and theoretical expectations.

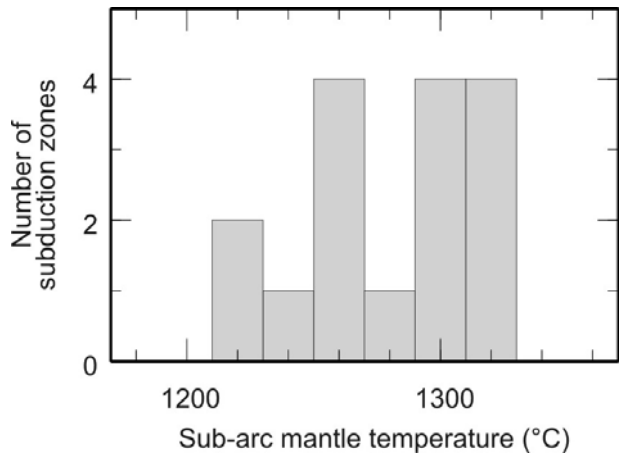

Figure 5.20. The distribution of the maximum mantle temperature beneath the regional average location of the volcanic arc predicted for all subduction zones with the 75-km maximum depth of decoupling except northern Hikurangi where ongoing continental rifting makes it difficult to pinpoint the location of the arc (**Figure 5.14**).

In contrast to the flowing and hot mantle beneath the arc, the stagnant mantle wedge in most of the forearc is rather cold and does not provide the thermal condition for volcanism. This explains why arc volcanism does not occur in the forearc. Odd volcanoes occasionally occur in the forearc, such as Mt. St. Helen in Cascadia which is situated some 35 km seaward of the rest of the Cascade volcanoes, but this situation is extremely rare and may be explained by an inclined path of the ascending magma controlled by site-specific geological structures. Furthermore, such volcanism may produce lavas that are

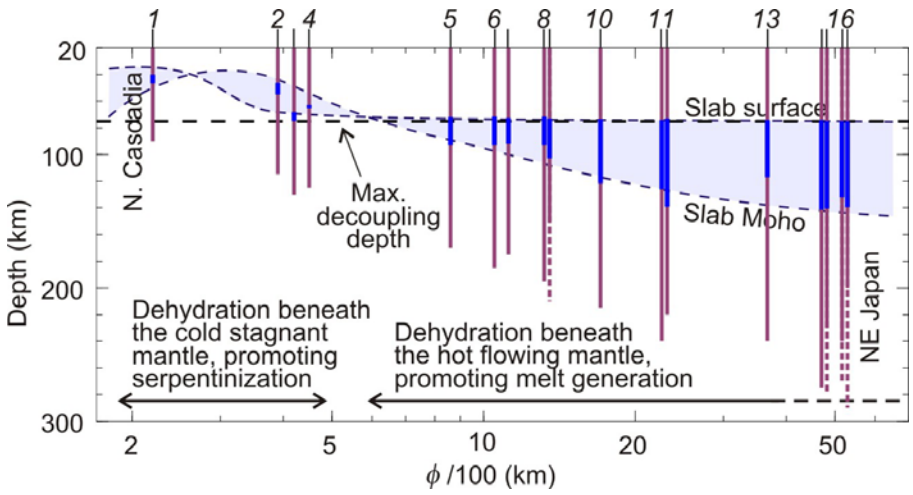

Figure 5.21. The depth range of peak crustal dehydration (thick blue lines) predicted by thermal models of the seventeen subduction zones plotted against the thermal parameter ϕ. Shaded area shows the trend of this depth range. The initial decrease in the peak crustal dehydration depth with increasing ϕ is due to the decrease in the basalt-eclogite transformation depth with decreasing temperature at low pressures. Depth range of antigorite stability in the subducting mantle below 20-km depth is shown with purple lines. Dashed purple lines indicate the portion of the depth range of antigorite stability that is extrapolated beyond the model domain from the modelling results. Small vertical bars and numbers at the top of the figure indicate the ϕ values and index numbers, respectively, of subduction zones.

geochemically different from those produced in the volcanic arc, enticing alternative explanations [*Defant and Drummond*, 1993].

The models also explain why arc volcanism is difficult to occur in the backarc. The generation of melts for arc volcanism requires both high temperature and sufficient fluid supply from the dehydrating slab. The model-predicted depths of peak crustal dehydration and maximum depth of antigorite stability in the subducting mantle for the seventeen subduction zone are summarized in **Table 5.2** and **Figure 5.21**. The models for all the subduction zones predict that the temperature of the upper part of the subducting slab increases abruptly downdip from the MDD where it is in contact with the overriding flowing hot mantle. Due to this temperature increase, crustal dehydration in all slabs peaks at depths shallower than ~140-km depth and provide little fluid for arc volcanism downdip of this depth. The overlap of the regions of high temperature and high fluid supply by the dehydrating crust occurs in a narrow zone, especially for subduction zones with a steeply dipping slab (e.g. Mariana). In some subduction zones such as NE Japan and Kamchatka, volcanoes are present almost 100 km landward of the volcanic arc. The relatively wide zone of volcanism may partly be attributed to a shallow dip of the slab, but it can be explained by the deeper transportation of fluid by the subducting mantle. The modeling results for cold-slab subduction zones predict that the dehydration of antigorite in the subducting mantle continues to yield fluid beyond ~140 km depth. However, the rate of the fluid supply in general must be much lower because hydration of the mantle lithosphere prior to subduction is likely to be limited to very few deep-cutting faults and also because the zone of antigorite stability shrinks very slowly as the slab travels to greater depths (e.g., **Figure 5.4**). The low supply of fluid from the slab downdip

of ~140 km depth may explain why arc volcanism does not extend much farther landward than observed, even for the coldest slabs.

Models with a common MDD explain not only the similarity of *H* (**Figure 5.1c**) but also some important second-order characteristics of these depths, that is, the small variations in *H*. Faster subduction increases the velocity of mantle wedge flow, which transports heat from the backarc at a faster rate (**Figure 5.22b**). This brings the region of high temperatures and thus the volcanic arc slightly closer to the trench, resulting in a smaller *H*. A steeper slab enables the stream lines of the wedge flow to have a large vertical component and thus more effectively transports heat from greater depths (**Figure 5.22c**). This also brings the arc closer to the trench, but *H* is deeper because the geometrical effect of a steeper dip on the *H* overshadows that of the trenchward shift of the arc (Figure 10c). The variations in the subduction rate and slab dip thus can generate the observed range (±~20 km) of variation in *H*. This is consistent with the hypothesis that the kinematics of the subducting slab controls the mantle wedge flow pattern and thus the region of melt generation as proposed by *England et al.* [2004] and *Syracuse and Abers* [2006]. For example, the slight dependence of *H* on the convergence rate and slab dip seen in these models is consistent with the trends observed along the margins of Kamchatka through Marianas shown in Figure 3 of *Syracuse and Abers* [2006]. Statistical correlations of observed *H* values with the subduction rate and slab dip are difficult to assess because of the coexistence of the effects of the two parameters and errors in *H*. For example, *England et al.* [2004] and *Syracuse and Abers* [2006] obtained opposite effects of the slab dip on *H* or *H'*.

Although the majority of the *H* values are in the 80-120 km depth range and their

variation is consistent with the common MDD hypothesis, anomalous values of *H* observed in few subduction zones require further explanation. End-member small and large *H* values of 65 km and 130 km are reported for eastern Aleutians and Izu, respectively, by *England et al.* [2004]. The steeply dipping slab in eastern Aleutians

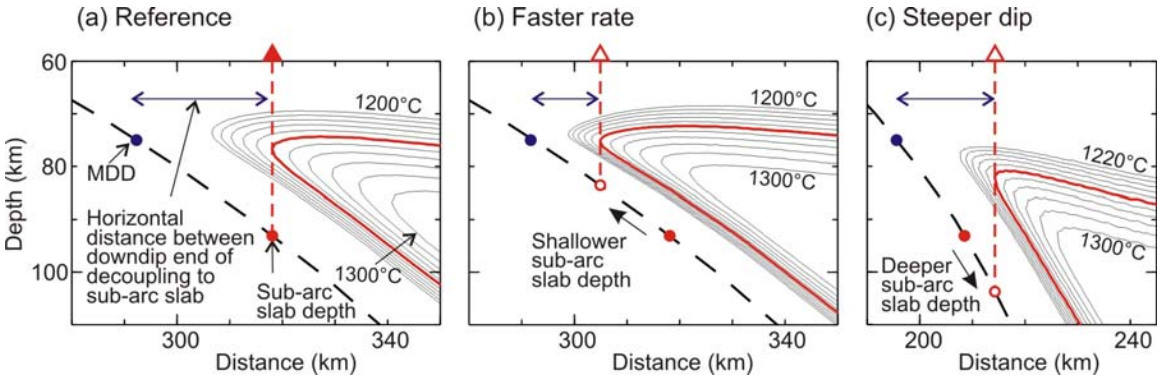

Figure 5.22. Generic subduction zone thermal models, illustrating the effects of subduction rate and slab dip on the thermally expected location of the volcanic arc and sub-arc slab depth *H*. Temperature contours between 1200°C and 1300°C at 10°C interval in the flowing part of the mantle wedge calculated by using (a) the northern Cascadia slab geometry and a 43 mm/yr subduction rate, (b) the northern Cascadia slab geometry and a 86 mm/yr subduction rate, and (c) the Mariana slab geometry with a 43 mm/yr subduction rate. The MDD is 75 km (filled blue circle) and the slab age is 8 Ma for all three models. The red contour line indicates 1250°C, which is the model-predicted maximum sub-arc mantle temperature in northern Cascadia. The filled red triangle and circle are the location of arc and *H*, respectively, in northern Cascadia. The horizontal distance (blue dashed line with a double arrowhead) between the downdip end of the decoupled interface and the most seaward point of the 1250°C contour, where melts are expected to be generated, is shorter for a faster subduction rate as shown in (b) or for a steeper slab dip as shown in (c). The shorter distance means that the arc is located closer to the trench. The predicted *H* (open red circle) is shallower for a faster subduction rate and deeper for a steeper slab.

results in a high sensitivity of H to the arc location, and the very old slab in Izu may generate intraslab earthquakes away from the slab surface, resulting in large uncertainties in H as discussed in Section 2.5. Furthermore, nonvertical melt migration may occur due, for example, to the effect of solid-state mantle wedge flow [e.g. *Cagnioncle et al.*, 2007] and can affect the location of arc relative to the region of melt generation and thus H. Alternatively, a presently anomalous subduction zone configuration may be caused by recent ongoing temporal changes in the regional tectonics or slab geometry.

5.7. Common Maximum Depth of Decoupling: Variations of Geophysical Processes with Slab Thermal Parameter

The preceding section demonstrates that the common MDD can explain the uniform configuration of subduction zones. The remaining question is whether this common MDD can also explain the strong slab-age dependent variability of the various observations reviewed in **Chapter 2** (**Figure 5.1a** and **b**).

The results summarized in **Figure 5.21** demonstrate that the maximum depths of peak crustal dehydration and serpentine stability in the subducting mantle increase systematically with ϕ. These trends explain the observed variability of the downdip extent of an LVL, which is interpreted to represent untransformed subducting crust (**Figures 2.4** and **5.1a**). An LVL detected in the cold-slab Aleutian, Kamchatka, Mariana, and NE Japan subduction zones by *Abers* [2005] extends to greater depths (>~150 km depths) than the model-predicted depths of basalt-eclogite transformation (<140 km) (See **Section 2.3.1**). There are a few possible explanations for this. One is that the

transformation in the gabbroic crust is kinetically delayed as mentioned in **Section 2.4.1**. Another possible explanation is the presence of hydrous minerals, particularly, serpentine, or free fluid in the subducting crust. For example, relatively low seismic velocities observed in the gabbroic oceanic lower crust formed at fast to intermediate-rate spreading centers is explained by alteration of olivine (~11%) to talc and/or serpentine [*Carlson et al.*, 2009]. After subduction, these hydrous minerals in the lower crust may persist to greater depths than the depths of basalt-eclogite transformation in the upper crust, causing low seismic velocity in the slab. Another possible explanation is that the deeper part of the LVL belongs to the mantle wedge or subducting mantle. For example, in NE Japan, *Kawakatsu and Watada* [2007] also identified an LVL at 140-190 km depths, in the similar depth range to *Abers* [2005], but they showed the layer to be in the mantle above the subducting slab. Based on a thermal model assuming an isoviscous mantle wedge, *Kawakatsu and Watada* [2007] interpreted this LVL to be serpentinite. However, the thermal models developed in the present study (**Figures 5.3** through **5.19**), as well as other thermal models that also incorporate the more realistic temperature-dependent mantle rheology [e.g., *van Keken et al.*, 2002; *Kneller et al.*, 2005], do not predict serpentine to be stable at these depths, regardless of the thermal state of the slab. Therefore, the LVL may represent the presence of melt that is redistributed along the zone of severe shear deformation immediately above the slab.

The trend shown in **Figure 5.21** also explains the depth range of intraslab seismicity and supports the hypothesis of dehydration embrittlement in both the subducting crust and mantle (See **Section 2.4.1**). Intraslab seismicity extends deeper than the model-predicted downdip extent of antigorite stability in very old cold slabs. This

may be due to the replacement of antigorite that survives to ~200 km depth by phase A, which contains 11.8 wt% H_2O and is stable to higher temperature than antigorite [*Schmidt and Poli*, 1998].

The modelling results show that in all the seventeen subduction zones, the stagnant and cold mantle wedge overlying the decoupled part of the interface is in a stable thermal condition for serpentinites (See **Section 2.3.3**). However, serpentinization depends also on the availability of fluid (**Figure 5.23**). The shallow crustal dehydration beneath the mantle wedge corner in warm-slab subduction zones provides substantially greater fluid supply than in cold-slab subduction zones where the peak crustal dehydration takes place at greater depths, beneath the hot flowing part of the mantle wedge. This model prediction is consistent with the relatively high degree of mantle wedge serpentinization reported for warm-slab subduction zones and a minor degree of serpentinization in subduction zones with very old and cold slabs except at ocean-ocean margins as explained in **Section 5.5**.

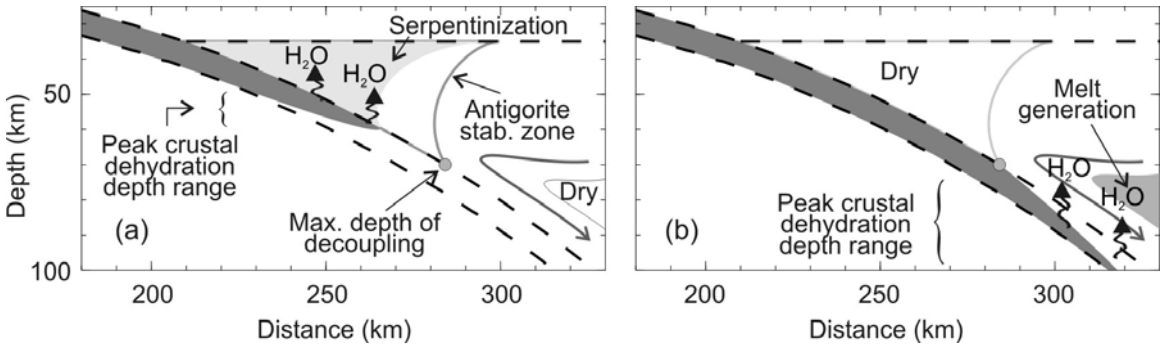

Figure 5.23. Schematic illustration of fluid supply at depth. (a) Peak crustal dehydration (boundary between the blue and the white areas in the subducting crust) beneath the cold and stagnant part of the mantle wedge promotes serpentinization, and (b) that beneath the hot and flowing part of the mantle promotes arc volcanism.

As discussed in **Section 2.4.3**, the ETS events observed in Cascadia and Nankai are likely to be associated with free fluids although the exact mechanism is unknown [*Obara*, 2002; *Kao et al.*, 2005; *Shelly et al.*, 2007]. The availability of free fluids depends on how much of the fluids is consumed in serpentinizing the mantle wedge. On the basis of seismic tomography at northern Cascadia, *Ramachandran and Hyndman* [2008, submitted manuscript] inferred that the degree of mantle wedge serpentinization decreases landward from the tip of the wedge. Although a typical serpentinization of ~15% is inferred from seismic velocity studies of subduction zones where there is evidence for mantle wedge serpentinization [*Carlson and Miller*, 2003], the degree of serpentinization at the wedge tip may be very high, conceivably approaching 100% given the diminishing vertical dimension of the wedge. At the two warm-slab subduction zones, Cascadia and Nankai, the shallow dehydration of the slab over the history of subduction may provide sufficient fluid to cause complete serpentinization of the very tip of the mantle wedge. The continuing dehydration of the subducting slab is likely to result in the accumulation of free fluid near the mantle wedge tip, which is consistent with the inferences of free fluid around the wedge tip at the two subduction zones and the proposed relation between the fluid and ETS events. In addition, models for cold-slab continental subduction zones predict a minor degree of mantle wedge serpentinization and thus shortage of fluid supply near the mantle wedge corner, consistent with the hypothesis that the ETS events are related to free fluid.

Modelling results show that slab dehydration peaks at shallow depths at warm-slab subduction zones. Although this is consistent with the generally low volcanic activity at warm-slab subduction zones (**Figure 5.1b**), arc volcanism does occur, implying that

some fluid must be transported to the sub-arc depth. Possible mechanisms of deep downdip fluid transfer include the subducting lower crust and mantle that contain hydrous minerals such as antigorite, talc, and chlorite, and the downdip transport of hydrated overriding mantle material by mantle wedge flow as discussed in **Section 2.5.1**. The modelling results suggest that both mechanisms can be at work. In the models for northern Cascadia and the other three warm-slab continental subduction zones, antigorite in the subducting mantle can be stable to a depth of ~100 km. In these models, although antigorite in the mantle wedge is not stable below the maximum depth of decoupling, the zone of chlorite stability just above the slab extends down deeper (**Figure 2.5**). Therefore, potentially the mantle wedge flow can transport chlorite down to the sub-arc depth.

Deeper dehydration of cold slabs provides significantly greater fluid supply for melt production beneath the arc, resulting in intense arc volcanism (**Figure 5.1b**). The correlation between the thermal state of the slab and fluid flux from the subducting slab into the magma source region is consistent with the observed variation in the enrichment of fluid-mobile element B in arc lavas among subduction zones [*Leeman*, 1996, and references therein].

The thermal and petrological states predicted by the thermal models for the seventeen subduction zones explain the observed systematic variation in geophysical processes as well as the uniform configuration of subduction zones. This supports the hypothesis that the common MDD reconciles the two contrasting characteristics of subduction zones.

5.8. Discussion

5.8.1. What Controls the Maximum Depth of Decoupling?

It has been shown in **Chapter 4** and this chapter that the strength contrast between the interface and the overriding mantle controls slab-mantle decoupling. The downdip termination of decoupling is caused by a downdip increase in the interface strength and/or a decrease in the mantle strength. The inferred narrow range of the MDD and the relatively uniform configuration of subduction zones suggest that some mechanism characterized by an inherent scale length is at work to cause the strength contrast to disappear at 70-80 km depth. Here, I speculate on possible mechanisms for the common MDD.

Metamorphic phase changes and associated dehydration reactions in the top part of the subducting crust and at the base of the mantle wedge affect the interface strengths. However, there is not a major phase change that takes place at the base of the mantle wedge at a common depth of 70-80 km (**Figures 5.24** and **5.25**). Therefore, phase changes are unlikely to be the main factor that causes the common MDD.

A possible role of hydrous minerals in terminating decoupling at a common depth is the change in their strength with depth. Recent laboratory results show that during dislocation creep, antigorite is significantly weaker than wet olivine at shallow depths, but the decrease in their strength with depth due to increasing temperature is faster for wet olivine than for antigorite, resulting in a decrease in the strength contrast between them (**Figure 2.2**) [*Hilairet et al.*, 2007]. The MDD may be regulated by the eventual disappearance of the strength contrast between the antigorite-bearing material along the

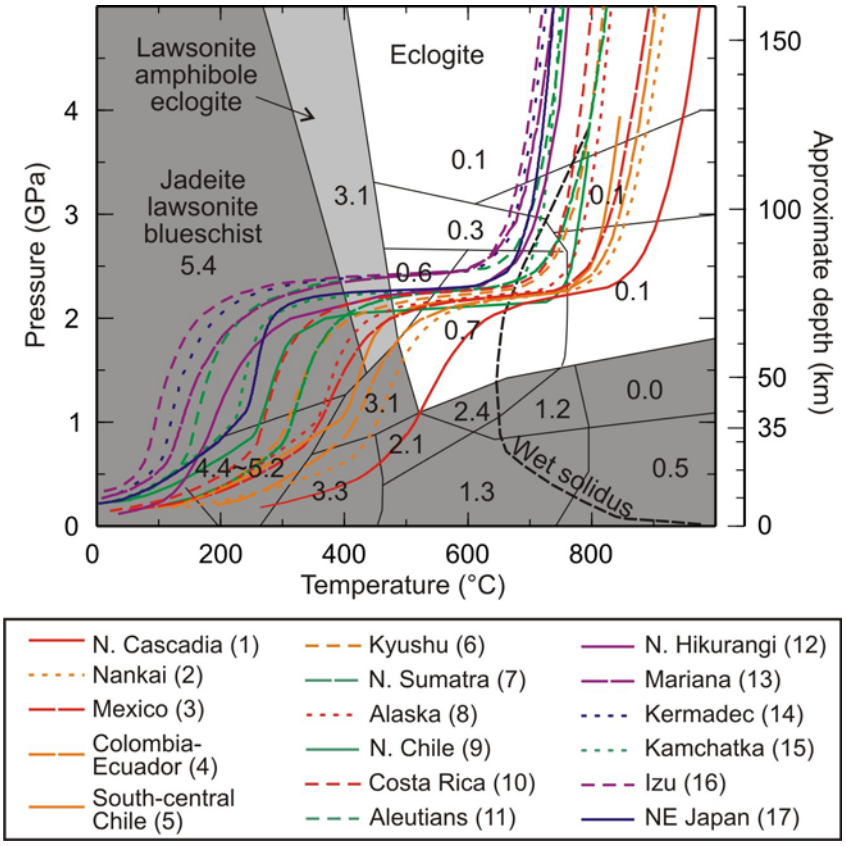

Figure 5.24. Temperatures along the plate interface predicted by the thermal models for the seventeen subduction zones overlain on a phase diagram for wet basalt shown in **Figure 2.3**. The pressure at depth is calculated by assuming 35-km-thick crust (2750 kg/m^3) and underlying mantle (3300 kg/m^3).

interface and the less hydrated overriding mantle with increasing depth.

Backarc heat flows for most subduction zones are about 80 mW/m^2 and are likely to be governed by a common process of small-scale convection (**Figure 1.1**) [*Currie and Hyndman*, 2006]. This probably determines the amount of heat supply into the arc and forearc region and thus regulates the overall strength of the forearc mantle. The effects of the backarc mantle thermal state on the forearc mantle thermal structure and rheology may give rise to an inherent scale length, which could regulate the MDD just like the Earth's thermal budget controls the thickness of the oceanic lithosphere. Regardless of

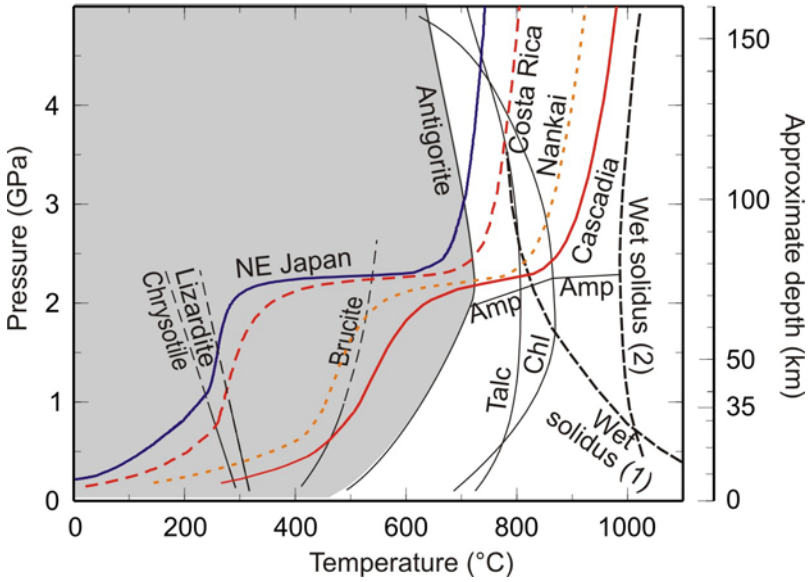

Figure 5.25. Temperatures along the plate interface predicted by the thermal models for Cascadia, Nankai, Costa Rica, and NE Japan overlain on a phase diagram for wet peridotite shown in **Figure 2.5.**

the specific mechanism, the common MDD is consistent with the fairly uniform backarc heat flow among subduction zones and therefore appears to be an expression of the subduction zone heat budget [*Currie et al.*, 2004a].

5.8.2. Seismic Anisotropy in the Forearc Mantle Wedge

The stagnant forearc mantle wedge seen in the models may have some implications for the interpretation of seismic anisotropy in this environment. In the upper mantle, lattice preferred orientation (LPO) of olivine develops during shear deformation, and the resultant seismic anisotropy causes orthogonal components of shear waves to travel at different velocities. Convergence-parallel fast direction is commonly observed in subduction zone upper mantle and is interpreted to indicate mantle flow and thus the

shear direction being aligned with plate convergence.

However, the fast direction in the forearc mantle wedge at many subduction zones is observed to be normal to the convergence direction, for which there are several interpretations [*Wiens and Smith*, 2003]. One hypothesis is that, in a "wet" condition at low temperature and high shear, the LPO of olivine results in a fast direction that is normal to the convergence direction (B-type olivine fabric) [*Jung and Karato*, 2001]. In contrast to conventional views, this mechanism does not require the mantle flow to change from convergence-parallel beneath the arc to margin-parallel in the forearc. There are some outstanding issues, though.

The first issue is whether there is significant shear deformation in the stagnant mantle wedge. In the models of *Kneller et al*. [2005, 2007], a velocity of about 3% of the plate convergence rate is assigned to the base of the forearc mantle wedge. The resultant slow "corner flow" creates enough shear deformation for the presence of the B-type fabric. Using a weak layer along the interface to simulate a condition of stress coupling, we have shown that there is little ongoing shear deformation in the stagnant wedge above the decoupled interface. One possibility is that the B-type fabric had been generated by deformation prior to the interface became decoupled and since "locked" in the rocks.

The second issue is how to explain the presence of arc-parallel fast direction observed in the arc-back arc mantle wedge of some subduction zones, such as Tonga [*Smith et al.*, 2001], Ryukyu [*Long and van der Hilst*, 2006], and Mariana [*Pozgay et al.*, 2007]. Beneath the arc and the back arc, temperatures are too high and stresses are too low to allow the formation of B-type olivine fabric.

The third issue is how to explain the convergence-parallel fast direction reported for

warm-slab subduction zones such as Cascadia and Nankai [*Currie et al.*, 2004b; *Tono*, 2006]. What causes the convergence-parallel fast direction in a serpentinized mantle wedge? Whatever mechanism that explains the anisotropy in cold-slab forearcs must explain why a warm-slab forearc behaves so differently.

Contrary to the above interpretations resorting to the anisotropy in the mantle wedge, *Faccenda et al.* [2008] argue that steeply dipping faults in the subducting slab and anisotropic hydrous minerals that form along the faults can explain the observed fast directions in the forearc regions of most subduction zones. They also explain that the hydrated upper portion of the young Juan de Fuca slab in northern Cascadia is likely to be too thin to cause significant anisotropy, and the convergence-parallel fast direction [*Currie et al.*, 2004b] is thus likely to be caused by the asthenospheric mantle flow. This also explains the convergence-parallel fast direction reported also for Nankai [Tono, 2006] where the slab is also young. This interpretation appears to be able to explain forearc seismic anisotropy in both cold-slab and warm-slab subduction zones.

5.8.3. Melting of Subducted Crust and Sediments

Earlier thermal models with an isoviscous mantle wedge predicted a relatively cool thermal condition of the subducting slab and no slab melting except for end-member warm-slab subduction zones [e.g. *Hacker et al.*, 2003a]. However, as discussed in **Section 2.5.1**, partial melting of the subducted sediment and crust has been reported for both warm-slab and cold-slab subduction zones on the basis of the geochemical signatures of arc lavas. The modeling results for the seventeen subduction zones show

that the temperature along the slab surface intersects the solidi of wet basalt (**Figure 5.24**) and fluid-saturated marine sediments (**Figure 5.26**). Thus, the uppermost part of the subducting crust and subducted sediment, if present, can potentially undergo partial melting, even in cold-slab subduction zones. Other thermal models with a temperature- and stress-dependent mantle wedge rheology show similar results [e.g. *Peacock et al.*, 2005].

Evidence for partial melting of the subducting crust is reported for Cascadia (Mount St. Helens) [*Defant and Drummond*, 1993], Nankai [*Morris et al.*, 1995], and Colombia-Ecuador [*Bourdon et al.*, 2002]. The larger fluid supply from the subducting mantle at the

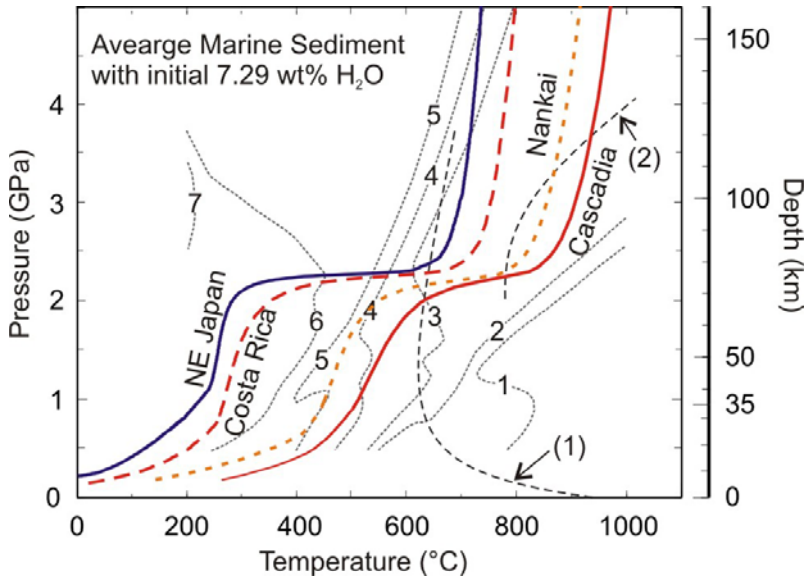

Figure 5.26. Temperatures along the plate interface predicted by thermal models for Cascadia, Nankai, Costa Rica, and NE Japan. Thin lines indicate weight percentage of H_2O computed for an average marine sediment composition of *Plank and Langmuir* [1998] [*Kerrick et al.*, 2001], and the solidus for fluid-saturated marine sediments experimentally determined by (1) *Nicholas et al*. [1994] and (2) *Johnson and Plank* [1999].

Colombia-Ecuador margin as discussed in **Section 5.5.2** may allow a greater degree of melting of the crust and thus contribute to the higher level of arc volcanism observed at this margin (**Figure 5.1b**).

5.9. Summary

A wide range of geophysical processes in subduction zones are known to depend on the thermal state of the subducting slab. Geological and geophysical observations show systematic variations of subduction zone processes with the thermal parameter of the subducting slab ϕ. In subduction zones with colder slabs, a layer of relatively low seismic-wave speed in the top part of the subducting slab, representing the untransformed basaltic crust, and intraslab seismicity extend to greater depths, and arc volcanism is more intense. ETS and mantle wedge serpentinization appear to be rare in cold-slab subduction zones, possibly indicating their dependence on the thermal state of the slab. In contrast, the configuration of subduction zones is surprisingly uniform in that the slab beneath the arc is at around 100 km depth regardless of the thermal state of the slab.

Toward reconciling this uniformity and diversity of subduction zones, we hypothesize that the subducting slab and the overriding mantle are decoupled to a common depth of 70-80 km depth in most, if not all, subduction zones, and the onset of mantle wedge flow downdip of the decoupled interface controls the uniform subduction zone configuration without significantly affecting the systematic variations in slab-age dependent subduction zone processes. To test this hypothesis, I have developed thermal models for seventeen subduction zones by prescribing interface decoupling to 75 km

depth. The models explain available surface heat flow observations.

The thermal models predict that the region of high temperatures (>1200°C) and thus mantle melting occurs where the slab is at ~100 km and greater depths for all the seventeen subduction zones. In contrast, the mantle wedge in most of the forearc is stagnant and cold, explaining why arc volcanism does not occur in the forearc region. Due to the sudden onset of mantle wedge flow at 70-80 km depth, crustal dehydration in most subduction zones peaks at depths shallower than 140 km. The much reduced fluid supply from the subducting slab to the overriding mantle wedge downdip of this depth explains why arc volcanism does not tend to occur in the backarc even though the mantle is as hot as beneath the arc. Therefore, the common MDD controls the location of arc and can explain the uniform configuration of subduction zones. The location of the arc can also be affected by other kinematic parameters and the specific path of the ascending arc magma, but these are likely second-order effects.

The model predictions are also consistent with the observed systematic variations of subduction zone processes. The model-predicted depths of dehydration in both the subducting crust and mantle are deeper for colder slabs, consistent with the observed increase in the maximum depth of an LVL and intraslab seismicity with ϕ. The models also predict that fluid supply near the forearc mantle wedge tip is significantly smaller in cold-slab subduction zones due to deeper slab dehydration than in warm-slab subduction zones, possibly explaining why there is less evidence for mantle wedge serpentinization and ETS in cold-slab subduction zones. However, deeper slab dehydration in cold-slab subduction zones provides more fluid to the sub-arc mantle than in warm-slab subduction zones, consistent with the increasing intensity of arc volcanism with ϕ. The sudden onset

of mantle wedge flow downdip of the decoupled interface also affects the thermal state of the slab but uniformly among different subduction zones owing to the common MDD, and therefore any systematic variations that depend on the thermal state of the slab are unaffected.

In this chapter, I have shown that a common depth of slab-mantle wedge decoupling reconciles the uniformity and diversity of subduction zones. Decoupling reflects a contrast between a stronger mantle wedge and a weaker subduction interface. The onset of coupling thus reflects the loss of the strength contrast. A mechanism that can reduce the strength contrast at a common depth of 70-80 km is the key to understanding the seemingly complex subduction zone geodynamics and is a critical subject of future research.

Chapter 6

Conclusions and Recommendations for Future Research

6.1. Conclusions

Geophysical and geological observations indicate that the shallow part of the forearc mantle wedge is cold and does not participate in mantle wedge flow. The necessary condition for the mantle wedge to be stagnant is that the slab and the mantle are decoupled. The degree of decoupling is controlled by the strength contrast between the two. In this dissertation, the effects of slab-mantle decoupling on the mantle wedge flow and subduction zone thermal structure are investigated by using a two-dimensional steady-state finite-element model. The model employs a temperature- and stress-dependent mantle wedge rheology and a viscous thin layer along the plate interface to represent the interface strength.

Using northern Cascadia as an example, it has been shown how the strength contrast between the mantle and interface may diminish with increasing depth due to the strong temperature-dependence of the mantle strength, leading to a change from decoupling to coupling. The weakened shallow part of the interface is always fully decoupled, but immediately downdip of the zone of decoupling the interface is always fully coupled, resulting in a sharp decoupling-coupling transition. The sharpness of the transition depends on the rheology assumed and increases with the nonlinearity of the flow system. The model also reveals that the flow in the mantle wedge is bimodal due to the nonlinear feedback between temperature and the mantle strength: the mantle either

does not flow at all or flows at a full rate compatible with the slab velocity. Varying the rheology of the interface and mantle wedge changes the maximum depth of decoupling (MDD), but the bimodal flow behaviour is persistent.

The bimodal behaviour of the wedge flow results in a strong thermal contrast between the stagnant and flowing parts of the mantle wedge. The stagnant part is cold because of conductive cooling caused by the descending slab, and the deeper flowing part is hot because the wedge flow brings in heat from greater depths and the backarc. The cold and hot parts of the mantle wedge result in low and high surface heat flows, respectively, and the low to high transition is governed by the MDD.

The model shows that an MDD of 70-80 km best explains the observed surface heat flow pattern in northern Cascadia, an end-member warm-slab subduction zone, and yields the high temperature (>1200°) beneath the volcanic arc as inferred from petrological and geochemical observations. A shallower MDD will overpredict surface heat flow in the forearc region, and a deeper MDD will result in sub-arc mantle temperatures that are too low for melt generation beneath the arc. A model for NE Japan, an end-member cold-slab subduction zone, also requires a MDD of 70-80 km in order to explain heat flow observations and the high temperatures beneath the arc.

A global synthesis of geological and geophysical observations illustrates that many processes in subduction zones vary systematically with the thermal state of the subducting slab. It is these variations that give rise to the rich diversity of subduction zones. In contrast, the configuration of subduction zones is rather uniform in that the arc always tends to be situated where the slab is at around 100 km depth. Thermal models for seventeen subduction zones including Cascadia and NE Japan show that the diversity and

uniformity can be reconciled if the MDD is 70-80 km in all these subduction zones. The shallow decoupling results in a stagnant forearc whose thermal regime is controlled mainly by the subducting slab. The deeper coupling leads to a sudden onset of mantle wedge flow, and thermal effect of this flow overshadows that of the slab in the arc region.

The models with the common MDD predict a region of high temperature (>1200°) where the slab is at ~100 km depth and peak crustal dehydration at depths shallower than 140 km depths. The 70-80 km common MDD thus provides a combination of high mantle temperature and fluid supply that is optimal for melt generation where the slab is at ~100 km depth, explaining the uniform configuration of subduction zones. The variations in subduction rate and slab dip among subduction zones affect the exact location of the high temperature region relative to the MDD and can explain the observed second-order variations in the sub-arc slab depth among subduction zones.

The models also explain the observed systematic variation of subduction zone processes with the thermal state of the slab. The depths of slab dehydration are greater for older and colder slabs, consistent with the seismologically inferred greater depths of basalt-eclogite transformation of the subduction crust and intraslab seismicity in older slabs. In these cold-slab subduction zones, the deeper slab dehydration provides ample fluid for melt generation beneath the arc but little fluid for mantle wedge serpentinization. In warm-slab subduction zones, the shallow slab dehydration provides ample fluid for serpentinization of the mantle wedge in the forearc but little fluid for melt generation beneath the arc.

This dissertation has demonstrated that the MDD is a key parameter that controls the thermal structure and hence geodynamics of subduction zones. The common MDD

presents a unified explanation for multidisciplinary observations and reconciles the process diversity and configuration uniformity of subduction zones. The recognition of the importance of the MDD provides guidance for future research.

6.2. Recommendations for Future Research

This dissertation has demonstrated that the MDD controls the mantle wedge flow and thermal structure. What remains unclear is the mechanism that controls the MDD. In some of the thermal models developed in this work, the MDD is controlled by the rheology of the interface layer. One obvious task is to understand better the mechanical properties of material along the interface, particularly antigorite, through further laboratory deformation experiments such as those performed by *Hilairet et al.* [2007] and *Chernak and Hirth* [2008]. Major petrological changes of the interface material are likely to lead to changes in their mechanical properties and could also control the MDD, although such changes have not been recognized.

Related to the above issue, but more important, is the question of what makes the MDD similar in different subduction zones. Feedback effects between decoupling and processes such as mantle wedge serpentinization and melting can potentially result in a common MDD. The backarc thermal regime affects the strength of the forearc mantle and thus slab-mantle decoupling, and the mechanism that controls the backarc thermal regime may give rise to the inherent scale length that leads to the common MDD. Development of models that incorporate self-consistent treatment of these mechanisms, although difficult, is an important topic for future research.

The models developed for all the seventeen subduction zones in this dissertation predict an abrupt increase in the temperature of the subducting crust beneath the seaward tip of mantle wedge flow at a relatively uniform depth owing to the common MDD. Due to the abrupt temperature increase, peak crustal dehydration in colder slabs is predicted to occur over a relatively narrow depth range. These model predictions are consistent with recent findings based on high-resolution seismic velocity and attenuation images that were obtained from the TUCAN Broadband Seismic Experiment in Nicaragua-Costa Rica [*Abers et al.*, 2008]. Upon further acquisition of such high-quality geophysical data, model predictions made in this dissertation need to be verified.

The stagnant and cold shallow part of the mantle wedge provides a stable thermal condition for serpentinization and can consume and store a large amount of fluid. Changes in the thermal and metamorphic states of the forearc mantle wedge thus affect the fluid budget at shallow depths, particularly in subduction zones with a young and warm slab that releases most of its fluid at such depths. If the mantle is fully serpentinized, fluid must migrate updip and upward from the hydrated region, taking part in other processes such as interplate and crustal earthquakes and ETS. An increase in temperatures of the hydrated mantle wedge due to a change in the plate boundary tectonics leads to release of fluid to the plate interface updip of the mantle wedge and to the overlying crustal material, even in the absence of dehydrating slab. Therefore, development of models for the evolution of the forearc mantle wedge is important for better understanding of the fluid control on geophysical processes. Such models should incorporate explicitly the phase changes associated with hydration and dehydration of the mantle wedge.

Bibliography

Abers, G. A. (2005), Seismic low-velocity layer at the top of subducting slabs: observations, predictions, and systematics, *Physics of the Earth and Planetary Interiors*, *149*, 7-29.

Abers, G. A., P. E. van Keken, E. A. Kneller, A. Ferris, and J. C. Stachnik (2006), The thermal structure of subduction zones constrained by seismic imaging: Implications for slab dehydration and wedge flow, *Earth and Planetary Science Letters*, *241*, 387-397.

Abers, G. A., L. MacKenzie, S. Rondenay, K. M. Fischer, E. Syracuse, and C. Rychert (2008), The Nicaragua-Costa Rica slab and wedge: imaging deep fluid pathways, *EOS Transactions of American Geophysical Union*, 89 (53), Fall Meeting Supplement, Abstract U52A-01.

Atwater, T. (1989), Plate tectonic history of the northeast Pacific and western North America, in *The Geology of North America*, vol. N, The Eastern Pacific Ocean and Hawaii, edited by E. L. Winterer, D. M. Hussong, and R. W. Decker, pp. 21– 72, Geological Society of America., Boulder, Colorado.

Audet, P., M. G. Bostock, N. I. Christensen, and S. M. Peacock (2009), Seismic evidence for overpressured subducted oceanic crust and megathrust fault sealing, *Nature*, *457*, doi:10.1038/nature07650.

Baba, T., Y. Tanioka, P. R. Cummins, and K. Uhira (2002), The slip distribution of the 1946 Nankai earthquake estimated from tsunami inversion using a new place model, *Physics of the Earth and Planetary Interiors*, *132*, 59-73.

Barckhausen, U., C. R. Ranero, R. von Huene, S. C. Cande, and H. A. Roeser (2001), Revised tectonic boundaries in the Cocos plate off Costa Rica: Implications for the segmentation of the convergent margin and for plate tectonic models, *Journal of Geophysical Research*, *106*, 19207-19220.

Batchelor, G. K. (1967), *An introduction to fluid dynamics*, Cambridge Univ. Press, New York, 615 pp.

Behn, M. D., G. Hirth, and P. B. Kelemen (2007), Trench-parallel anisotropy produced by foundering of arc lower crust, *Science*, *317*, 108-111.

Billen, M. I., and G. Hirth (2007), Rheological controls on slab dynamics, *Geochemistry, Geophysics, Geosystems*, *8*, Q08012.

Blackwell, D. D., J. L. Steele, M. K. Frohme, D. F. Murphey, G. R. Priest, and G. L. Black (1990a), Heat flow in the Oregon Cascade Range and its correlation with regional gravity, Curie point depths, and geology, *Journal of Geophysical Research*, *100*, 15,303-15,316.

Blackwell, D. D., J. L. Steele, S. Kelley, and M. A. Korosec (1990b), Heat flow in the State of Washington and thermal conditions in the Cascade Range, *Journal of Geophysical Research*, *95*, 19,495-19,516.

Blakely, R. J., T. M. Brocher, and R. E. Wells (2005), Subduction-zone magnetic anomalies and implications for hydrated forearc mantle, *Geology*, *33*, 445-448.

Bock, G., B. Schurr, and G. Asch (2000), High-resolution image of the oceanic Moho in the subducting Nazca plate from P – S converted waves, *Geophysical Research Letters*, *27*, 3929-3932.

Bock, Y., L. Prawirodirdjo, J. F. Genrich, C. Stevens, R. McCaffrey, C. Subarya, S. S. O. Puntodewo, and E. Calais (2003), Crustal motion in Indonesia from GPS measurements., *Journal of Geophysical Research*, *108* (B8), 2367, doi:10.1029/2001JB000324.

Bonatti, E. (1976), Serpentinite protrusions in the oceanic crust, *Earth and Planetary Science Letters*, *91*, 297-311.

Bostock, M. G., R. D. Hyndman, S. Rondenay, and S. M. Peacock (2002), An inverted continental Moho and serpentinization of the forearc mantle, *Nature*, *417*, 536-538.

Bourdon, E., J. -P. Eissen, M. Monzier, C. Robin, H. Martin, J. Cotton, and M. L. Hall (2002), Adakite-like lavas from Antisana Volcano (Ecuador): Evidence for slab melt metasomatism beneath the Andean northern volcanic zone, *Journal of Petrology*, *43*, 199-217.

Brocher, T. M., R. Parsons, A. M. Trehu, S. M. Snelson, and M. A. Fisher (2003), Seismic evidence for widespread serpentinized forearc upper mantle along the Cascadia margin, *Geology*, *31*, 267-270.

Brudzinski, M. R., C. H. Thurber, B. R. Hacker, and E. R. Engdahl (2007), Global prevalence of double Benioff zones, *Science*, *316*, 1472-1474.

Cagnioncle, A.-M., E. M. Parmentier, and L. T. Elkins-Tanton (2007), Effect of solid flow above a subducting slab on water distribution and melting at convergent plate boundaries, *Journal of Geophysical Research*, *112*, B09402, doi:10.1029/2007JB004934.

Calvert, A. J. (2004), Seismic reflection imaging of two megathrust shear zones in the northern Cascadia subduction zone, *Nature*, *428*, 163-167.

Cande, S. C., and D. V. Kent (1995), Revised calibration of the geomagnetic polarity timescale for the late Cretaceous and Cenozoic, *Journal of Geophysical Research*, 100, 6093-6095.

Carlson, R. L., and D. J. Miller (2003), Mantle wedge water contents estimated from seismic velocities in partially serpentinized peridotites, *Geophysical Research Letters*, *30*(5), 1250, doi:10.1029/2002GL016600.

Carlson, R. L., D. J. Miller, and J. Newman (2009), Olivine enigma: Why alteration controls the seismic properties of oceanic gabbros, *Geochemistry, Geophysics, Geosystems*, *10*, Q03o16, doi:10.1029/2008GC002263.

Carslaw, H. S., and J. C. Jaeger (1959), *Conduction of heat in solids*, Oxford University Press, Oxford, 510 pp.

Carter, N., and N. Tsenn (1987), Flow properties of continental lithosphere, *Tectonophysics*, *136*, 27-63.

Cassidy, J. F., and R. M. Ellis (1993), S wave velocity structure of the northern Cascadia subduction zone, *Journal of Geophysical Research*, *98*, 4407-4421.

Cassidy, J. F., and F. Waldhauser (2003), Evidence for both crustal and mantle earthquakes in the subducting Juan de Fuca plate, *Geophysical Research Letters*, *30*, doi:10.1029/2002GL015511.

Chen, Y. and W. J. Morgan (1990), A nonlinear rheology model for mid-ocean ridge axis topography, *Journal of Geophysical Research, 95*, 17,583-17,604.

Chen, J., and S. D. King (1998), The influence of temperature and depth dependent viscosity on geoid and topography profiles from models of mantle convection, *Physics of the Earth and Planetary Interiors*, *106*, 75–92.

Chernak, L. J., and G. Hirth (2008), Experimental constraints on the strength of antigorite deformed at high temperature and pressure, *EOS Transactions of American Geophysical Union*, *89*(53), Fall Meeting Supplement, Abstract T53C-1966.

Christensen, N. I. (2004), Serpentinites, peridotites, and seismology, *International Geology Review*, *46*, 795-816.

Clift, P., and P. Vannucchi (2004), Controls on tectonic accretion versus erosion in subduction zones: Implications for the origin and recycling of the continental crust, *Reviews of Geophysics*, *42*, RG2001, doi:10.1029/2003RG000127.

Collot, J. -Y., S. Migeon, G. Spence, Y. Legonidec, B. Marcaillou, J. -L. Schneider, F. Michaud, A. Alvarado, J. -F. Lebrun, M. Sosson, and A. Pazmino (2005), Seafloor margin map helps in understanding subduction earthquakes, *EOS Transactions of American Geophysical Union*, *86*, 463-465.

Conder, J. A., D. Wiens, J. Morris (2002), On the decompression melting structure at volcanic arcs and back-arc spreading centers, *Geophysical Research Letters*, *29*, doi:10.1029/2002GL015390.

Conder, J. A. (2005), A case for hot slab surface temperatures in numerical viscous flow models of subduction zones with improved fault zone parameterization, *Earth and Planetary Science Letters*, *149*, 155-164.

Crisp, J. A. (1984), Rates of magma emplacement and volcanic output, *Journal of Volcanology and Geothermal Research*, *20*, 177-211.

Currie, C. A. (2004), The thermal structure of subduction zones and backarcs, Ph.D. thesis, 267 pp., Univ. of Victoria, Canada, September.

Currie, C. A., R. D. Hyndman, K. Wang, and V. Kostoglodov (2002), Thermal models of the Mexico subduction zone: Implications for the megathrust seismogenic zone, *Journal of Geophysical Research*, *107*, B12, doi:10.1029/2001JB000886.

Currie, C. A., K. Wang, R. D. Hyndman, and J. He (2004a), The thermal effects of steady-state slab-driven mantle flow above a subducting plate: The Cascadia subduction zone and back arc, *Earth and Planetary Science Letters*, *223*, 35-48.

Currie, C. A., J. F. Cassidy, R. D. Hyndman, and M. G. Bostock (2004b), Shear wave anisotropy beneath the Cascadia subduction zone and western North American craton, *Geophysical Journal International*, *157*, 341-353.

Currie, C. A., and R. D. Hyndman (2006), The thermal structure of subduction zone back arcs, *Journal of Geophysical Research*, *111*, B08404, doi:10.1029/2005JB004024.

Davies, J. H. (1999), Simple analytical model for subduction zone thermal structure, *Geophysical Journal International*, *139*, 823-828.

Davies, J. H., and D. J. Stevenson (1992), Physical models of source region of subduction zone volcanic, *Journal of Geophysical Research*, *97*, 2037-2070.

Davis, E. E. and T. J. Lewis (1984), Heat flow in a back-arc environment: Intermontane and Omineca Crystalline Belts, southern Canadian Cordillera, *Canadian Journal of Earth Sciences*, *21*, 715-726.

Davis, E. E. and R. D. Hyndman (1989), Accretion and recent deformation of sediments along the northern Cascadia subduction zone, *Geological Society of America Bulletin*, *101*, 1465-1480.

Davis, E. E., R. D. Hyndman, and H. Villinger (1990), Rates of fluid expulsion across the northern Cascadia accretionary prism: Constraints from new heat flow and multichannel seismic reflection data, *Journal of Geophysical Research*, *95*, 8869-8889.

Davis, E. E., K. Wang, J. He, D. Chapman, H. Villinger, A. and Rosenberger (1997), An unequivocal case for high Nusselt number hydrothermal convection in sediment-buried igneous oceanic crust, *Earth and Planetary Science Letters*, *146*, 137-150, doi:10.1016/S0012-821X(96)00212-9.

Davy, B., and R. A. Wood (1994), Gravity and magnetic modelling of the Hikurangi Plateau, *Marine Geology*, *118*, 139-151.

Defant, M. J., and M. S. Drummond (1993), Mount St. Helens: Potential example of the partial melting of the subducted lithosphere in a volcanic arc, *Geology*, *21*, 547-550.

Defant, J. J., T. E. Jackson, M. S. Drummond, J. Z. de Boer, H. Bellon, M. D. Feigenson, R. C. Maaury, and R. H. Stewart (1992), The geochemistry of young volcanism throughout western Panama and southeastern Costa Rica: An overview, *Journal of the Geological Society, London*, *149*, 569-579.

Delahaye, E. J., J. Townend, M. E. Reyners, and G. Rogers (2009), Microseismicity but no tremor accompanying slow slip in the Hikurangi subduction zone, New Zealand, *Earth and Planetary Science Letters*, *277*, 21-28.

DeMets, D.C. (2001), A new estimate for present-day Cocos-Caribbean plate motion: Implications for slip along the Central American volcanic arc, *Geophysical Research Letters*, *28*, 4043-4046.

DeMets, C., R. G. Gordon, D. F. Argus, and S. Stein (1990), Current plate motions, *Geophysical Journal International*, *101*, 423-478.

DeMets, C., and T. H. Dixon (1999), New kinematic models for the Pacific-North America motion from 3 Ma to present: I. Evidence for steady motion and biases in the NUVEL-1A model, *Geophysical Research Letters*, *26*, 1921–1924.

DeMets, C., R. G. Gordon, D. F. Argus, and S. Stein (1994), Effect of recent revisions to the geomagnetic time-scale on estimate of current plate motions, *Geophysical Research Letters*, *21*, 2191-2194.

DeShon, H. R., and S. Y. Schwartz (2004), Evidence for serpentinization of the forearc mantle wedge along the Nicoya Peninsula, Costa Rica, *Geophysical Research Letters*, *31*, L21611, doi:10.1029/2004GL021179.

Dimalanta, C., A. Taira, G. P. Yumul Jr., H. Tokuyama, and K. Mochizuki (2002), New rates of western Pacific island arc magmatism from seismic and gravity data, *Earth and Planetary Science Letters*, *202*, 105-115.

Douglas, A., J. Beavan, L. Wallace, and J. Townend (2005), Slow slip on the northern Hikurangi subduction interface, New Zealand, *Geophysical Research Letters*, *32*, 2005L16305, doi:10.1029/2005GL023607.

Dragert, H., K. Wang, and T. S. James (2001), A silent slip event on the deeper Cascadia subduction interface, *Science*, *292*, 1525-1528.

Eberhart-Phllips, D., M. Reyners, M. Chadwick, and G. Stuart (2008), Three-dimensional attenuation structure of the Hikurangi subduction zone in the central North Island, New Zealand, *Geophysical Journal International*, *174*, 418-434.

Elkins Tanton, L.T., T. L. Grove, and J. Donnelly-Nolan (2001), Hot, shallow mantle melting under the Cascades volcanic arc, *Geology*, *29*, 631-634.

Engdahl, E. R., Van der Hilst, R. D., and Buland, R. P. (1998), Global teleseismic earthquake relocation with improved travel times and procedures for depth determination, *Bulletin of the Seismological Society of America*, *88*, 722-743.

England, P., R. Engdahl, and W. Thatcher (2004), Systematic variation in the depths of slabs beneath arc volcanoes, *Geophysical Journal International*, *156*, 377-408.

England, P., and C. Wilkins (2004), A simple analytical approximation to the temperature structure in subduction zones, *Geophysical Journal International*, *159*, 1138-1154.

Evans, B. W. (1977), Metamorphism of alpine peridotite and serpentinite, *Annual Review of Earth and Planetary Sciences*, *5*, 397-447.

Evans, B. W. (2004), The serpentine multisystem revised: Chrysotile is metastable, *International Geology Review*, 46, 479-506.

Faccenda, M., L. Burlini, T. V. Gerya, and D. Mainprice (2008), Fault-induced seismic anisotropy by hydration in subducting oceanic plates, *Nature*, *455*, doi:10.1038/natuure07376.

Fisher, A. T., C. A. Stein, R. N. Harris, K. Wang, E. A. Silver, M. Pfender, M. Hutnak, A. Cherkaoui, R. Bodzin, and H. Villinger (2003), Abrupt thermal transition reveals hydrothermal boundary and role of seamounts within the Cocos Plate, *Geophysical Research Letters*, *30*(11), 1550, doi:10.1029/2002GL016766.

Frohlich, C (1989), The nature of deep-focus earthquakes, *Annual Review of Earth and Planetary Sciences*, *17*, 227-254.

Flück, P., R.D. Hyndman, and K. Wang (1997), 3-D dislocation model for great earthquakes of the Cascadia subduction zone, *Journal of Geophysical Research, 102*, 20539-20550.

Fryer, P. (1996), Evolution of the Mariana convergent plate margin system, *Reviews of Geophysics*, *34*, 89-125.

Fukao, Y., S. Hori, and M. Ukawa (1983), A seismological constraint on the depth of basalt-eclogite transition in a subducting oceanic crust, *Nature*, *303*, 413-415.

Furukawa, Y. (1993), Depth of the decoupling plate interface and thermal structure under arcs, *Journal of Geophysical Research*, *98*, 20005-20013.

Furukawa, Y, and S. Uyeda (1989), Thermal state under the Tohoku arc with consideration of crustal heat generation, *Tectonophysics*, *164*, 175-187.

Gaetani, G. A., and T. L. Grove (1998), The influence of water on melting of mantle peridotite, *Contributions to Mineralogy and Petrology*, *131*, 323-346.

Gill, J. B. (1981), *Orogenic andesites and plate tectonics*, Springer-Verlag, New York, 390pp.

Global Heat Flow Database, The International Heat Flow Commission of the International Association of Seismology and Physics of the Earth's Interior, The global heat flow database of the international heat flow commission, http://www.heatflow.und.edu/index2.html. Last updated 08/10/2008.

Goto, K., T. Honda, H. Yakiwara, T. Kakuta, and H. Shimizu (2001), (in Japanese) *Chikyu Monthly*, *23*, 664-668.

Graeber, F. M., and G. Asch (1999), Three-dimensional models of P wave velocity and P-to-S ratio in the southern central Andes by simultaneous inversion of local earthquake data, *Journal of Geophysical Research*, *104*, 20237-20256.

Green, H. W. (1973), Experimental melting studies on a model upper mantle composition at high pressure under water-saturated and water-undersaturated conditions, *Earth and Planetary Science Letters*, *19* (1), 37-53.

Green, H. W. and Burnley, P. C. (1989), A new self-organizing mechanism for deep-focus earthquakes, *Nature*, *341*, 733.

Grevemeyer, I., J. L. Diaz-Naveas, C. R. Ranero, H. W. Villinger, and ODP Leg 202 Scientific Party (2003), Heat flow over the descending Nazca plate in central Chile, 32°S to 41°S: Observations from ODP Leg 202 and the occurrence of natural gas hydrates, *Earth and Planetary Science Letters*, *213*, 285-298.

Groβ, K., U. Micksch, and TIPTEQ Research Group, Seismics Team (2008), The reflection seismic survey of project TIPTEQ – the inventory of the Chilean subduction zone at 38.2°S, *Geophysical Journal International*, *172*, 565-571.

Grove, T. L., N. Chatterjee, S. W. Parman, and E. Medard (2006), The influence of H_2O on mantle wedge melting, *Earth and Planetary Science Letters*, *249*, 74-89.

Gurnis, M., and B. Hager (1988), Controls on the structure of subducted slabs, *Nature*, *335*, 317–321.

Grove, T. L., C. B. Till, E. Lev, N. Chatterjee, and E. Médard (2009), Kinematic variables and water transport control the formation and location of arc volcanoes, *Nature*, *459*, doi:10.1038/nature08044.

Haberland, C., A. Rietbrock, D. Lange, K. Batalille, and S. Hofmann (2006), Interaction between forearc and oceanic plate at the south-central Chilean margin as seen in local seismic data, *Geophysical Research Letters*, *33*, L23302, doi:10.1029/2006GL028189.

Hacker, B. R., S. M., Peacock, G. A. Abers, and S. D. Holloway (2003a), Subduction factory: 2. Are intermediate-depth earthquakes in subducting slabs linked to metamorphic dehydration?, *Journal of Geophysical Research*, *108*(B1), 2030, doi:10.1029/2001JB001129.

Hacker, B. R., G. A. Abers, and S. M. Peacock (2003b), Subduction factory: 1. Theoretical mineralogy, densities, seismic wave speeds, and H_2O contents, *Journal of Geophysical Research*, *108*(B1), 2029, doi:10.1029/2001JB001127.

Hall, C. E., K. M. Fisher, and E. M. Parmentier (2000), The influence of plate motions on three dimensional back-arc mantle flow and shear wave splitting, *Journal of Geophysical Research*, *105*, 20809-28033.

Hansen, F. D., and N. L. Carter (1982), Creep selected crustal rocks at 1000 MPa, *EOS Transactions of American Geophysical Union*, *63*, 437.

Hardy, N.C. (1991), Tectonic evolution of the easternmost Panama Basin: Some new data and interferences, *Journal of South American Earth Sciences*, *4*, 261-269.

Harris, R. N., and K. Wang (2002), Thermal models of the Middle America Trench at the Nicoya Peninsula, Costa Rica, *Geophysical Research Letters*, *29*, 2010, doi:10.1029/2002GL015406.

Hasegawa, A., S. Horiuchi, and N. Umino (1994), Seismic structure of the northeastern Japan convergent margin: a synthesis, *Journal of Geophysical Research*, *99*, 22295-22311.

Hilairet, N., B. Reynard, Y. Wang, I. Daniel, S. Merkel, N. Nishiyama, and S. Petitgirard (2007), High-pressure creep of serpentine, interseismic deformation, and initiation of subduction, *Science*, *318*, 1910-1913.

Hippchen, S., and R. D. Hyndman (2008), Thermal and structural models of the Sumatra subduction zone: Implications for the megathrust seismogenic zone, *Journal of Geophysical Research*, 113, B12103, doi:10.1029/2008JB005698.

Hirose, H., and K. Obara (2005), Repeating short- and long-term slow slip events with deep tremor activity around the Bungo channel region, Southwest Japan, *Earth Planets and Space*, *57*, 961-972.

Hirose, H., and K. Obara (2006), Short-term slow slip and correlated tremor episodes in the Tokai region, central Japan, *Geophysical Research Letters*, *33*, L17311, doi:10.1029/2006GL026579.

Hirth, G. and D. L. Kohlstedt (1996), Water in the oceanic upper mantle: Implications for rheology, melt extraction and the evolution of the lithosphere, *Earth and Planetary Science Letters*, *144*, 93-108.

Hirth, G., and D. Kohlstedt (2003), Rheology of the upper mantle and the mantle wedge: A view from the Experimentalists, in *Inside the Subduction Factory*, *Geophysical Monograph Series*, vol. 138, edited by J. Eiler, pp. 83-105, American Geophysical Union, Washington, D. C.

Hochstein, M. P. (1995), Crustal heat transfer in the Taupo Volcanic Zone (New Zealand): comparison with other volcanic arcs and explanatory heat source models, *Journal of Volcanology and Geothermal Research*, *68*, 117-151.

Honda, S. (1985), Thermal structure beneath Tohoku, Northeast Japan – A case study for understanding the detailed thermal structure of the subduction zone, *Tectonophysics*, *112*, 69-102.

Honda, S., and M. Saito (2003), Small-scale convection under the back-arc occurring in the low viscosity wedge, *Earth and Planetary Science Letters*, *216*, 703-715.

Honda, S., and T. Yoshida (2005), Effects of oblique subduction on the 3-D pattern of small-scale convection within the mantle wedge, *Geophysical Research Letters*, *32*, L13307, doi:10.1029/2005GL023106.

Honda, S., M. Saito, and T. Nakakuki (2002), Possible existence of small-scale convection under the back-arc, *Geophysical Research Letters, 29*(21), 2043, doi: 10.1029/2002GL015853.

Hori, S (1990), Seismic waves guided by untransformed oceanic crust subducting into the mantle: the case of the Kanto district, *Tectonophysics*, *176*, 335-376.

Hori, S., H. Inoue, Y. Fukao, and M. Ukawa (1985), Seismic detection of the untransformed 'basaltic' oceanic crust subducting into the mantle, *Geophysical Journal Royal Astronomical Society*, *83*, 169-197.

Hyndman, R. D., and K. Wang (1993), Thermal constraints on the zone of major thrust earthquake failure: The Cascadia subduction zone, *Journal of Geophysical Research*, *98*, 2039-2060.

Hyndman, R. D., and T. J. Lewis (1999), Geophysical consequences of the Cordillera-Craton thermal transition in southwestern Canada, *Tectonophysics, 306*, 397-422.

Hyndman, R. D., and S. M. Peacock (2003), Serpentinization of the forearc mantle, *Earth and Planetary Science Letters*, *212*, 417-432.

Hyndman, R. D., C. J. Yorath, R. M. Clowes, and E. E. Davis (1990), The northern Cascadia subduction zone at Vancouver Island: seismic structure and tectonic history, *Canadian Journal of Earth Sciences*, *27*, 313-329.

Hyndman, R. D., K. Wang, T. Yuan, and G. D. Spence (1993), Tectonic sediment thickening, fluid expulsion, and the thermal regime of subduction zone accretionary prisms: The Cascadia margin off Vancouver Island, *Journal of Geophysical Research*, *98*, 21865-21876.

Hyndman, R. D., M. Yamano, and D. A, Oleskevich (1997), The seismogenic zone of subduction thrust faults, *Island Arc*, *6*, 244-260.

Irifune, T. (1993), Phase transformations in the Earth's mantle and subducting slabs: Implications for their compositions, seismic velocity and density structures and dynamics, *Island Arc*, *2*, 55−71.

Ishikawa, T., and E. Nakamura (1994), Origin of the slab component in arc lavas from across-arc variation of B and Pb isotopes, *Nature*, *370*, 205-208.

Ito, E. and T. Katsura (1989), A temperature profile of the mantle transition zone, *Geophysical Research Letters*, *16*, 425-428.

Iwamori, H. (1997), Heat sources and melting in subduction zones, *Journal of Geophysical Research*, *102*, 14803-14820.

Iwamori, H. (1998), Transportation of H_2O and melting in subduction zones, *Earth and Planetary Science Letters*, *160*, 65-80.

Iyer, K., B. Jamtveit, J. Mathiesen, A. Malthe-Sørenssen, and J. Feder (2008), Reaction-assisted hierarchical fracturing during serpentinization, *Earth and Planetary Science Letters*, *267*, 503-516.

James, T. S., E. J. Gowan, and I. Wada (2009), Glacio-isostatic adjustment modeling of new relative sea-level observations from the northern Cascadia subduction zone, British

Columbia, Canada, *Journal of Geophysical Research*, *114*, B04405, doi:10.1029/2008JB006077.

Johnson, M. C., and T. Plank (1999), Dehydration and melting experiments constrain the fate of subducted sediments, *Geochemistry, Geophysics, Geosystems*, *1*, 1999GC000014.

Johnson, J. M., K. Satake, S. R. Holdahl, and J. Sauber (1996), The 1964 Prince William Sound earthquake: Joint inversion of tsunami and geodetic data, *Journal of Geophysical Research*, *101*, 523-532.

Jung, H., and S. Karato (2001), Water-induced fabric transitions in olivine, *Science*, *293*, 1460-1463.

Kamimura, A., J. Kasahara, R. Hino, M. Shinohara, R. Hino, H. Shiobara, G. Fujie, T. Kanazawa (2002), Crustal structure study at the Izu-Bonin subduction zone around 31°N: Implications of serpentinized materials along the subduction plate boundary, *Physics of the Earth and Planetary Interiors*, *132*, 105-129.

Kamiya, S., and Y. Kobayashi (2000), Seismological evidence for existence of serpentinized wedge mantle, *Geophysical Research Letters*, *27*, 819-822.

Kanamori, H., D. L. Anderson, and T. H. Heaton (1998), Frictional melting during the rupture of the 1994 Bolivian earthquake, *Science*, *279*, 839-842.

Kao, H., S. J. Shan, H. Dragert, G. Rogers, J. F. Cassidy, and K. Ramachandran (2005), Depth distribution of seismic tremors along the northern Cascadia margin, *Nature*, 436, 841-844.

Kao, H., K. Wang, R.-Y. Chen, I. Wada, J. He, and S. D. Malone (2008), Identifying rupture plane of the 2001 Nisqually, Washington Earthquake, *Bulletin of the Seismological Society of America*, *98*, 1546-1558.

Karato, S. (2008), *Deformation of Earth Materials: Introduction to the Rheology of the Solid Earth*, Cambridge Univ. Press, New York.

Karato, S., and P. Wu (1993), Rheology of the upper mantle: A synthesis, *Science*, *260*, 771-778.

Karato, S., and H. Jung (1998), Water partial melting and the origin of the seismic low velocity and high attenuation zone in the upper mantle, *Earth and Planetary Science Letters*, *157*, 193-207.

Kawakatsu, H., and S. Watada (2007), Seismic evidence for deep-water transportation in the mantle, *Science*, *316*, 1468-1471.

Kelemen, P. B., J. Rilling, E. M. Parmentier, L. Mehl, and B. R. Hacker (2003), Thermal structure due to solid-state flow in the mantle wedge beneath arcs, in *Inside the Subduction Factory*, *Geophysical Monograph Series*, vol. 138, edited by J. Eiler, pp. 293-311, American Geophysical Union, Washington, D. C.

Kerrick, D. M., and J. A. D. Connolly (2001), Metamorphic devolatilization of subducted marine sediments and the transport of volatiles into the Earth's mantle, *Nature*, *411*, 293-296.

Kimura, G., E. A. Silver, and P. Blum (1997), *Proceedings ODP, Initial Reports, 170*. Texas A&M University, College Station, TX.

Kincaid, C. and I. S. Sacks (1997), Thermal and dynamical evolution of the upper mantle in subduction zones, *Journal of Geophysical Research*, *102*, 12295-12315.

King, S. D., and J. Ita (1995), Effect of slab rheology on mass-transport across a phase transition boundary, *Journal of Geophysical Research*, *100* 20211-20222.

Kirby, S. H. (1983), Rheology of the lithosphere, *Reviews of Geophysics and Space Physics*, 21, 1458-1487.

Kirby, S. H. (1987), Localized polymorphic phase transitions in high-pressure faults and applications to the physical mechanism of deep earthquakes, *Journal of Geophysical Research*, *92*, 13789– 13800.

Kirby, S. H., B. William, B. Durham, and L. A. Stern (1991), Mantle phase changes and deep-earthquake faulting in subducting lithosphere, *Science*, *252*, 216-225.

Kirby, S. H., E. R. Engdahl, and R. Denlinger (1996a), Intermediate-depth intraslab earthquakes and arc volcanism as physical expressions of crustal and uppermost mantle metamorphism in subducting slabs, in *Subduction: Top to Bottom*, *Geophysical Monograph Series*, vol. 96, edited by G. E. Bebout, D. W. Scholl, S. H. Kirby, and J. P. Platt, pp. 195-214 American Geophysical Union, Washington, D. C.

Kirby, S. H, S. Stein, E. A. Okal, and D. C. Rubie (1996b), Metastable mantle phase transformations and deep earthquakes in subducting oceanic lithosphere, *Reviews of Geophysics*, *43*, 261-306.

Kneller, E. A., P. E. van Keken, S. Karato, and J. Park (2005), B-type olivine fabric in the mantle wedge: Insights from high-resolution non-Newtonian subduction zone models, *Earth and Planetary Science Letters*, *237*, 781-797.

Kneller, E. A., P. E. van Keken, I. Katayama, and S. Karato (2007), Stress, strain, and B-type olivine fabric in the fore-arc mantle: Sensitivity tests using high-resolution steady-state subduction zone models, *Journal of Geophysical Research*, *112*, B04406, doi:10.1029/2006JB004544.

Kneller, E. A., and P. E. van Keken (2008), Effect of three-dimensional slab geometry on deformation in the mantle wedge: Implications for shear wave anisotropy, *Geochemistry, Geophysics, Geosystems*, *9*, Q01003, doi:10.1029/2007GC001677.

Kodaira, S., T. Sato, N. Takahashi, A. Ito, Y. Tamura, Y. Tatsumi, and Y. Kaneda (2007), Seismological evidence for variable growth of crust along the Izu intraoceanic arc, *Journal of Geophysical Research*, *112*, B05104, doi:10.1029/2006JB004593.

Kohut, E. J., R. J. Stern, A. J. R. Kent, R. L. Nielsen, S. J. Bloomer, and M. Leybourne (2006), Evidence for adiabatic decompression melting in the Southern Mariana Arc from high-Mg lavas and melt inclusions, *Contributions to Mineralogy and Petrology*, *152*, 201-221.

Kostoglodov, V., and W. Bandy (1995), Seismotectonic constraints on the convergence rate between the Rivera and North American plates, *Journal of Geophysical Research*, *100*, 17977-17989.

Kostoglodov, V., W. Bandy, J. Domínguez, and M. Mena (1996), Gravity and seismicity over the Guerrero seismic gap, Mexico, *Geophysical Research Letters*, *23*, 3385-3388, 10.1029/96GL03159.

Koulakov, I. S. V. Sobolev, and G. Asch (2006), P- and S-velocity images of the lithosphere-asthenosphere system in the Central Andes from local-source tomographic inversion, *Geophysical Journal International*, *167*, 106-126.

Kushiro, I., Y. Syono, and S. Akimoto (1968), Melting of a peridotite nodule at high pressures and high water pressures, *Journal of Geophysical Research B Solid Earth Planets*, *73*, 6023-6029.

Lamb, S. (2006), Shear stresses on megathrusts: Implications for mountain building behind subduction zones, *Journal of Geophysical Research, 111*, B07401, doi:10.1029/2005JB003916.

Langseth, M. G., and E. A. Silver (1996), The Nicoya convergent margin – a region of exceptionally low heat flow, *Geophysical Research Letters, 23*, 891-894.

La Rocca, M., K. C. Creager, D. Galluzzo, S. Malone, J. E. Vidale, J. R. Sweet, and A. G. Wech (2009), Cascadia tremor located near plate interface constrained by S minus P wave times, *Science*, *323*, 620, doi:10.1126/science.1167112.

Larson, K. M., V. Kostoglodov, S. Miyazaki, and J. A. Santiago (2007), The 2006 aseismic slow slip event in Guerrero, Mexico: New results from GPS, *Geophysical Research Letters*, *34*, L13309, doi:10.1029/2007GL029912.

Lee, C., and S. D. King (2009), Effect of mantle compressibility on the thermal and flow structures of the subduction zones, *Geochemistry Geophysics Geosystems*, 10, Q01006, doi:10.1029/2008GC002151.

Leeman, W. P. (1996), Boron and other fluid-mobile elements in volcanic arc lavas: Implications for subduction processes, in *Subduction: Top to bottom*, *Geophysical Monograph Series*, *96*, edited by G. E. Bebout, D. W. Scholl, S. H. Kirby, and J. P. Platt, pp. 269-276, American Geophysical Union, Washington, D. C.

Le Pichon, X., S. Mazzotti, P. Henry, and M. Hashimoto (1998), Deformation of the Japanese Islands and seismic coupling: an interpretation based on GSI permanent GPS observations, *Geophysical Journal International*, *134*, 501-514.

Lewis, T. J., W. H. Bentkowski, E. E. Davis, R. D. Hyndman, J. G. Souther, and J. A. Wright (1988), Subduction of the Juan de Fuca Plate: Thermal consequences, *Journal of Geophysical Research*, *93*, 15207-15225..

Lewis, T. J., W. H. Bentkowskia, and J. A. Wright (1991), Thermal state of the Queen Charlotto basin, British Columbia: Warm, in *Evolution and Hydrocarbon potential of the Queen Charlott Basin, British Columbia*, *Geological Survey of Canada. Paper*, 90-10, 489-506.

Lewis, T. J., W. H. Bentkowski, and R. D. Hyndman (1992), Crustal temperatures near the Lithoprobe Southern Canadian Cordillera transect, *Canadian Journal of Earth Sciences*, *29*, 1197-1214.

Liu, Y., and J. R. Rice (2005), Aseismic slip transients emerge spontaneously in three-dimensional rate and state modeling of subduction earthquake sequences, *Journal of Geophysical Research*, *110*, B08307, doi:10.1029/2004JB003424.

Liu, Y., and J. R. Rice (2007), Spontaneous and triggered aseismic deformation transients in a subduction fault model, *Journal of Geophysical Research*, *112*, B09404, doi:10.1029/2007JB004930.

Long, M. D., and van der Hilst, R. D. (2006), Shear wave splitting from local events beneath the Ryukyu arc: Trench-parallel anisotropy in the mantle wedge, *Physics of the Earth and Planetary Interiors*, *155*, 300-312.

Magee, M. E., and M. D. Zoback (1993), Evidence for a weak interplate thrust fault along the northern Japan subduction zone and implications for the mechanics of thrust faulting and fluid expulsion, *Geology*, *21*, 809-812.

Manea, V. C., M. Manea, V. Kostoglodov, C. A. Currie, and G. Sewell (2004), Thermal Structure, Coupling and Metamorphism in the Mexican Subduction Zone beneath Guerrero, *Geophysical Journal International*, *158*, 775-784.

Manea, V. C., M. Manea, V. Kostoglodov, and G. Sewell (2005), Thermo-mechanical model of the mantle wedge in Central Mexican subduction zone and a blob tracing approach for the magma transport, *Physics of the Earth and Planetary Interiors*, *149*, 165-186.

Márquez, A., R. Oyarzun, M. Doblas, and S. P. Verma (1999), Alkalic (ocean-island basalt type) and calc-alkalic volcanism in the Mexican volcanic belt: A case for plume-related magmatism and propagating rifting at an active margin?, *Geology*, *27*, 51-54.

Marcaillou, B., G. Spence, J.-Y. Collot, and K. Wang (2006), Thermal regime from bottom simulating reflectors along the north Ecuador–south Colombia margin: Relation to margin segmentation and great subduction earthquakes, *Journal of Geophysical Research*, *111*, B12407, doi:10.1029/2005JB004239.

Marcaillou, B., G. Spence, K. Wang, J. -Y. Collot, and A. Ridodetti (2008), Thermal segmentation along the N. Ecuador-S. Colombia margin (1-4ºN): Prominent influence of sedimentation rate in the trench, *Earth and Planetary Science Letters*, *272*, 296-308.

Matsuzawa, T. N. Umino, A. Hasegawa, and A. Takagi (1986), Upper mantle velocity structure estimated from PS-converted wave beneath the north-eastern Japan Arc, *Geophysical Journal Royal Astronomical Society*, *86*, 767-787.

McCausland, W., S. Malone, and D. Johnson (2005), Temporal and spatial occurrence of deep non-volcanic tremor: from Washington to northern California, *Geophysical Research Letters*, *32*, L24311, doi:10.1029/2005GL024349.

McCrory, P. A., J. L. Blair, D. H. Oppenheimer, and S. R. Walter (2004), Depth to the Juan de Fuca slab beneath the Cascadia subduction margin: A 3-D model for sorting earthquakes, *U.S. Geological Survey Data Series*, *DS-91*, 1 CD-ROM.

McKenzie, D. (1969), Speculations on the consequences and causes of plate motion, *Geophysical Journal Royal Astronomical Society*, *18*, 1-32.

Mei, S. and Kohlstedt, D.L. (2000), Influence of water on plastic deformation of olivine aggregates 2. Dislocation creep regime, *Journal of Geophysical Research*, *105*, 21,471-21,481.

Mibe, K., T. Fujii, and A. Yasuda (1999), Control of the location of the volcanic front in island arcs by aqueous fluid connectivity in the mantle wedge, *Nature*, *401*, 259-262.

Millhollen, G. L., A. J. Irving, and P. J. Wyllie (1974), Melting interval of peridotite with 5.7 percent water to 30 kilobars, *Journal of Geology.*, *82* (5), 575-587.

Miura, S., S. Kodaira, A. Nakanishi, T. Tsuru, M. Takahashi, N. Hirata, and Y. Kaneda (2003), Structural characteristics controlling the seismicity of southern Japan Trench fore-arc region, revealed by ocean bottom seismographic data, *Tectonophysics*, *323*, 79-102.

Miura, S., N. Takahashi, A. Nakanishi, T. Tsuru, S. Kodaira, and Y. Kaneda (2005), Structural characteristics off Miyagi forearc region, the Japan Trench seismogenic zone, deduced from a wide-angle reflection and refraction study, *Tectonophysics*, *407*, 165-188.

Molnar, P., D. Freedman, and J. Shih (1979), Lengths of intermediate and deep seismic zones and temperatures in downgoing slabs of lithosphere, *Geophysical Journal Royal Astronomical Society*, *56*, 41-54.

Monger, J. W. H., and R. A. Price (2002), The Canadian Cordillera: Geology and tectonic evolution, *Canadian Society of Exploration Geophysicists Recorder*, February 2002, 17-36.

Moore, J. C. and D. Saffer (2001), Updip limit of the seismogenic zone beneath the accretionary prism of Southwest Japan: An effect of diagenetic to low-grade metamorphic processes and increasing effective stress, *Geology*, *29*, 183-186.

Morris, P. (1995), Slab melting as an explanation of Quaternary volcanism and seismicity in southwest Japan, *Geology*, *23*, 395-398.

Morrow, C. A., D. E. Moore, and D. A. Lockner (2000), The effect of mineral bond strength and adsorbed water on fault gouge frictional strength, *Geophysical Research Letters*, *27*, 815-818.

Mortimer, N., and D. Parkinson (1996), Hikurangi Plateau: A Cretaceous large igneous province in the southwest Pacific Ocean, *Journal of Geophysical Research*, *101*, 687-696.

Müller, R. D., W. R. Roest, J. -Y. Royer, L. M. Gahagan, and J. G. Sclater (1997), Digital isochrons of the world's ocean floor, *Journal of Geophysical Research*, *102*, 3211–3214.

Mysen, B. O., and A. L. Boettcher (1975), Melting of a hydrous mantle: I, Phase relations of natural peridotite at high pressures and temperatures with controlled activities of water, carbon dioxide, and hydrogen, *Journal of Petrology*, *16* (3), 520-548.

Nakajima, J., T. Matsuzawa, A. Hasegawa, and D. Zhao (2001), Three-dimensional structure of Vp, Vs, and Vp/Vs beneath northeastern Japan: Implications for arc magmatism and fluids, *Journal of Geophysical Research*, *106*(B10), 21,843-21,858.

Nakamura, M, H. Watanabe, T. Konomi, S. Kimura, K. Moira (1997), Characteristic activities of subcrustal earthquakes along the outer zone of southwestern Japan, *Annuals of the Disaster Prevention Research Institute*, Kyoto Univ. 40, B-1 (in Japanese).

Nedimovic, M. R., R. D. Hyndman, K. Ramachandran, and G. D. Spence (2003), Reflection signature of seismic and aseismic slip on the northern Cascadia subduction interface, *Nature*, *424*, 416-420.

Newman, A. V., S. Y. Schwartz, V. Gonzalez, H. R. DeShon, and J. M. Protti (2002), Along-strike variability in the seismogenic zone below Nicoya Peninsula, Costa Rica, *Geophysical Research Letters, 29*, doi:10.1029/2002GL015409.

Nichols, G. T., P. J. Wyllie, and C. R. Stern (1994), Subduction zone melting of pelagic sediments constrained by melting experiments, *Nature*, *371*, 785-788.

Nicholson, T., M. Bostock, and J. F. Cassidy (2005), New constraints on subduction zone structure in northern Cascadia, *Geophysical Journal International*, *161*, 849-859.

Obara, K. (2002), Nonvolcanic deep tremor associated with subduction in Southwest Japan, *Science*, *296*, 1679-1681.

Obara, K., H. Hirose, F. Yamamizu, and K. Kasahara (2004), Episodic slow slip events accompanied by non-volcanic tremors in southwest Japan subduction zone, *Geophysical Research Letters*, *31*, doi:10.1029/2004GL020848.

Ogawa, M. (1987), Shear instability in a viscoelastic material as the cause of deep focus earthquakes, *Journal of Geophysical Research*, *92*, 13801-13810.

Ohkura, T. (2000), Structure of the upper part of the Philippine Sea plate estimated by later phases of upper mantle earthquakes in and around Shikoku, Japan, *Tectonophysics*, *321*, 17-36.

Okino, K., Y. Shimakawa, and S. Nagaoka (1994), Evolution of the Shikoku Basin, *Journal of Geomagnetism and Geoelectricity*, *446*, 463-479.

Ohta, Y., J. T. Freymueller, S. Hreinsdóttir, and H. Suito (2006), A large slow slip event and the depth of the seismogenic zone in the south central Alaska subduction zone, *Earth and Planetary Science Letters*, 108-116.

Oleskevich, D. A., R. D. Hyndman, and K. Wang (1999), The updip and downdip limits to great subduction earthquakes: Thermal and structural models of Cascadia, south Alaska, SW Japan, and Chile, *Journal of Geophysical Research*, *104*, 14965-14991.

Ozawa, S., M. Murakami, M. Kaidzu, T. Tada, T. Sagiya, Y. Hatanaka, H. Yarai, and T. Nichimura (2002), Detection and monitoring of ongoing aseismic slip in the Tokai region, central Japan, *Science*, *298*, 1009-1012.

Pacheco, J., L. R. Sykes, and C. H. Scholz (1993), Nature of seismic coupling along simple plate boundaries of the subduction type, *Journal of Geophysical Research*, *98*, 14133-14159.

Pawley, A. R., and J. R. Holloway (1993), Water sources for subduction zone volcanism: New experimental constraints, *Science*, *260*, 664-667.

Pawley, A. R., and B. J. Wood (1995), The high-pressure stability of talc and 10 Å phase: Potential storage sites for H_2O in subduction zones, *American Mineralogist*, *80*, 998-1003.

Payero, J. V. Kostoglodov, N. Shapiro, T. Mikumo, A. Iglesias, X. Pérez-Campos, and R. W. Clayton (2008), Nonvolcanic tremor observed in the Mexican subduction zone, *Geophysical Research Letters*, *35*, L07305, doi:10.1029/2007GL032877.

Peacock, S. M. (1987), Serpentinization and infiltration metasomatism in the Trinity peridotite, Klamath province, northern California: implications for subduction zones, *Contributions to Mineralogy and Petrology*, *95*, 55-70.

Peacock, S. M. (1993), The importance of blueschist → eclogite dehydration reactions in subducting oceanic crust, *Geological Society of America Bulletin*, *105*, 684-694.

Peacock, S.M. (1996), Thermal and petrologic structure of subduction zones, in *Subduction: Top to bottom*, *Geophysical Monograph Series*, *96*, edited by G. E. Bebout et al., pp. 119-133, American Geophysical Union, Washington, D. C.

Peacock, S. M. (2001), Are the lower planes of double seismic zones caused by serpentine dehydration in subducting oceanic mantle?, *Geology*, *29*, 299-302.

Peacock, S. M. and R. D. Hyndman (1999), Hydrous minerals in the mantle wedge and the maximum depth of subduction thrust earthquakes, *Geophysical Research Letters*, *26*, 2517-2520.

Peacock, S. M. and K. Wang (1999), Seismic consequences of warm versus cool subduction metamorphism: Examples from Southwest and Northeast Japan, *Science*, *286*, 937-939.

Peacock, S. M., T. Rushmer, and A. B. Thompson (1994), Partial melting of subducting oceanic crust, *Earth and Planetary Science Letters*, *121*, 227-244.

Peacock, S. M., P. E. van Keken, S. D. Holloway, B. R. Hacker, G. A. Abers, and R. L. Fergason (2005), Thermal structure of the Costa Rica – Nicaragua subduction zone, *Physics of the Earth and Planetary Interiors*, *149*, 187-200.

Peterson, C., D. Christensen, and S. McNutt (2007), Non-volcanic tremor in south-central Alaska and its relation to the 1998-2000 slow-slip event, *EOS Transactions of American Geophysical Union*, *88*(52), Fall Meeting Supplement, Abstract T11F-08.

Plank, T., and C. H. Langmuir (1998), The chemical composition of subducting sediment and its consequences for the crust and mantle, *Chemical Geology*, 145, 325-394.

Pollack, H. N., S. J. Hurter, and J. R. Johnson (1993), Heat flow from the earth's interior: Analysis of the global data set, *Reviews of Geophysics, 31*, 267-280.

Pozgay, S. H., D. A. Wiens, J. A. Conder, H. Shiobara, and H. Sugioka (2007), Complex mantle flow in the Mariana subduction system: evidence from shear wave splitting, *Geophysical Journal International*, *170*, 371–386.

Preston, L. A., K. C. Creager, R. S. Crosson, T. M. Brocher, and A. M. Trehu (2003), Intraslab earthquakes: Dehydration of the Cascadia slab, *Science*, *302*, 1197, doi:10.1126/science.1090751.

Protti, M., F. Guendel, and K. McNally (1995), Correlation between the age of the subducting Cocos plate and the geometry of the Wadati-Benioff zone under Nicaragua and Costa Rica, in *Geologic and Tectonic Development of the Caribbean Plate Boundary in Southern Central America*, Spec. Pap. Geol. Soc. Am. *295*, edited by P. Mann, pp. 309-326.

Ramachandran, K., S. E. Dosso, C. A. Zelt, G. D. Spence, R. D. Hyndman, and T. M. Brocher (2004), Upper crustal structure of southwestern British Columbia from the 1998 Seismic Hazards Investigation in Puget Sound, *Journal of Geophysical Research*, *109*, B09303, doi:10.1029/2003JB002826.

Ramachandran, K., S. E. Doss, G. D. Spence, R. D. Hyndman, and T. M. Brocher (2005), Forearc structure beneath southwestern British Columbia: A three-dimensional tomographic velocity model, *Journal of Geophysical Research*, *110*, B02303, doi:10.1029/2004JB003258.

Ramachandran, K. and R. D. Hyndman (submitted manuscript, 2008)

Ranero, C. R., J. P. Morgan, K. McIntosh, and C. Reichert (2003), Bending-related faulting and mantle serpentinization at the Middle America trench, *Nature*, *425*, 367-373.

Reyners, M., D. Eberhart-Phillips, G. Stuart, and Y. Nishimura (2006), Imaging subduction from the trench to 300 km depth beneath the central North Island, New Zealand, with Vp and Vp/Vs, *Geophysical Journal International*, *165*, 565-583.

Reyners, M., D. Eberhart-Phillips, and G. Stuart (2007), The role of fluids in lower-crustal earthquakes near continental rifts, *Nature*, *446*, doi:10.1038/nature05743.

Riddihough, R. (1984), Recent movements of the Juan de Fuca plate system, *Journal of Geophysical Research*, *89*, 6980-6994.

Rogers, G., and H. Dragert (2003), Episodic tremor and slip on the Cascadia subduction zone: The chatter of silent slip, *Science*, *300*, 1942-1943.

Rondenay, S., G. A. Abers, and P. E. van Keken (2008), Seismic imaging of subduction zone metamorphism, *Geology*, *36*, 275-278.

Saffer, D. M., and C. Marone (2003), Comparison of smectite- and illite-rich gouge frictional properties: application to the updip limit of the seismogenic zone along subduction megathrusts, *Earth and Planetary Science Letters*, *215*, 219-235.

Sagiya, T. (2004), Interplate coupling in the Kanto district, central Japan, and the Boso Peninsula silent earthquake in May 1996, *Pure and Applied Geophysics*, *161*, 2327-2342.

Sallarès, V., and C. R. Ranero (2005), Structure and tectonics of the erosional convergent margin off Antofagasta, north Chile (23°30'S), *Journal of Geophysical Research*, *110*, B06101, doi:10.1029/2004JB003418.

Saltus, R. W., T. L. Hudson, and G. G. Connard (1999), A new magnetic view of Alaska, *GSA today*, *9*, 2-6.

Savage, M. K. (1999), Seismic anisotropy and mantle deformation: What have I learned from shear wave splitting?, *Reviews of Geophysics*, *37*, 65-106.

Schmidt, M. W., and S. Poli (1998), Experimentally based water budgets for dehydrating slabs and consequences for arc magma generation, *Earth and Planetary Science Letters*, *163*, 361-379.

Seno, T. (2005), Variation of downdip limit of the seismogenic zone near Japanese islands: Implications for the serpentinization mechanism of the forearc mantle wedge, *Earth and Planetary Science Letters*, *231*, 249-262.

Seno, T. (2009), Determination of the pore fluid pressure ratio at seismogenic megathrusts in subduction zones: Implications for strength of asperities and Andean-type mountain building, *Journal of Geophysical Research*, *114*, B05405, doi:10.1029/2008JB005889.

Seno, T., and Y. Yamanaka (1996), Double seismic zones, compressional deep trench-outer rise events, and superplumes, in *Subduction: Top to Bottom, Geophysical Monograph Series*, vol. 96, edited by G. E. Bebout et al., pp. 347-355, American Geophysical Union, Washington, D. C.

Seno, T., D. Zhao, Y. Kobayashi, and M. Nakamura (2001), Dehydration of serpentinized mantle: Seismic evidence from Southwest Japan, *Earth Planets and Space*, *53*, 861-871.

Shelly, D. R., G. C. Beroza, S. Ide, and S. Nakamula (2006), Low-frequency earthquakes in Shikoku, Japan, and their relationship to episodic tremor and slip, *Nature*, *442*, 188-191.

Shelly, D. R., G. C. Beroza, and S. Ide (2007), Non-volcanic tremor and low-frequency earthquake swarms, *Nature*, *446,* 305-307.

Shiomi, K., H. Sata, K. Obara, and M. Ohtake (2004), Configuration of subducting Philippine Sea plate beneath southwest Japan revealed from receiver function analysis based on the multivariate autoregressive model, *Journal of Geophysical Research*, *109*, B04308, doi:10.1029/2003JB002774.

Simoes, M., J. P. Avouac, R. Cattin, and P. Henry (2004), The Sumatra subduction zone: A case for a locked fault zone extending into the mantle, *Journal of Geophysical Research*, *109*, B10402, doi:10.1029/2003JB002958.

Smith, G. P., D. A. Wiens, K. M. Fischer, L. M. Dorman, S. C. Webb, and J. A. Hildebrand (2001), A complex pattern of mantle flow in the Lau back arc, *Science*, *292*, 713-716.

Spinelli, G. A., and K. Wang (2008), Effects of fluid circulation in subducting crust on Nankai margin seismogenic zone temperatures, *Geology*, *36*, 887-890.

Stachnik, J. C., G. A. Abers, and D. Christensen (2004), Seismic attenuation and mantle wedge temperatures in the Alaska subduction zone, *Journal of Geophysical Research*, *109*, doi:10.1029/2004JB003018.

Staudigel, H., T. Plank, B. White, and H. -U. Schmincke (1996), Geochemical fluxes during seafloor alteration of the basaltic cupper oceanic crust: DSDP sites 417 and 418, in *Subduction: Top to Bottom*, *Geophysical Monograph Series*, vol. 96, edited by G. E. Bebout, D. W. Scholl, S. H. Kirby, and J. P. Platt, pp. 19-38, American Geophysical Union, Washington, D. C.

Stein, C.A., and S. Stein (1992), A model for the global variation in oceanic depth and heat flow with lithospheric age, *Nature*, *359*, 123-129.

Syracuse, E. M., and G. A. Abers (2006), Global compilation of variations in slab depth beneath arc volcanoes and implications, *Geochemistry, Geophysics, Geosystems*, *7*, doi:10.1029/2005GC001045.

Taira, A., and 10 others (1998), Nature and growth rate of the northern Izu-Bonin (Ogasawara) arc crust and their implications for continental crust formation, *Island Arc*, *7*, 395-407.

Takahashi, E., and I. Kushiro (1983), Melting of a dry peridotite at high pressures and basalt magma genesis, *American Mineralogist*, *68*, 859-879.

Takahashi, N., S. Kodaira, S. L. Klemperer, Y. Tatsumi, Y. Kaneda, and K. Suyehiro (2007), Crustal structure and evolution of the Mariana intra-oceanic island arc, *Geology*, *35*, 203-206.

Tamura, Y., Y. Tatsumi, D. Zhao, Y. Kido, and H. Shukuno (2002), Hot fingers in the mantle wedge: new insights into magma genesis in subduction zones, *Earth and Planetary Science Letters*, *197*, 105-116.

Tanaka, A., M. Yamano, Y. Yano, and M. Sasada (2004), Geothermal gradient and heat flow data in and around Japan, *Digital Geoscience Map DGMP-5*, Geological Survey of Japan.

Tatsumi, Y. (1986), Formation of the volcanic front in subduction zones, *Geophysical Research Letters*, *17*, 717-720.

Tatsumi, Y., and S. Eggins (1995), *Subduction Zone Magmatism*, Blackwell Science, Boston, 211 pp.

Tebbens, S. F., W. C. Cande, L. Kovacs, J. D. Parra, J. L. LaBrecque, and H. Vergara (1997), The Chile ridge: A tectonic framework, *Journal of Geophysical Research*, *102*, 12035-12059.

Tichelaar, B. W., and L. J. Ruff (1993), Depth of seismic coupling along subduction zones, *Journal of Geophysical Research*, *98*, 2018-2037.

Tono, Y. (2006), Use of Hi-net tiltmeter records to image mantle discontinuities and anisotropic structure beneath the Japanese islands, Ph.D. thesis, 101 pp., Univ. of Tokyo, Japan, March.

Townend, J., (1997), Estimates of conductive heat flow through bottom-simulating reflectors on the Hikurangi and southwest Fiordland continental margins, New Zealand, *Marine Geology*, *141*, 209-220.

Tsenn, M. C. and N. L. Carter (1987), Upper limits of power law creep of rocks, *Tectonophysics, 136*, 1-26.

Turcotte, D. L. and G. Schubert (2002), *Geodynamics*, second edition, Cambridge Univ. Press, Cambridge, UK, 456 pp.

Ulmer, P. and V. Trommsdorff (1995), Serpentine stability to mantle depths and subduction-related magmatism, *Science*, *268*, 858-861.

Ulmer, P. (2001), Partial melting in the mantle wedge - the role of H_2O in the genesis of mantle-derived "arc-related" magmas, *Physics of the Earth and Planetary Interiors*, *127*, 215-232.

van Keken, P. E., B. Kiefer, and S. M. Peacock (2002), High-resolution models of subduction zones: Implications for mineral dehydration reactions and the transport of water into the deep mantle, *Geochemistry, Geophysics, Geosystems*, *3*, doi: 10.1029/2001GC000256.

van Keken, P. E., and 10 others (2008), A community benchmark for subduction zone modeling, *Physics of the Earth and Planetary Interiors*, *171*, doi:10.1016/j.pepi.2008.04.015.

Verma, S. P. (2002), Absence of Cocos plate subduction- related basic volcanism in southern Mexico: A unique case on Earth?, *Geology*, *30*, 1095-1098.

von Herzen, R., C. Ruppel, P. Molnar, M. Nettles, S. Nagihara, and G. Ekstrom (2001), A constraint on the shear stress at the Pacific-Australian plate boundary from heat flow and seismicity at the Kermadec forearc, *Journal of Geophysical Research*, *106*, 6817-6833.

Vrolijk, P. (1990), On the mechanical role of smectite in subduction zones, *Geology*, *18*, 703-707.

Wada, I., K. Wang, J. He, and R. D. Hyndman (2008), Weakening of the subduction interface and its effects on surface heat flow, slab dehydration, and mantle wedge serpentinization, *Journal of Geophysical Research*, *113*, B04402, doi:10.1029/2007JB005190.

Wada, I., and K. Wang (2009), Common depth of decoupling between the subducting slab and mantle wedge: Reconciling diversity and uniformity of subduction zones, *Geochemistry, Geophysics, Geosystems*, doi:10.1029/2009GC002570, in press.

Wada, I., S. Mazzotti, and K. Wang (2009), Intraslab stresses in the Cascadia subduction zone from inversion of earthquake focal mechanisms, submitted to *Journal of Geophysical Research.*

Wallace, L.M., J. Beavan, R. McCaffrey, and D. Darby (2004), Subduction zone coupling and tectonic block rotations in the North Island, New Zealand, *Journal of Geophysical Research*, *109*, doi:10.1029/2004JB003241.

Wang, K., and E. E. Davis (1992), Thermal effect of marine sedimentation in hydrothermally active areas, *Geophysical Journal International*, *100*, 70-78.

Wang, K., and J. He (1999), Mechanics of low-stress forearcs: Nankai and Cascadia, *Journal of Geophysical Research*, *104*, 15191-15205.

Wang, K., and K. Suyehiro (1999), How does plate coupling affect crustal stresses in Northeast and Southwest Japan?, *Geophysical Research Letters*, *26*, 2307-2310.

Wang, K., T. Mulder, G. C. Rogers, and R. D. Hyndman (1995), Case for very low coupling stress on the Cascadia subduction fault, *Journal of Geophysical Research*, *100*, 12907-12918.

Wang, K., R. Wells, S. Mazzotti, R. D. Hyndman, and T. Sagiya (2003), A revised dislocation model of interseismic deformation of the Cascadia subduction zone, *Journal of Geophysical Research*, *108*, 2026, doi:10.1029/2001JB001227.

Wang, K., Wada, I., and Ishikawa, Y. (2004), Stresses in the subducting slab beneath southwest Japan and relation with plate geometry, tectonic forces, slab dehydration, and damaging earthquakes, *Journal of Geophysical Research*, *109*, B08304, doi:10.1029/ 2003JB002888.

Wang, K., H. Dragert, H. Kao, and E. Roeloffs (2008), Characterizing an ‘‘uncharacteristic’’ ETS event in northern Cascadia, *Geophysical Research Letters*, *35*, L15303, doi:10.1029/2008GL034415.

Wech, A. G., and K. C. Creager (2007), Cascadia tremor polarization evidence for plate interface slip, *Geophysical Research Letters*, *34*, L22306, doi:10.1029/2007GL031167.

Westbrock, G. K., et al. (1994), Proceedings of the Ocean Drilling Program, Initial Reports, vol. 146, part 1, Ocean Drilling Program, College Station, Tex..

White, S. M., J. A. Crisp, and F. J. Spera (2006), Long-term volumetric eruption rates and magma budgets, *Geochemistry, Geophysics, Geosystems*, *7*, Q03010, doi:10.1029/2005GC001002.

Wiens D. A., and G. P. Smith (2003), Seismological constraints on structure and flow patterns within the mantle wedge, in *Inside the Subduction Factory*, *Geophysical Monograph Series*, vol. 138, edited by J. Eiler, pp. 59-81, American Geophysical Union, Washington, D. C.

Wilson, D. S. (1988), Tectonic History of the Juan de Fuca Ridge over the last 40 million years, *Journal of Geophysical Research*, *93*, 11863-11876.

Wilson, D. S. (1993), Confidence intervals for motion and deformation of the Juan de Fuca plate, *Journal of Geophysical Research*, *88*, 16053-16071.

Xia, S., D. Zhao, and X. Qiu (2008), Tomographic evidence for the subducting oceanic crust and forearc mantle serpentinization under Kyushu, Japan, *Tectonophysics*, *449*, 85-96.

Yamano, M. (1995), Recent heat flow studies in and around Japan, in *Terrestrial heat flow and geothermal energy in Asia*, edited by M. L. Gupta and M. Yamano, pp. 173-201, Oxford and IBH Publishing Co. Pvt. Ltd., Bombay.

Yamasaki, T., and T. Seno (2003), Double seismic zones and dehydration embrittlement of the subducting slab, *Journal of Geophysical Research*, *108* (B4), 2212 doi:10.1029/2002JB 001918.

Yuan, X., and 21 others (2000), Subduction and collision processes in the central Andes constrained by converted seismic phases, *Nature*, *408*, 958-961.

Zang, S. X., Q. Y. Chen, J. Y. Ning, Z. K. Shen, and Y. G. Liu (2002), Motion of the Philippine Sea plate consistent with the NUVEL-1A model, *Geophysical Journal International*, *150*, 809-819.

Zhao, D., A. Hasegawa, and H. Kanamori (1994), Deep structure of Japan subduction zones as derived from local, regional and teleseismic events, *Journal of Geophysical Research*, *99*, 22313-22329.

Zhao, D., T. Matsuzawa, and A. Hasegawa (1997), Morphology of the subducting slab boundary in the northeastern Japan arc, *Physics of the Earth and Planetary Interiors*, *102*, 89-104.

Zhao, D., K. Asamori, and H. Iwamori (2000), Seismic structure and magmatism of the young Kyushu subduction zone, *Geophysical Research Letters*, *27*, 2057-2060.